# Measurement and Evaluation of In-Core Gamma Heating in the McMaster Nuclear Reactor

# Measurement and Evaluation of In-Core Gamma Heating in the McMaster Nuclear Reactor

By Mohammed Alqahtani,

*A Thesis Submitted to the School of Graduate Studies in the Partial Fulfillment of the Requirements for the Degree Ph.D.*

McMaster University © Copyright by Mohammed Alqahtani

April 28, 2021

DOCTOR OF PHILOSOPHY (2021) McMaster University

(Department of Engineering Physics) Hamilton, Ontario, Canada

TITLE: Measurement and Evaluation of In-Core Gamma Heating in the McMaster Nuclear Reactor.

AUTHOR: Mohammed Alqahtani

Ph.D. Candidate (Engineering Physics, McMaster University)

M.Sc. (Nuclear Engineering, Balseiro Institute)

B.Sc. (Production Engineering and Mechanical Systems Design, King Abdulaziz University)

SUPERVISOR: Professor Dr. Adriaan Buijs

NUMBER OF PAGES: xix, 116

# Abstract

The emission of gamma radiation in nuclear reactors manifests itself as heat which may substantially impact irradiation applications and reactor safety. Evaluating this phenomenon can increase the efficiency and safety of the reactor and its irradiation materials. Calculating or predicting the gamma heating (GH) in a nuclear reactor is not a simple task, especially when not all parameters of the reactor are known. This dissertation incorporates various methods for verifying results, including operational data, calculations and measurements. The thesis is divided into five research chapters to illuminate uncharted areas for simulation codes and to better understand factors influencing the GH. Study 1 applies the overall system for calculation of reactors (OSCAR-4) code system to the McMaster Nuclear Reactor (MNR) for understanding and verifying core-follow calculations against the MNR operational data. Based on this understanding, the calculational scheme presented advances to the operational fuel management data by (i) embodying an axial U-235 distribution profile and (ii) including all fissile materials present in the core. Study 2 gives insight into the impact of control rods (CR) movement on axial fuel inventory using the OSCAR-4 and Serpent-2 simulation codes. This was done to study whether OSCAR-4 performs as well as the time-consuming Serpent-2 for core-follow calculations. It was found that averaging the CRs movement can precisely predict fuel inventory without requiring detailed CRs tracking. Study 3

focused on improving MNR fuel operational data which were subsequently used in both the OSCAR-4 and Serpent-2 simulation codes. This research emphasizes the importance of applying the fuel inventory correction factor to any MNR cycle to accurately predict the fuel inventory at any given stage of a cycle. Study 4 involved the experimental measurement of GH using the SCK-CEN gamma thermometer (GT) in three irradiation sites at 27 GH values. In addition, a Serpent-2 simulation was conducted to calculate the GH at the same 27 points with an understanding of uncertainties accompanied by the measurement. Similarly, MCNP-6 code was implemented with the same methodology used for both OSCAR-4 and Serpent-2 and showed a very good agreement with the reactor operation data and GH measurement. The computational tools program provided a good prediction and evaluation of the GH. Finally, study 5 expanded the evaluation and uncertainty quantification of the GH under several reactor core conditions and time-dependent sets. The measurements presented in this work indicate that, even over four years, the combined effects of fuel burnup and fuel management operations do not significantly change the GH level inside the beryllium site. This is likely due to the overall distribution of the MNR core configuration and fuel burnup.

# *Acknowledgements*

This thesis would not have been completed without the support I received before and during the beginning my Ph.D. journey. First, I would like to thank my supervisor Dr. Adriaan Buijs for offering me this opportunity to pursue my higher education in the nuclear field. He was always available for any concerns I had. Dr. Buijs's help was not only in the research field; he encouraged me to mingle with experts in the nuclear field and participate in many conferences, which was crucial to develop my research. I would also like to thank Dr. Simon Day for his support, especially during the beginning of this research, and for always being available to answer technical questions about the McMaster Nuclear Reactor. Special thanks to Dr. David Novog for his valuable comments and ideas on my research during the annual meetings and beyond.

In this work, I was fortunate enough to have the McMaster Nuclear Reactor group available to support my research. Thanks to Chris Heysel, reactor director, for letting me access the reactor whenever I needed. Also, thanks to Jay Grigg-Tait, Rob Pasuta, Frank Labonte, and the MNR operators for accommodating the experimental campaign. Jay Grigg-Tait was always available to answer any questions I had about the reactor part during the measurement. Also, thanks to Elizabeth MacConnachie for the beneficial discussions we had during part of this work. Also, sincere gratitude goes to Dr. Rouben Benjamin, who was always available to answer my inquiries on reactor fuel burnup and temporal neutron

behavior.

I would also like to thank the King Abdulaziz City for Science and Technology (KACST) for the support and funding during my Ph.D. journey. Two people greatly impacted my career and life at KACST: Dr. Turki bin Saud and Dr. Khalid Aleissa. Their guidance and enlightenment shaped my life and helped me become who I am now. I also appreciate the moral support from Dr. Sultan Alsagabi. Thanks should also go to my close colleagues in Argentina, Fahad, Yousef, Feras and Abdullah. I also have to mention my colleagues in the Department of Engineering Physics at McMaster University. Also, thanks to the South African Nuclear Energy Corporation Limited (Necsa), especially Dr. Rian Prinsloo and Dr. Francois van Heerden, for their support of the OSCAR-4 code. I would also like to thank Dr. Erwin Alhassan from my research group at the first year of this work for many enjoyable lunches and useful discussions. Not to forget, I am so thankful for Lorena Pilar.

I'm extremely grateful for the blessing of my son Tamim who has filled my life with love, joy, and happiness. Finally, my deepest gratitude to my family for their continuous and relentless love, help, and support. I am forever indebted to my parents for teaching me the importance of education in life, which has made me who I am.

*To my son Tamim, my parents, my sisters and my brothers.*

# Contents

# List of Figures

# List of Tables

# Declaration of Authorship

The thesis consists of four articles in refereed journals. The author (Mohammed Alqahtani) was the main contributor to each article. Prior to publication, the ideas of the articles were discussed and developed with the supervisor Dr. Buijs and the supervisory committee, which included Dr. Novog and Dr. Day. However, background investigation, simulation preparation, simulation execution, and analysis were performed either solely or primarily by the author.

# Chapter 1

# Introduction

## 1.1 Background

Research reactors are major contributors to improving human health and quality of life, manufacturing better industrial products, and advancing science and technology. In order to ensure their safe operation, a complete understanding of reactor parameters and conditions is deemed important in safety assessments for a sustainable continuous supply of isotope production and material irradiation [1]. Many countries have built research reactors and operated them for many years. Figures 1.1 and 1.2 show the timeline and regional distribution of research reactors worldwide.

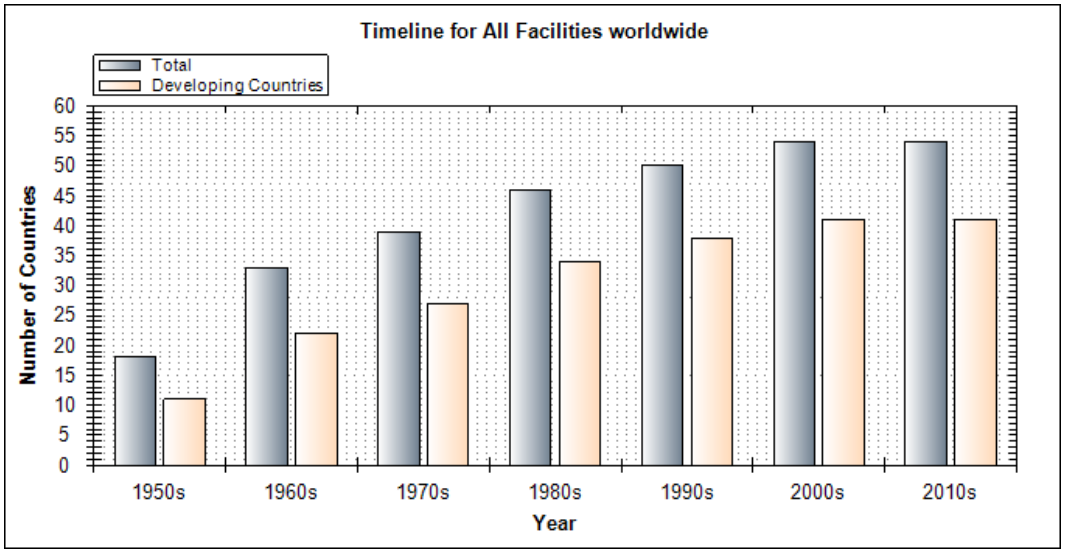


FIGURE 1.1: Timeline of Research Reactors for category: Isotope Production Facilities, IAEA.

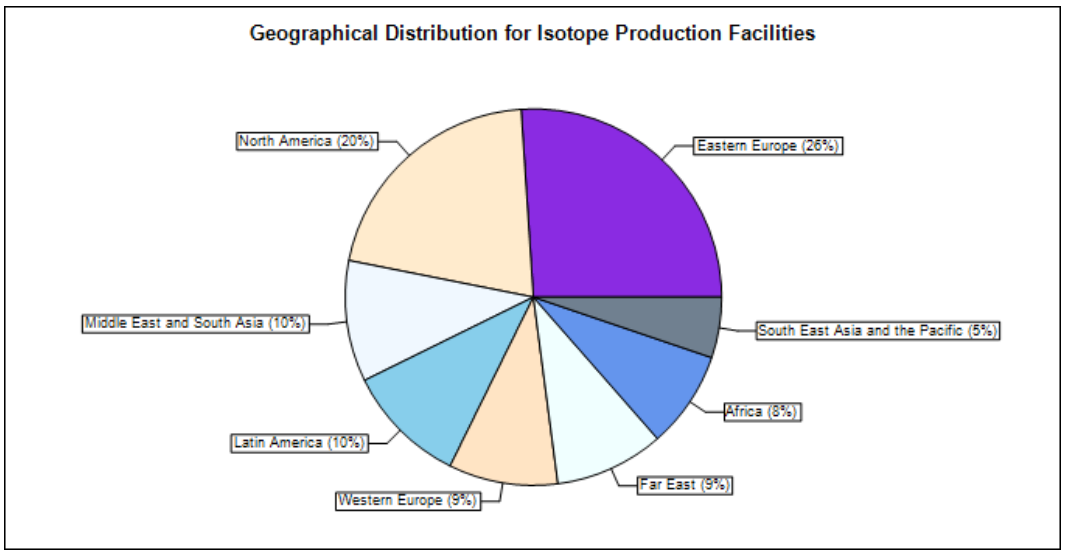


FIGURE 1.2: Regional distribution of Research Reactors for category: Isotope Production Facilities, IAEA.

Nuclear research reactors produce neutrons and photons that can be widely used for multipurpose applications involving education,

training, and production of radioisotopes for medicine and industry. They also serve in applied research and for testing various types of nuclear fuel and studying the radiation resistance of new materials. Therefore, providing information on several peaceful applications has always been recommended by the International Atomic Energy Agency (IAEA).

One of such recommendations is irradiation applications, in which target materials and irradiation conditions can be optimized for higher quality of the irradiation purposes, such as isotope production, activation analysis, experiments, measurement analysis and others [2]. Nonetheless, several factors may influence the quality and environmental condition of any irradiation test in any nuclear reactor. These include reactor fuel composition, power density, core configuration and other such parameters. All these parameters strongly exhibit the gamma heating dependent behavior at any nuclear reactor core. Excessive gamma radiation can cause overheating and is therefore a safety parameter. Having an on-line information of essential physical parameters for the follow-up and analysis before any experiment is carried out is necessary.

Previous research in this field concerning nuclear research reactors have largely focused on neutron flux [3] [4] [5], which is an important parameter in any nuclear reactor for multiple reasons, such as obtaining required activity for isotope production, specimen irradiation etc. However, literature reviews show a lack of comprehensive information on gamma heating that is evaluated by both simulations and measurements under several core conditions. In addition, there is no previous research combining the studying of the gamma heating

(GH) with the actual reactor core condition for low and medium research reactor, and more specifically for the MNR core, one of which is fuel core inventory in different time frames.

Efforts are therefore put in place to quantify all uncertainties that can influence this condition either computationally or experimentally. In the last few years there has been a growing interest in studying the nuclear/gamma heating, which is the main cause for temperature rise in non-fuelled regions of a nuclear reactor [6]. If gamma heat and its associated uncertainties are not taken into consideration in reactor analysis, reactor safety could be compromised.

## 1.2 Motivation

Nuclear research reactors will continue playing a vital role worldwide in the coming decades [7]. In Canada, the major nuclear research, education, and commercial reactor is located at McMaster University, the McMaster Nuclear Reactor (MNR). MNR is the major international supplier of the medical isotope iodine-125, used for cancer brachytherapy, and is the only approved North American supplier of holmium-166 microspheres for radioembolic therapy among other commercial applications such as aircraft safety and resources discovery support.

Thus, in order to support the sustainability of the MNR and, at the same time, pursue its applications for providing services to maximize the quality of life, utilizing computational tools to develop, validate and optimize is crucial. Reliable core analysis for isotope inventory is necessitated for any computational tools application in order to, eventually, help evaluating not only the gamma heating but

also the other reactor core safety parameters. Computational tools calculation will be benchmarked against measurements and operational data.

Up until the date of this research, MNR fuel inventory estimates were mainly used to support fuel management using a semi-empirical measurement based system. This method is time-consuming and conservative approach to estimating U235 depletion with relatively high uncertainty for use in detailed physics calculations. The time evolution of material composition is a vital parameter in any simulation code application. Therefore, prior to implementing a computational code against operational data or measurement, fuel composition has to be analyzed. Once this uncharted area is illuminated, measurement and operational parameters can be utilized in parallel with the computational tools.

In addition, research reactors are small reactors with high power density. As a result, the core experiences a high gamma flux that leads to heat generation and hence changes in the irradiation conditions. A few incidents due to radiation damage have been noticed during sample irradiation, one of these has been reported in MNR [8]. For such incidents, it was of interest to investigate and evaluate the gamma heating for any future irradiation.

# Chapter 2

# Reactor Physics Theory and Background

In general, two types of reactor core calculation are used to solve neutron and photon transport. Those are: (i) the stochastic method, where a detail information of particles is provided by simulating individual particles and recording some aspects of their average behavior, and (ii) the deterministic method, where approximation is made on the transport equation to solve the reactor physics parameters in a shorter time and usually it gives fairly comparable to the most detail method (stochastic). This chapter introduces the fundamental concepts of reactor physics theory that are used throughout this thesis.

## 2.1 Neutron Interactions

The neutron is an electrically neutral particle. It can pass easily through the atomic electron cloud and may interact with nuclei of the atoms. Neutrons interact with material in either a scattering or an absorption interaction.

### 2.1.1 Neutron Scattering

In this type of interaction, the neutron can undergo elastic scattering or inelastic scattering. The former interaction can occur by way of the potential scattering interaction mechanism. The cross-section for this scattering can be approximated by

$$\sigma_e = 4\pi R^2, \tag{2.1}$$

Where $R$ is the nuclear radius. In this type of scattering, the neutron collides with the nucleus without being absorbed. As a consequence, the neutron loses energy and alters its direction based upon the target nuclei mass ($A$). The neutron energy in elastic scattering ranges between a maximum energy nearly equivalent to the incident energy of $E_o$ and a minimum energy of $\alpha E_o$

$$\alpha E_o < E < E_o,$$

where $\alpha$ can be defined as

$$\alpha = \frac{(A-1)^2}{(A+1)^2}.$$

The other type of scattering is inelastic scattering in which the neutron is absorbed by the nucleus and then re-emitted with different energy. It differs from elastic scattering in that it keeps the nucleus in an excited state. Hence, the nucleus later de-excites by emitting one or more $\gamma$-rays.

### 2.1.2 Neutron Absorption

The next type of neutron interaction is neutron absorption in which a neutron is absorbed and a compound nucleus is formed. Subsequently, the compound nucleus undergoes de-excitation by either:

- **Radiative capture** where the target nucleus absorbs the neutron and then emits one or several $\gamma$-rays to reach a stable ground state. The neutron will transform the mass number M to M+1. This interaction represents a neutron loss for the system.
- **Fission reaction** where the nucleus of an atom is split into two or more nuclei. As a result, lower mass atoms are produced and fission neutrons are released.

The fission reaction is the principal source of nuclear energy. It releases energy with the target nucleus of approximately 200 MeV, this varies with target nucleus. The majority of the released energy is formed as kinetic energy of the fission products. Table 2.1 shows the kinetic energies of the particles resulting from U-235 fission. The sum of these kinetic energies is equal to the total energy released by fission. Most of this energy can be recovered, except for the energy of the neutrinos, which escape the reactor without interacting.

TABLE 2.1: Emitted energies from U-235 fission.

| Form | Emitted Energy (MeV) |
|---|---|
| Fission fragments | 168 |
| Fission product decay | |
| $\beta$ rays | 8 |
| gamma rays | 7 |
| neutrinos | 12 |
| Prompt gamma rays | 7 |
| Fission neutrons | 5 |
| TOTAL | 207 |

Fission products, along with neutrons are emitted after a fissile nucleus undergoes nuclear fission. The fission fragment yield depends

upon the fissile isotope e.g. U-235 and Pu-239. These two isotopes can produce different fission products, see Figure 2.1 [9].

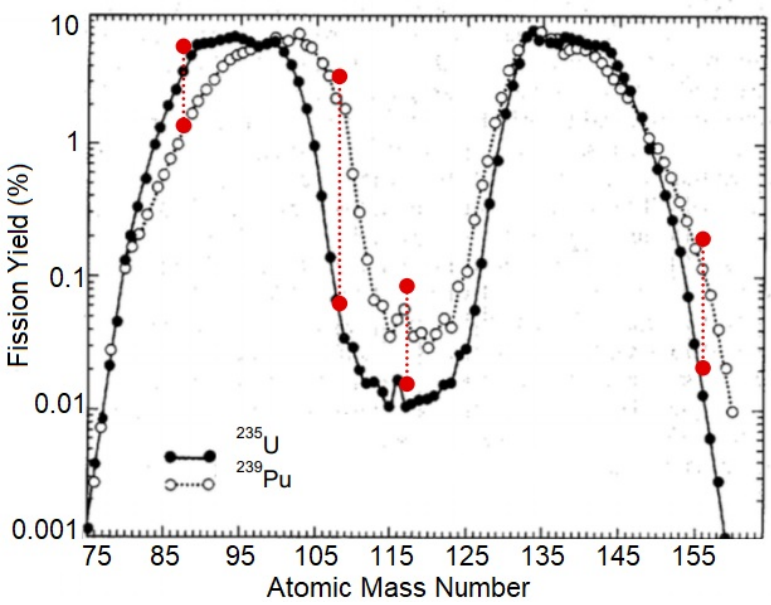


FIGURE 2.1: Cumulative thermal fission product-yield distributions for U-235 and Pu-239 [10].

The fission fragments produced are generally unstable. They will eventually seek stability through series of transformations such as emitting $\gamma$-ray or $\beta$-decay or by ejecting a neutron. The latter are produced after the initial fission, they are called delayed neutrons and play a major role in reactor kinetics and control.

## 2.2 Neutron production

The neutron emissions inside a nuclear reactor can be categorized into: prompt and delayed neutrons. The prompt neutrons emit immediately following fission processes in a matter of $10^{-13}$ seconds. The prompt neutrons energy spectrum can be well described by the

function

$$\chi(E) = 0.453 \times e^{-1.036 \times E} \sinh \sqrt{2.29 \times E}, \tag{2.2}$$

where $\chi(E)$ is the fraction of the prompt neutrons with energy $E$ in MeV. Figure 2.2 shows the prompt neutron energy spectrum.

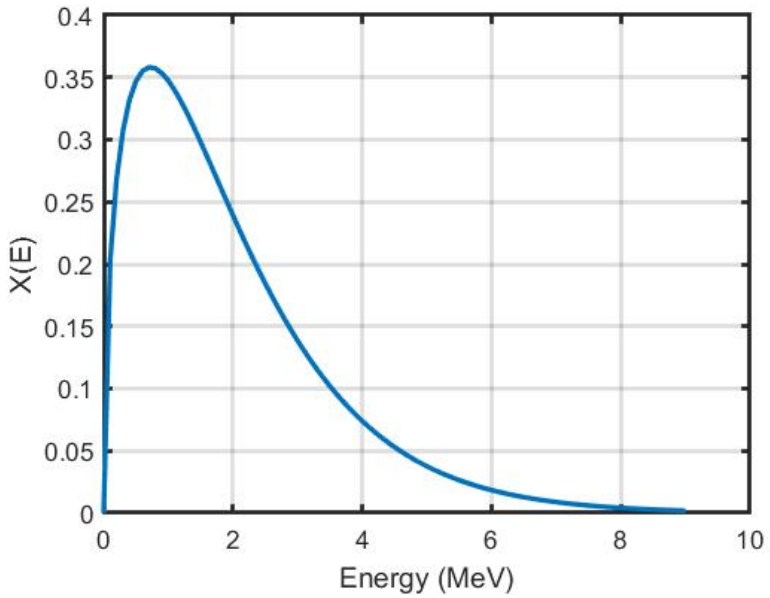


FIGURE 2.2: Prompt neutron energy spectrum

The unstable fission products can also emit neutrons (delayed neutrons). The fission fragments can undergo one or more - decays before emitting a neutron. Due to the different half-lives of the delayed neutrons emissions, it was found adequate to group them in six groups (see Table 2.2).

TABLE 2.2: Delayed neutrons for thermal fission in U-235.

| Group | Half-life (sec) | Decay constant ($sec^{-1}$) | Fraction ($\beta_i$) |
|---|---|---|---|
| 1 | 55.72 | 0.0124 | 0.000215 |
| 2 | 22.72 | 0.0305 | 0.001424 |
| 3 | 6.22 | 0.111 | 0.001274 |
| 4 | 2.3 | 0.301 | 0.002568 |
| 5 | 0.61 | 1.14 | 0.000748 |
| 6 | 0.23 | 3.01 | 0.000273 |

## 2.3 Neutron transport

The propagation of neutron in a nuclear reactor core is a stochastic process, through which interaction with medium is a probabilistic manner. The neutron in a multi-dimensional phase-space system can be described from Boltzmann transport equation (BTE), which is originally the fundamental tool for describing the dynamics of dilute gases. The BTE describes the statistical behaviour of radiations motion through media. For instance, a particle in a nuclear rector can be located at any position $\bar{r}$, with an energy E, and a direction of motion defined by the unit vector $\hat{\Omega}$. Figure 2.3 demonstrates the differential volume of phase-space $d^3r\ d\hat{\Omega}\ dE$ at any given position with vector $\bar{r}$ in a small volume $d^3r$, traveling in some direction $\Omega$, with some infinitesimally small energy group dE at time t.

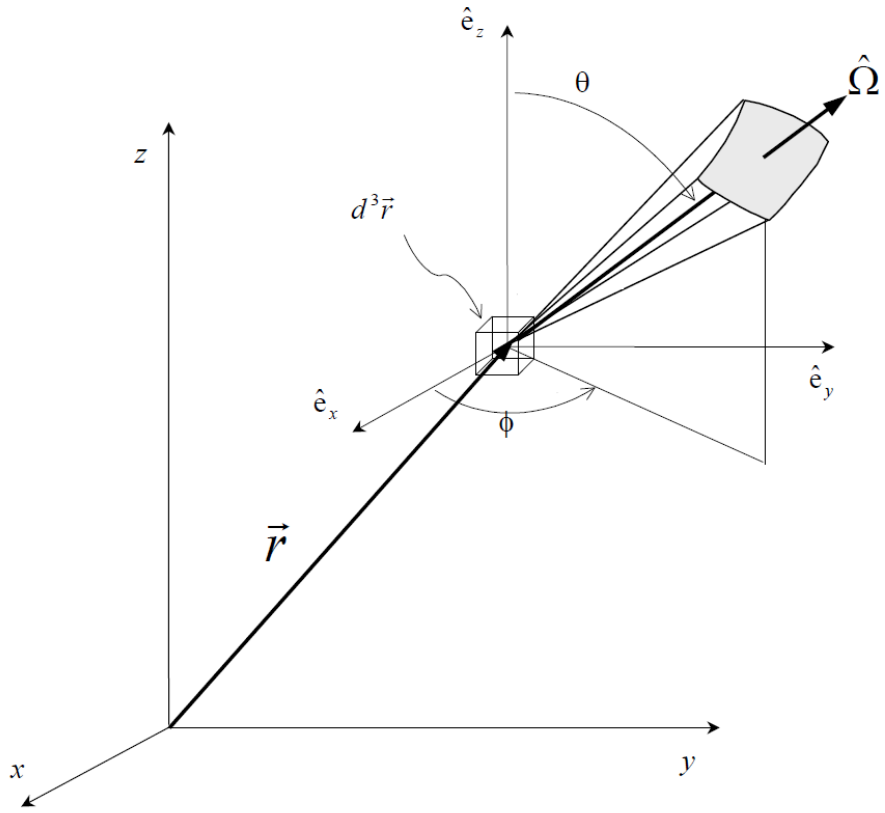


FIGURE 2.3: Multi-dimensional phase-space system of a particle at position $\bar{r}$, direction $\hat{\Omega}$ and energy E, per unit volume, solid angle and energy [11].

In an arbitrary volume with neutrons in a nuclear reactor, a neutron can either appear or disappear following collision. These mechanisms can be classified into various phenomena such as: neutron source, neutron streaming, neutron scattering, neutron leakage and neutron absorption. Therefore, in order to define how neutrons interact, it is imperative to describe the population of those neutrons within an element of a multi-dimensional phase-space. Those population can be described as the number of neutrons within the spatial element $d^3r$ about $\bar{r}$ moving within the solid angle element $d\hat{\Omega}$ about

$\hat{\Omega}$, with energy in the range dE about E, and can be written as

$$n(\bar{r}, E, \hat{\Omega}, t)\ d^3r\ d\hat{\Omega}\ dE\ dt \tag{2.3}$$

This term is the most general angular neutron density function. It is the fundamental term required to define the exact equation. However, this quantity by itself can not describe the interaction frequency, therefore the macroscopic cross section and neutron speed are introduced with the neutron density to determine the reaction rate as follow

$$R(\bar{r}, E, \hat{\Omega}, t) = v\Sigma n(\bar{r}, E, \hat{\Omega}, t) \tag{2.4}$$

The quantity of $vn(\bar{r}, E, \hat{\Omega}, t)$ is the angular neutron flux $[\frac{n}{cm^2.s}]$. From this reaction rate, one can describe all the reaction types that may cause either gains or losses in any defined system. For instance, for many one-group, two-group and three-group energies, fission is always a source term in transport equation as their energy is started with a minimum of 1 MeV. The absorption reaction rate is neutron loss. The differential scattering can be either considered as a gain or loss, as a high energy neutron may collide with the medium and lose/gain energy to E, this term can be described as $\Sigma_s(\vec{r}, E' \rightarrow E, \vec{\Omega}' \rightarrow \vec{\Omega}, t)$ or $\Sigma_s(\vec{r}, E \rightarrow E', \vec{\Omega} \rightarrow \vec{\Omega}', t)$. Neutron sources can also gain our system with neutrons as well as neutron streaming into our system. Finally, the neutron leakage into or from the system can be described with the term of neutron current as follow

$$j(\bar{r}, E, \hat{\Omega}, t).dS = v\hat{\Omega}n(\bar{r}, E, \hat{\Omega}, t).dS \tag{2.5}$$

where this terms describes the angular neutron current density rate at which neutrons with energy dE about E and direction $d\hat{\Omega}$ about $\hat{\Omega}$ passing through a surface element dS at location r.

The neutron transport equation describes all the phenomena that may lead to an appearance/disappearance of the neutron. There are other minor reactions that can cause neutron production and will not be considered in the equations such as photo-fission and (n,in) reactions. Considering all the terms introduced in this section, the NTE can now be written as follows:

$$\frac{1}{\upsilon}\frac{\partial\varphi(\vec{r},E,\vec{\Omega},t)}{\partial t} = s(\bar{r},E,\hat{\Omega},t)+\int_{4\pi}\mathrm{d}\vec{\Omega}'\int_0^\infty \mathrm{d}E'\Sigma_s(\vec{r},E'\to E,\vec{\Omega}'\to\vec{\Omega},t)$$
$$\varphi(\vec{r},E',\vec{\Omega}',t)+\frac{\chi(E)}{4\pi}\int_{4\pi}\mathrm{d}\vec{\Omega}'\int_0^\infty \mathrm{d}E'\nu(E)\Sigma_f(E')\varphi(\vec{r},E',\vec{\Omega}',t)$$
$$-\vec{\Omega}\cdot\nabla\varphi(\vec{r},E,\vec{\Omega},t)-\Sigma_t(\vec{r},E)\varphi(\vec{r},E,\vec{\Omega},t) \quad (2.6)$$

where:

$s(\bar{r},E,\hat{\Omega},t)$ is all the neutron sources in the system,

$\varphi(\vec{r},E,\vec{\Omega},t)$ is the angular neutron flux in $(\vec{r},E,\vec{\Omega},t)$.

$\nu(E)$ is the number of neutrons appeared in region $\vec{r}$ at energy $E$ following a fission reaction at the same location,

$\chi(E)$ is the fission spectrum, in other words, the probability for a neutron to appear with energy $E$ in region $\vec{r}$,

$\Sigma_f(E')$ is the macroscopic neutron fission cross section

$\Sigma_t(\vec{r},E)$ is the total macroscopic neutron cross section that cause the system to lose neutron by either scattering or absorption interaction,

$\Sigma_s(\vec{r},E'\to E,\vec{\Omega}'\to\vec{\Omega},E')$ is the macroscopic scattering neutron

cross section from all other $\mathrm{d}E'$, $\mathrm{d}\vec{\Omega}'$ to the system of $\mathrm{d}E$, $\mathrm{d}\vec{\Omega}$, and $\vec{\Omega} \cdot \nabla\varphi(\vec{r}, E, \vec{\Omega}, t)$ describes the neutrons leakage out from the system.

## 2.4 Reactor Physics Theory

The NTE describes the transport of neutron particles from one collision with an atom to another. It is a 'balance' statement that accounts for all additions and subtractions in a given increment of space, energy, direction and time. The NTE cannot be solved analytically unless simplifying assumptions are made. Numerical techniques are often implemented to obtain physically realistic solutions to the NTE. These techniques can be classified into: (i) stochastic methods, and (ii) deterministic methods [12]. This section will provide the reactor physics theory that is used throughout the journal articles included in this thesis.

### 2.4.1 Stochastic method

In stochastic nuclear physics codes, such as MCNP and Serpent, individual particles are simulated, tracked, and then some aspects of their average behavior are scored. The Monte Carlo method creates a series of particle histories by using random sampling techniques. It can be used in the combined neutron/photon transport, and hence based on the type of the neutron interaction, one or more photons can be produced. Subsequently, photon tracking is performed. Photon

interaction will be discussed later in this chapter. The results obtained by MC methods are estimated results which should lie within some confidence interval about the 'true' value [13].

The MC method uses statistical processes to simulate the interaction of nuclear particles with materials. This statistical sampling processes is calculated based on random numbers. It comprises of particles tracking from its source throughout its life to its disappearance i.e. leaking and absorption. Figure 2.4 describes the process of random walk of neutron incident on a fissile material.

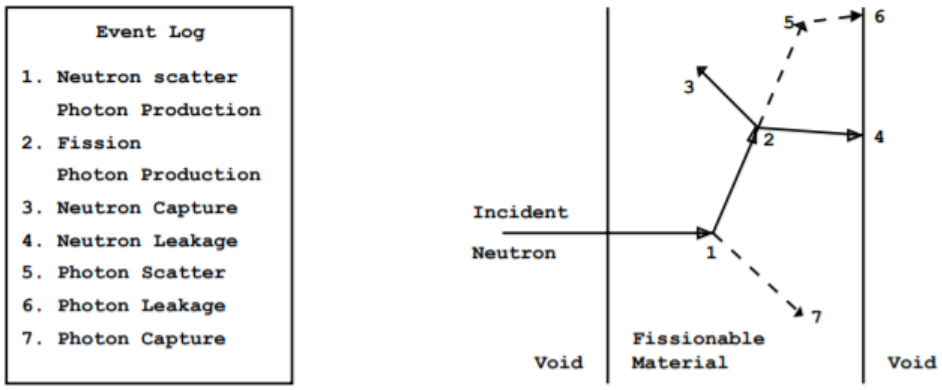


FIGURE 2.4: Neutron random walk in a fissile or fissionable material [14].

The simulation approach in MC in Figure 2.6 is as follows: the neutron interacts at point 1, where a scattering interaction occurred and photon is emitted in random direction. At event 2, a fission interaction takes place which results in termination of the neutron and emission of two neutrons and one photon. The first neutron emitted in event 3 is absorbed and the second neutron at event 4 escapes from the system. The photon in event 5 is scattered before it escapes from the material.

Now, all the described previous events are one neutron tracking history from source to death. Therefore, for better results that can estimate the true value, more neutrons histories are required [15]. In general, the uncertainty in the calculation decreases inversely proportion to the square root of the number of histories.

### 2.4.2 Diffusion equation

Another method for solving the NTE is by using a deterministic method, in this case the diffusion approximation. This method is widely used in the field of the reactor core calculation for solving reactor core physics parameters and fuel burnup calculations. To reduce the computational load and the NTE complexity for solving the neutron flux, the neutron diffusion equation employs approximations on the neutron transport equation. Those are: neutrons inside the reactor behave in the same way as solute in a solution. For instance, if the neutron flux is concentrated at one point along $x$-axis Fick's law that describes the net number of neutrons passing through an area per unit time is

$$J_x = -D\frac{d\phi}{dx}, \tag{2.7}$$

where $J_x$ is the net number of neutrons per unit area per time $n/\text{cm}^2\text{s}$, $D$ is the diffusion coefficient in cm. The Fick's law diffusion approximation is not valid under: strong absorption, near the surface and when there is a strongly anisotropic scattering.

In a 3D calculation the Fick's law becomes a gradient of the flux which then can be replaced by the leakage to have one equation with

one unknown. Now, the diffusion equation can be written as

$$\frac{1}{\upsilon}\frac{\partial\phi(\vec{r},t)}{\partial t} - D\nabla^2\phi(\vec{r},t) + \Sigma_a\phi(\vec{r},t) = \nu\Sigma_f.\phi(\vec{r},t) \qquad (2.8)$$

Furthermore, some approximations have been implemented in the equation such as $P_1$ angular flux approximation, isotropic neutron sources, and isotropic scattering [16].

### 2.4.3 Photon interaction and transport

The photon transport mode in Serpent is utilized whenever photon heating studies are performed. Serpent provides several features for the photon transport mode such as a coupled neutron-photon transport mode, radioactive decay source mode and bremsstrahlung emission by beta particles. There are four main types of photon interactions such as photoelectric effect, Compton scattering, Rayleigh scattering, and electron-positron pair production.

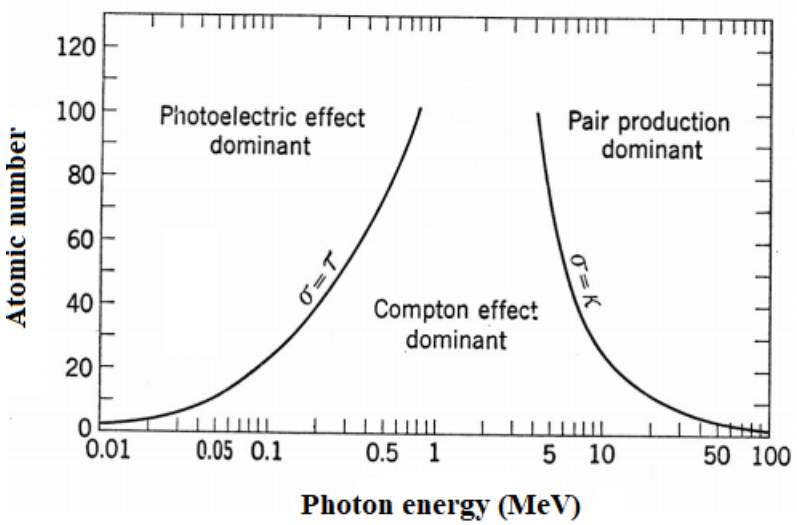


FIGURE 2.5: Regions of the photoelectric effect, Compton scattering, and pair production with respect to the photon energy and atomic mass number.

The Monte Carlo photon particle transport method follows each photon in a random walk process with the Markov property. Photons travel in straight lines between interaction sites in a geometry which consists of homogeneous material regions with well-defined boundaries. Photon interacts with matter as they would occur with individual atoms, ignoring any molecular or lattice structure effects. In addition, the secondary photons in Serpent-2 are created in electron-positron annihilation, atomic relaxation and bremsstrahlung of electrons and positrons [17].

## 2.5 Computer codes used in this study

The computational tools that were used in this study are: (i) OSCAR-4, which is comprised of two internal codes named as HEterogeneous Assembly DEpletion (HEADE) code and Multi-Group Reactor Analysis Code (MGRAC) code; and (ii) Monte Carlo particle Serpent-2 and MCNP-6.2 code system. These codes are briefly described in this section.

### 2.5.1 OSCAR-4 code system

The OSCAR-4 approach to compute the neutron population distribution in MNR core is to divide the reactor into relatively large volumes called neutronic nodes. In each node, a set of spatially homogeneous "equivalent" few-group parameters is assigned. The homogeneous and few-group/energy condensation can be defined according to Generalized Equivalence Theory; They are used in MGRAC and are flux-volume weighted. For instance, the energy condensation,

and spatial homogenization of a macroscopic cross section can be defined as follows:

$$\Sigma_g = \frac{\int_V \int_{E_1}^{E_2} dV dE\, \Sigma_t(E)\phi(E)}{\int_V \int_E {}_1^{E_2} dV dE\, \phi(E)}, \tag{2.9}$$

where $\Sigma_g$ represents the general integral energy condensation and spatial homogenization for any mixture of material with neutron energy between $E_1$ and $E_2$. OSCAR-4 separates the homogenization procedure into two independent phases, namely a radial and an axial homogenization phase. Radial homogenization takes place at the 2-D lattice physics level where the spatial heterogeneity in the radial plane are explicitly modeled in 2-D transport theory calculations for each assembly segment type (fuel and non-fuel). The homogenization of the axial heterogeneity of any assembly is based on 1-D diffusion theory within the whole core calculations. The axial heterogeneities in any given fuel assembly or reflector are represented by layers of varying heights, the heights being determined by the superpositioning of exposure nodes, in this work the axial fuel was divided into seven layers. Each of the axial layer is treated as a homogeneous region with constant cross-sections. The solution of this axial 1-D few-group diffusion equations is based on the Multi-group Analytic Nodal Method (MANM) with transverse (radial) leakages treated as effective absorption cross-sections or as fixed sources. Finally, the equivalent homogeneous axial side fluxes that are needed to compute axial discontinuity factors are determined from the analytic solution of a two-point boundary problem for each homogenized neutronic node [18]. The following Figure depicts the OSCAR-4 calculational tool in each part of the calculation.

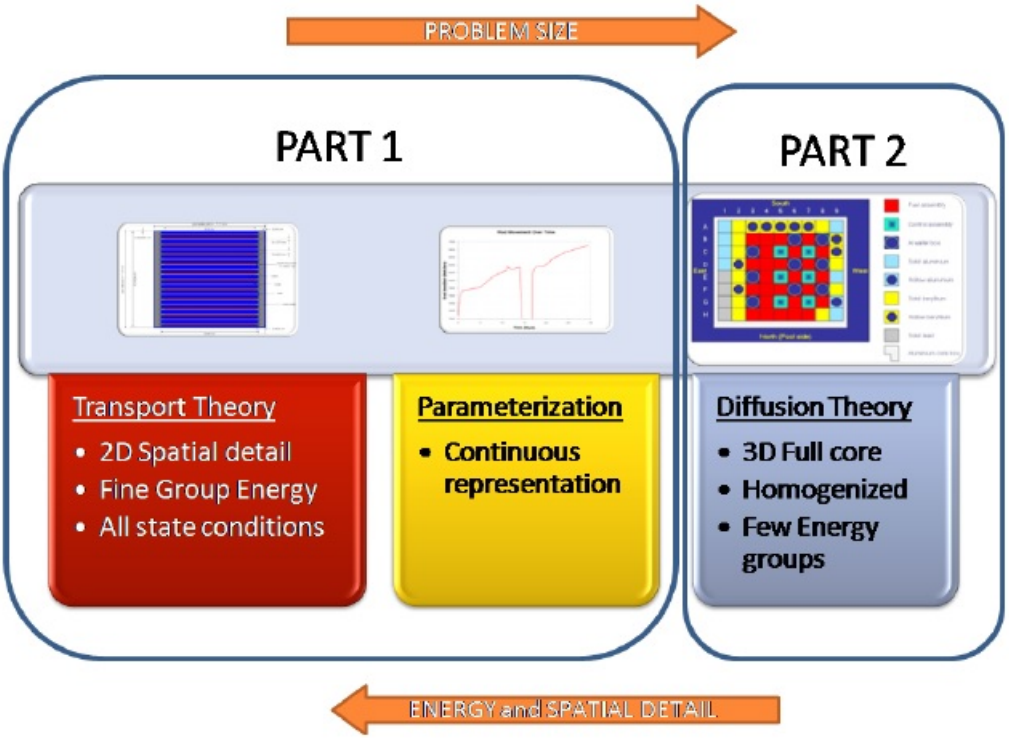


FIGURE 2.6: OSCAR-4 calculational path [18].

**HEADE code**

HEADE is a 2D code that is used to generate a few-group homogenized cross section. It is the first step in the calculational path of the OSCAR-4 system. HEADE uses the collision probability (CP) method to solve the NTE. The method of the CP is applied into partitioned discrete meshes or volumes in which flux and cross section are constant. In general, the CP method can be formulated using the integral transport equation and can be written as [19]

$$\Phi_i = \sum_j T^{j \to i}[(\Sigma_{sj} + \nu\Sigma_{fj})\Phi_j + S_{0j}], \tag{2.10}$$

where $T^{j\to i}$ here relates the fluxes by the probabilities and can be written as

$$T^{j\to i} = \frac{1}{V_i}\int_{V_i} dr_i \int_{V_j} dr_j \frac{e^{-\alpha(r_i,r_j)}}{4\pi|r_i - r_j|^2} \tag{2.11}$$

Where the optical path length $\alpha$ is

$$\alpha(r_i, r_j) = |\int_{r_i}^{r_j} \Sigma_t(R)dR| \tag{2.12}$$

The McMaster Nuclear Reactor (MNR) fuel is an MTR-fuel type which constitutes of 18 plates of which 16 are fueled with Low Enriched Uranium (LEU), and two peripheral dummy aluminium plates. The 2D calculation in fuel assembly (FA) using HEADE was carried out by dividing the cross sectional fuel into meshes as seen Figure 2.7

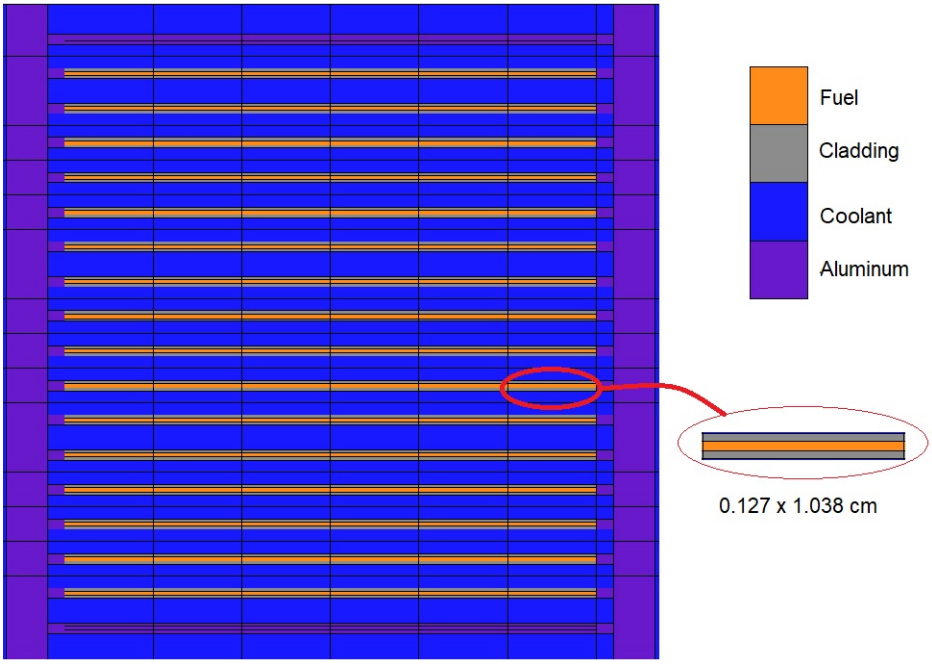


FIGURE 2.7: Fuel assembly generated by HEADE.

Figure 2.7 shows an example of a lattice cell that contains three meshes in the $y$-direction: fuel meat in the center with 0.051 cm

thickness, and aluminum cladding with 0.038 cm on either side (total 0.127 cm); and one mesh in the $x$-direction of 1.038 cm.

In the HEADE code, group homogenized cross-sections and nodal equivalence parameters, needed by the global core diffusion solver, are generated. In addition, collapsed few-energy parameters are calculated for each material type in the reactor.

**Multi-Group Reactor Analysis Code (MGRAC)**

The MGRAC code is the final step required to complete the OSCAR-4 run. In this part, a 3D full core assembly layout is defined, constructed of various assembly types based on the cross-section mixtures available in the LINX library. In order to successfully run the MGRAC code, several files have to be defined for each fuel, reflector, and surrounding regions. Those are:

- CONFIG file - describes the core geometric layout.
- LOAD file - describes the placement of the elements prior to the start of the cycle.
- BASE file - describes the axial material structure of a given base assembly type.
- HIST file - describes the isotopic data of an actual, named assembly.
- INPUT file - describes the cycle/scenario to be simulated - hence power levels, rod positions, depletion steps, etc.

The global diffusion calculation MGRAC would contain a number of assemblies placed within configurations somewhat different from the idealized infinite medium lattice applied in the HEADE calculation, and hence, equivalence is partially lost.

In this part, the Beggining of cycle (BOC) and End of Cycle (EOC) along with the reactor plant data are specified in order to determine core-follow parameters. One of the important parameters is fuel burnup. The fuel burnup calculation used in OSCAR-4 is a predictor corrector method. This method is based upon two-step calculations performed at the beginning and the end of each step. The flux and cross section at the beginning of the step are used to deplete the fuel, and then the flux and cross section at the end of the step are calculated. In the predictor corrector method, the averages of the two parameters are used to deplete the fuel.

**OSCAR Analysis System (OASYS)**

Up to the last section, OSCAR core calculation for any given cycle can be completely performed. However, for such a large number of cycles, the reactor modelling automation with OASYS needs to be utilized. The OASYS code uses the automation capabilities in the OASYS system to perform the necessary corefollow calculation for the past cycle, and then perform the reload analysis calculation for the coming cycle.

### 2.5.2 Serpent-2 Modelling of the MNR

The MNR Serpent-2 model includes the reactor core, the reflector and the surrounding beams – all of which are modelled explicitly as described in the MNR facility specification report [20]. The nuclear data library used in this model is ENDF/B-VII.1 [21].

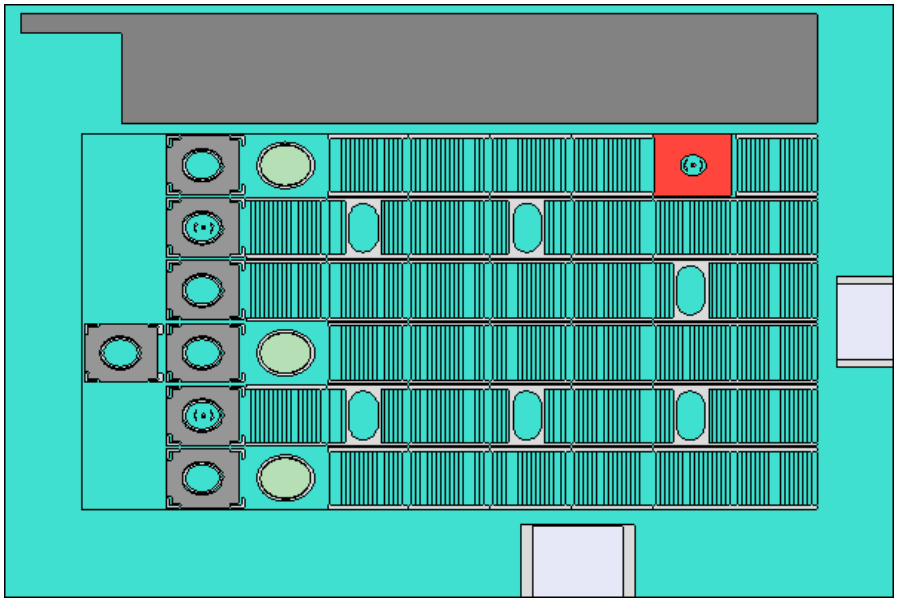

FIGURE 2.8: MNR Serpent-2 model.

The predictor-corrector approach was used for burnup calculations. In addition, to take into consideration spatial distribution of burnup, each fuel assembly was divided into seven axial zones with different material numbers. This will calculate the flux and the reaction rates over each axial burnup zone per fuel assembly. Also, the initial number densities used in this work were obtained from this study since the starting core used in this study (Core 54A in 2007).

One major setback for burnup in the Serpent code aside been computationally expensive, is its difficult to take into consideration the movement of the control rods during burnup which affects the flux shapes and power distribution in the core. This is however important for core-follow calculations as the control rods degree of withdrawal are regularly moved during reactor operations. This drawback was also investigated in this research and an appropriate method was

suggested to do the core-follow calculation burnup.

**Serpent-2 energy deposition calculation**

The Serpent-2 code offers four different modes (0-3) with different combination of accuracy and time requirement. In mode 0 and 1, all energy is deposited at fission sites. The only difference between them is that mode 0 deposits a constant energy per fission; whereas the mode 1 gives components of energy release due to fission as a function of incident neutron energy. These two modes produce inaccurate energy deposition since all energies are deposited locally. In mode 2, offers an improvement to the accuracy by providing the neutron energy deposition along its history. However, in this mode, the photon energy is deposited locally at the fission sites.

The most accurate mode 3 in Serpent-2 was used in this work. This modes adds photon heating deposition which is scored after each interaction by any of the three photon interaction methods, photoelectric effect, Compton scattering and pair production. The delayed photon heating can be calculated using any of the two methods either assuming the delayed gammas is deposited with the same distribution as the prompt gammas and hence use the correction factor, or by solving the Bateman equations which gives more accurate energy deposition of delayed gamma. The two methods of delayed gammas were utilized in this dissertation.

### 2.5.3 MCNP-6 modelling of the MNR

The MCNP-6 model of the MNR core was primarily developed in 2001. Prior this thesis, the last updated core was received for the

cycle 54A (2007). A continuous updating to reflect various changes in the geometry and material compositions were carried out. In this thesis, emphasis was placed on the updating the core materials. Figure shows the MCNP-6 model for the MNR core.

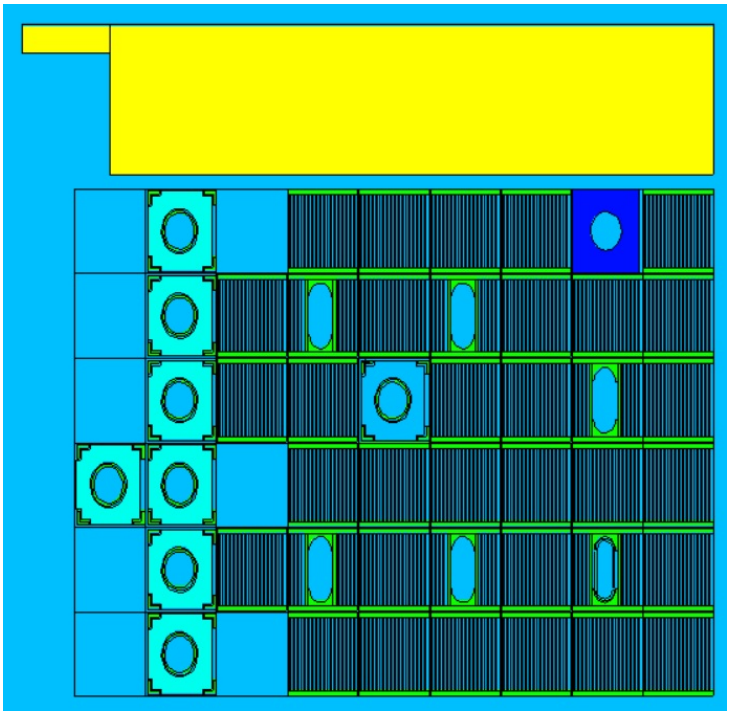

FIGURE 2.9: MNR core using MCNP-6.

One geometrical simplification was implemented in MCNP-6 and Serpent-2 models: the representation of the curved fuel plates with non-curved plates. This approximation was judged to have little physical significance and the rest of the model is a correct representation of the core geometry.

#### MCNP-6.2 energy deposition

The energy deposition tally utilized in this work by MCNP-6.2 is the F6 tally, where the neutron and photon energy deposition is

determined using the heating numbers from the nuclear data tables. These heating numbers are estimates of the energy deposited per unit track length. This tally includes all reactions and scores interact at the point of interest. The general description of this tally can be seen in the following equation

$$F6 = \frac{1}{V}\int_V \int_E \int_t H(E)\Phi(r, E, t)dEdtdV \tag{2.13}$$

where H(E) is the heating response in MeV/g, depends on the particle type. This tally is merely track-length estimators of the flux with an energy-dependent multiplier, H(E). The heating tally is merely flux tally multiplied by an energy-dependent multiplier (FM card). The heating response H(E) is calculated depending on the context, neutron or photon, as follow

$$H(E) = \sigma_t(E)H_{avg}(E) \tag{2.14}$$

where $H_{avg}$(E) for neutron and photon is

$$H_{avg}(E)_n = E - \Sigma_i p_i(E)[\bar{E}_{out}(E) - Q_i + \bar{E}_\gamma(E)] \tag{2.15}$$

$$H_{avg}(E)_\gamma = E - \Sigma_i^3 p_i(E)[\bar{E}_{out\gamma}] \tag{2.16}$$

where $H_{avg}$ is the heating number, $\sigma_t$ is the total cross section, $p_i(E)$ is the reaction probability of i (Compton scattering, pair-production, photoelectric), E is the incident neutron energy, $\bar{E}_{out}$ is the average exiting energy,neutron or photon, for reaction i with incident neutron energy E, $E_\gamma$ is the average gamma emission energy and $Q_i$ is the Q-value of reaction i.

# Chapter 3

# OSCAR-4 Code System Comparison and Analysis with a First-Order Semi-Empirical Method for Core-Follow Depletion Calculation in MNR

Citation:

M. Alqahtani, S. Day, and A. Buijs, 2019, "OSCAR-4 Code System Comparison and Analysis with a First-Order Semi-Empirical Method for Core-Follow Depletion Calculation in MNR", Canadian Nuclear Laboratories Nuclear Review, 9 (1), pp. 73 - 82. doi: 10.12943/CNR.2019.00011.

This paper introduces the three-dimensional reactor core analysis code OSCAR-4 developed by the South African Nuclear Energy Corporation (Necsa). The OSCAR-4 code was used to calculate and verify the fuel inventory against the MNR core operational data. The comparison results between OSCAR-4 code and the MNR operational data were in good agreement with small divergence along the period of the comparison (three years). Lacking of the consideration of Pu-239 in LEU-type fuel will cause a higher consumption in U-235 and as a result a variation in the fuel inventory evaluation in the two methods. For the purpose of this thesis, the fuel composition needed as inputs to the simulation codes have to improve this prior to any future comparisons with the MNR core.

FULL ARTICLE

# OSCAR-4 CODE SYSTEM COMPARISON AND ANALYSIS WITH A FIRST-ORDER SEMI-EMPIRICAL METHOD FOR CORE-FOLLOW DEPLETION CALCULATION IN MNR

**Mohammed Alqahtani[1,2]*, Simon Day[1], and Adriaan Buijs[1]**

[1]McMaster University, Hamilton, ON L8S 4L8, Canada
[2]Nuclear Science Research Institute (NSRI), KACST, Riyadh, Saudi Arabia

**Article Info**
Keywords: $k_{eff}$, depletion calculation, flux-wire estimate, OSCAR-4.
Article History: Received 10 May 2019, Accepted 30 October 2019, Available online 16 June 2020.
DOI: http://dx.doi.org/10.12943/CNR.2019.00011

*Corresponding author: alqahm1@mcmaster.ca

*Knowledge of the isotopic composition of a nuclear reactor core is important for accurate core-follow and reload analysis. In the McMaster Nuclear Reactor, fuel depletion estimates are based upon a semi-empirical calculation using flux-wire measurements. These estimates are used to plan and guide fuelling operations. To further support operations, an OSCAR-4 model is being developed. To evaluate the performance of the OSCAR-4 code for this application, 2 points of comparison, considering the period between 2007 and 2010, are presented: (i) the multiplication factor $k_{eff}$ and (ii) U-235 fuel inventory. The latter is compared with a simple first-order semi-empirical calculation. The calculation of $k_{eff}$ for the last operational 3 months yields $0.997 \pm 0.002$ (vs. 1.000 for an operating reactor), and differences in both core-average inventory and the maximum standard fuel assembly inventories estimates are found to be 5.7% and 7.5%, respectively.*

CNL Nuclear Review Downloaded from pubs.cnl.ca by 76.64.227.45 on 02/05/21
For personal use only.

## 1. Introduction

The McMaster Nuclear Reactor (MNR) is a light-water moderated material testing reactor (MTR) used for, among other things, the production of the medical radio-isotope I-125, neutron radiography, reactor physics experiments, and education and training purposes [1]. The standard operating schedule at MNR is two 8-hour shifts per day, Monday to Friday, with an extra shift on some Saturdays.

The in-core fuel management in MNR is an important task for keeping the reactor operation optimal for isotope production and for running experiments. This includes fuel reload and fuel shuffling, which can be carried out with the goal of satisfying certain criteria, such as boosting the neutron flux in the irradiation positions and beam tubes and meeting safety constraints and economic parameters. In MNR, prior to fuel reload or shuffling, the fuel inventory of U-235 for each standard fuel assembly (SFA) is estimated from a flux-wire measurement and the preceding operation cycle energy output.

As part of the overall system for calculation of reactors (OSCAR-4) code validation, the fuel composition must be estimated adequately. The purpose of this study is two-fold: (*i*) testing the OSCAR-4 code model, this is done by seeing how the code predicts $k_{\text{eff}} = 1$ as this is an actual value to compare against the reactor operation, using the critical rods positions, and (*ii*) examining the fuel composition with depletion including a comparison against a first-order semi-empirical approach.

## 2. The MNR

MNR is a light-water cooled and moderated plate-fuel reactor with a U-235 enrichment of 19.75% and a maximum neutron flux of $5.8 \times 10^{13}$ n/cm$^2$ s [1]. It is licensed to operate at a power up to 5 MW$_{\text{th}}$. The nominal power is 3 MW$_{\text{th}}$. Reactivity within the MNR core is controlled by 5 silver–indium–cadmium (Ag–In–Cd) shim-safety rods and 1 stainless steel regulating rod. The core is comprised of MTR-type fuel assemblies arranged in a $9 \times 6$ grid plate [1]. Cooling of the core is

CNL Nuclear Review Downloaded from pubs.cnl.ca by 76.64.227.45 on 02/05/21
For personal use only.

TABLE 1. A general description of the MNR facility and core specifications [3].

| Parameter | Specification |
|---|---|
| Type of reactor | Open-pool MTR |
| Maximum/nominal power | 5/3 $MW_{th}$ |
| Maximum neutron flux (3 MW) | $5.8 \times 10^{13}$ n/cm$^2$ s |
| Coolant and moderator | Light water |
| Reflector | Graphite and beryllium |
| Coolant circulation | Natural circulation or forced downward flow |
| Fuel type | $U_3Si_2$-Al dispersion Al-clad curved plate fuel |
| Fresh SFA and CFA atom density | $1.89 \times 10^{-3}$ and $1.67 \times 10^{-3}$ at/b.cm |
| LEU enrichment | 19.75% |
| HEU enrichment | 93% |
| Control system | 5 Ag-In-Cd shim safety rods and 1 stainless steel rod |

achieved at low power via natural circulation and at high power via forced down-flow driven by the hydrostatic head of the pool and returned by a pump. An MNR SFA contains 18 curved plates, the inner 16 of which contain fuel while the 2 outer (dummy) plates are aluminium. The MNR control fuel assembly (CFA) contains 9 fuelled plates, leaving space for an absorber rod in the center. The SFA and CFA share the same outer assembly dimensions, differing only in material specifications and number of plates. Lattice spacing on the MNR grid is 8.100 cm × 7.709 cm radially. The core has an active height of 60 cm. A row of graphite assemblies acts as a reflector on 1 side of the core, while the other sides are flanked by a lead block and 6 radial beam tubes [1]. Table 1 presents the general core specifications of the MNR.

For the nonproliferation of nuclear materials, MNR started to convert the fuel to low enriched uranium (LEU) in 1998 on a burnup basis and was totally converted to LEU in 2007.

## 3. Calculational Tool

### 3.1. The OSCAR-4 code system

The OSCAR-4 was developed and is supported by the Radiation and Reactor Theory section of Necsa (South Africa Nuclear Energy Corporation) [2, 3]. The code is comprised of 3 main modules: CROGEN, CROLIN and CORANA.

The CROGEN module includes the 2-D lattice code HEADE that uses the collision probability method to solve the neutron transport equation to generate multi-group cell cross-sections and nodal parameters based on a WIMS-E 172-group cross-section library. The MNR model adopts a 6 group structure that is used by Necsa for the SAFARI-1 reactor. Cell data are then passed to the CROLIN module, which uses the POLX and LINX codes to paramatrize (POLX code) the multi-group cell data and link it (LINX code) into a runtime library used by the core solver. The core analysis module, CORANA, uses the nodal diffusion theory solver MGRAC (multi-group reactor analysis code). MGRAC compiles all the geometry (CONFIG), fuel load (LOAD), axial levels (BASE), and history (HIST) of the assemblies and produces a 3-D core solution. A schematic of the subset of the OSCAR calculation path used in this study is shown in Figure 1.

MGRAC can perform both snapshot flux and reactivity solutions, as well as cycle depletion analysis. Depletion is conducted in a quasi-static fashion, using alternating flux and burnup calculations. A predictor–corrector scheme is used to capture the nonlinear impact of changing number densities on flux, and step sizes are limited by the rate of change of plant data (rod positions, power levels, etc.). This process is largely automated using the OASYS (OCSAR analysis system) as illustrated in Figure 2.

One of the inputs to OASYS is the reactor operation history (plant data), such as reactor power, operation time, control rod positions, shutdown times, number of time steps per burn step, Xenon tracking/equilibrium, and critical rod searching. In this study, the plant data for MNR operation are captured in 1 log entry per day (12–14 hours burn step). Each entry includes the reactor power and start-up critical rod positions (1 position for the low-worth regulating rod and 1 for the gang-operated shim-safety rods). Because of the xenon transient in each day, MNR absorber rods are repositioned several times each day. In this study a single core-follow timestep was used per operational day with daily average extraction rod positions to account for the rod movement. This is adopted to improve tracking the axial profile of each fuel assembly compared with using the start-up rod

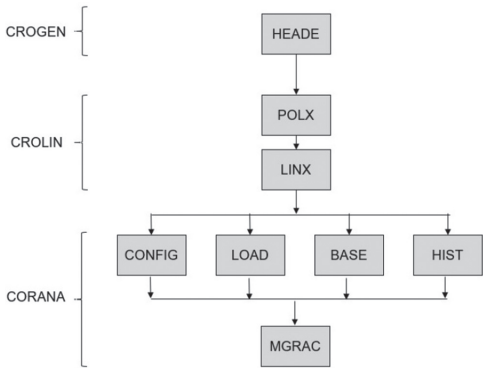


FIGURE 1. OSCAR-4 reactor calculational path for MNR.

CNL NUCLEAR REVIEW
VOL 9, NUMBER 1, DECEMBER 2020



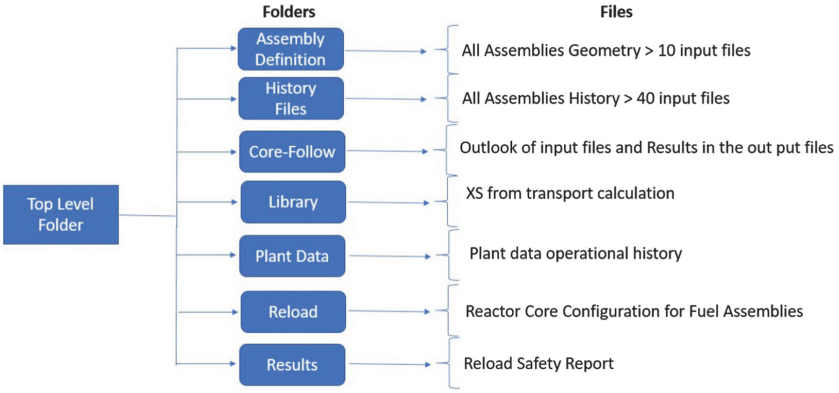


FIGURE 2. OASYS database structure.

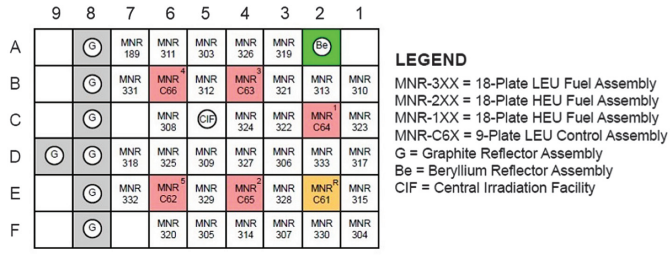


FIGURE 3. MNR core grid configuration, cycle 54A.

CNL Nuclear Review Downloaded from pubs.cnl.ca by 76.64.227.45 on 02/05/21
For personal use only.

positions for the entire burnup timestep. In contrast, the critical rod positions, which is the position at the reactor start-up, were used for the $k_{\text{eff}}$ predictions. Figure 3 presents the first core configuration of the first cycle.

## 4. Methodology

### 4.1. The first-order semi-empirical method (FOSEM)

As part of fuel management activities at MNR, a set of short-length Mn–Cu flux wires are inserted into the coolant channels, as shown in Figure 4, of each SFA and activated at low power [4]. This activation profile is used to estimate the power profile of the core which in turn is available for use in fuel consumption estimates. The wire holder design is such that a collar stops the holder at the top of the fuel plates and consistently positions the flux wire near the axial centerline of the active height of the core. The flux wires are then irradiated at low power, typically 200 W, for about 10 minutes. The activation reaction induced in the wires is described by the following equation:

$$^{55}\text{Mn} + n \rightarrow {}^{56}\text{Mn}(2.58h) + \gamma \quad (1)$$

After the radial wires are irradiated, they are removed. The activity induced in the $^{56}$Mn is counted using an NaI detector system. Each wire is measured twice and the background is subtracted. The measured activity is then converted into a relative flux distribution across the reactor core. With that, given that the cycle length and reactor power are known from reactor operation data, the fuel depletion at the end of cycle (EOC) for each fuel assembly can be estimated. A simplistic approach to a fuel consumption estimate assumes all fission power coming from U-235 thermal fission and leads to the following equation.

$$M_{235} = M^*_{235} - CX \quad (2)$$

where $M_{235}$ and $M^*_{235}$ are the U-235 amounts in gram at the EOC and beginning of cycle, respectively; $C$ is the consumption value in g/MWh; and $X$ is the total energy released up to the EOC in MWh. This semi-empirical method was used

CNL NUCLEAR REVIEW
VOL 9, NUMBER 1, DECEMBER 2020



CNL Nuclear Review Downloaded from pubs.cnl.ca by 76.64.227.45 on 02/05/21
For personal use only.

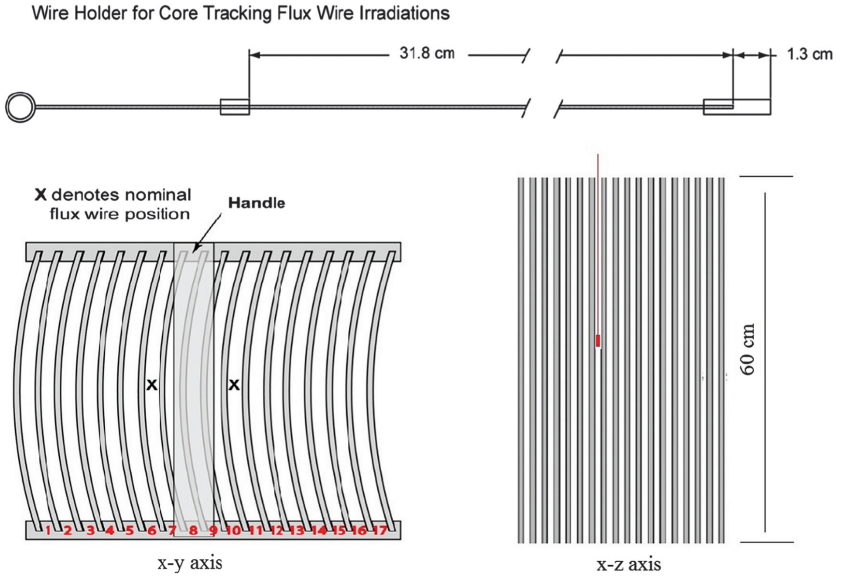


FIGURE 4. Wire holder (top), *x–y* and x–*z* views of a fuel assembly.

at MNR for high enriched uranium (HEU) fuel cycle calculations, with a value of $C = 0.05417$ g/MWh of U-235. It is herein investigated in comparison with the OSCAR-4 simulation approach in light of the current LEU fuel cycle.

The assumptions made in the flux-wire estimate of the fuel depletion are: (*i*) the flux wires are consistently positioned in the central coolant channel of each SFA, (*ii*) the assembly average fission rate is proportional to Mn activation in the central coolant channel, (*iii*) the activation distribution is representative of an average flux distribution over the operating cycle, and (*iv*) burnup occurs only by U-235 fission.

### 4.2. Modelling MNR in OSCAR-4

The work described here considers MNR operational data from 2007 until 2010, starting with Core 54A (February 2007). This core configuration contained only 1 HEU SFA and 36 LEU FAs (30 SFAs and 6 CFAs) at different degrees of fuel burnup.

The MNR OSCAR-4 model is based on the one developed by NECSA for a 2008–2011 IAEA Coordinated Research Project [5], used for calculation of Core 54A characteristics. This model has been only slightly modified and is applied to core-follow cases for multiple reactor cycles in the work herein.

The MNR core model is defined as a $12 \times 11$ rectangular node grid. Each in-core node is associated with a grid position in the MNR grid plate, housing a single type of core component (e.g., fuel, reflector, irradiation position). The ex-core nodes are of the same dimension and extend the model 3 nodes (roughly 24 cm) beyond the grid plate. Ex-core nodes include those for beam tubes and the gamma shield lead block.

The active height of the core is divided into 7 axial layers of 8.57 cm each, see Figure 5, allowing for the capture of the axial variation in fuel consumption. The axial reflector (i.e., above and below the active core) is modelled by 2 additional layers, a homogeneous light water and aluminum blend (6 cm), and light water (9 cm). The MNR model here is $15 \times 12$ assemblies, adding up to 1260 calculational nodes, and with 31 standard fuel assemblies and 6 control fuel assemblies, adding up to 259 fuel calculation nodes. Initial number densities for each element over the 7 layers were taken from the in-house empirical approach.

The MNR 18-plate SFA was modelled as an infinite lattice on a 2-D Cartesian mesh. All 18 plates, as well as the side plates and side water, were captured explicitly. Apart from ignoring the curvature of the fuel plates, the fuel assembly was modelled as per nominal dimensions. The span or width of the fuel plates was dictated by the distance maintained between

CNL NUCLEAR REVIEW
VOL 9, NUMBER 1, DECEMBER 2020



CNL Nuclear Review Downloaded from pubs.cnl.ca by 76.64.227.45 on 02/05/21
For personal use only.

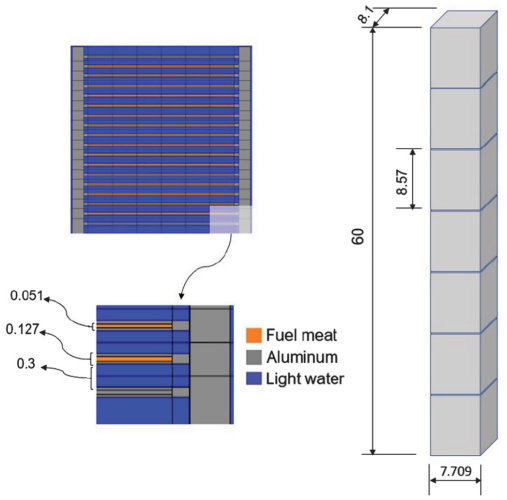


FIGURE 5. Axial fuel nodes or burnup zones used for core-follow calculations (all in cm).

the 2 side plates. Similarly, the nominal thickness of the fuel plate, including that of the clad and fuel meat, is maintained. Side plate dimensions were also conserved, requiring a thin row of cells beyond the 2 dummy plates to capture the small amount of water that exists beyond the ends of the side plates. Each fuel plate was divided into 8 sub-cells (meshes), the middle 6 containing fuel meat (around 1.038 cm each) and the outer 2 composed of only the extension of the clad between the fuel meat and the side plates.

For the reflector assemblies and ex-core structures some approximations were made for the complexity of the model geometry, necessitated by the restrictions of using a 2-D cartesian geometry code. In all cases material volume was conserved. The graphite and beryllium reflector model geometries are shown in Figures 6 and 7. The model for the central irradiation position is identical to that for the graphite reflector assembly with only the graphite material replaced by light water. The ex-core regions, i.e., beyond the MNR Grid Plate, which include structure such as the beam tubes and lead block, were modelled by conserving the volume of the different materials.

The HEADE code was used to produce a set of homogenized microscopic cross-sections. HEADE uses 38 isotopes that are important isotopic fission and actinide chains in the reactor calculation. Additionally, HEADE considers all the other isotopes lumped into a single structural macroscopic material. The energy group structure used was the 6-neutron energy group structure (HEADE uses nuclear data from the WIMS-E 172-group library, which were then collapsed into 6 groups for this study) [6].

## 5. Start-up Critical Rod Positions

The operational data of MNR are recorded on a daily basis. The information provides (*i*) reactor power, (*ii*) control rod extraction in 30 minute periods during the operation, and

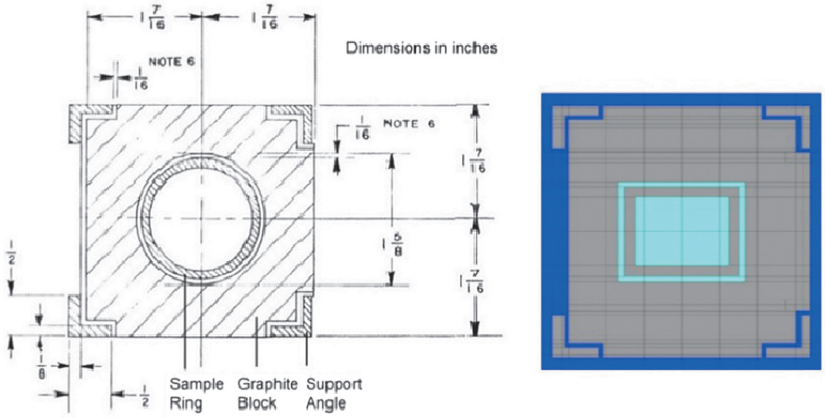


FIGURE 6. Actual and modelled graphite assembly. The left diagram was obtained from reactor drawings and presented also in Day [1].

CNL NUCLEAR REVIEW
VOL 9, NUMBER 1, DECEMBER 2020



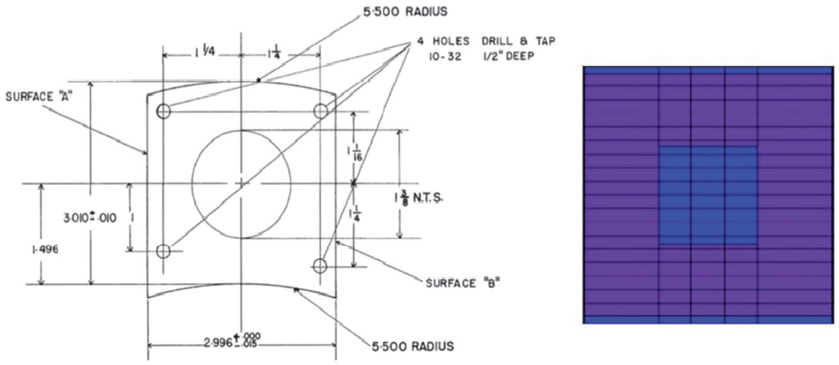


FIGURE 7. Actual and modelled Be assembly. The left diagram was obtained from reactor drawings and presented also in Day [1].

TABLE 2. MNR operational data for the first week of the cycle 54A, 2007.

| Date | Power ($MW_{th}$) | Start-up time (hh:mm) | Shim CRs (%) | Reg. CR (%) | Shut-down time (hh:mm) |
|---|---|---|---|---|---|
| Monday, 26 February 2007 | 3 | 11:14 | 77 | 50 | 22:45 |
| Tuesday, 27 February 2007 | 3 | 8:36 | 96 | 70 | 22:45 |
| Wednesday, 28 February 2007 | 3 | 9:06 | 100 | 100 | 22:45 |
| Thursday, 1 March 2007 | 3 | 9:02 | 100 | 70 | 21:30 |
| | 2 | 21:30 | 100 | 65 | 22:45 |
| Friday, 2 March 2007 | 3 | 8:46 | 100 | 70 | 22:45 |
| Saturday, 3 March 2007 | — | — | — | — | — |
| Sunday, 4 March 2007 | — | — | — | — | — |

(*iii*) the total time of the reactor operation. Table 2 illustrates an example of the first few days from the operational data that was used for this investigation.

Table 2 presents sample data of the first week of this calculation from the control room data sheet. These data show the start-up extraction position. The data used for this study are extending until January 2010. The calculation in this study evaluates all the available data, which is extending up to January 2010. These data were used to test and compare the $k_{eff}$ values for each day to the actual value. In contrast, a daily average control rod extraction was used for the depletion calculation. More detailed Operations data that records rod positions every 30 minutes, were used to calculate the daily average positions.

## 6. Results and Analysis

### 6.1. OSCAR4 $k_{eff}$ calculation

The first comparison made with the MNR operational data is the effective multiplication factor at the critical control rod positions (start-up). MNR experiences xenon poisoning in the early hour during the weekdays. Therefore, the control rod positions in the start-up, after the night-shift shutdown, are usually extracted higher than the rest of the day to achieve the criticality. In this model, MGRAC treats the xenon concentration explicitly. Figure 8 shows the $k_{eff}$ at the critical rod positions for the daily operational data covering the entire period of study. Owing to the long-documented data for this study, about 1050 days of information including shutdown days, Figure 8 presents solely the operational days.

Figure 8 shows the calculated $k_{eff}$ values and the control rod positions extracted from the operational data (Table 2). The tracked data contain 31 cycles with a total of 738 operational days of the core-follow calculation. The total core burnup between the beginning and the end of this calculation is 33.1 MWD/kg, and about 1279 MWD energy was released. A number of trends are evident in Figure 8. Firstly, there appears to be a day-to-day variation in the critical $k_{eff}$ estimates related to the specific day of the week. All the $k_{eff}$ peaks, or control rod valleys, can only be found on Mondays.



CNL Nuclear Review Downloaded from pubs.cnl.ca by 76.64.227.45 on 02/05/21
For personal use only.

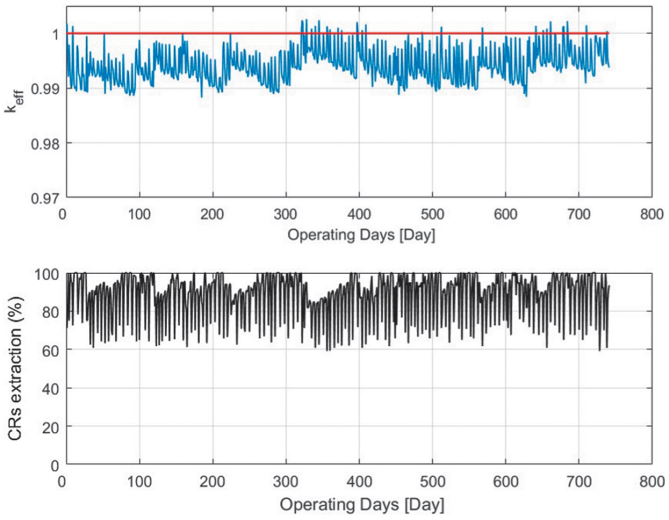


FIGURE 8. $k_{\text{eff}}$ and critical rod position (% extraction) vs. operating days.

TABLE 3. Multiplication factor and its standard deviation for 8 points average.

| Operation days | $k_{\text{eff}} \pm \sigma$ |
|---|---|
| 1–92 | $0.99296 \pm 0.00191$ |
| 93–185 | $0.99437 \pm 0.00049$ |
| 186–278 | $0.99609 \pm 0.00123$ |
| 279–371 | $0.99529 \pm 0.00043$ |
| 372–463 | $0.99518 \pm 0.00031$ |
| 464–555 | $0.99351 \pm 0.00136$ |
| 556–647 | $0.99517 \pm 0.00031$ |
| 647–738 | $0.99684 \pm 0.00196$ |

Secondly, the cycle trend of the $k_{\text{eff}}$, which varies from 7 to 80 days per cycle, is decreasing, i.e., the calculated critical $k_{\text{eff}}$ decreases per cycle. These 2 observations can be explained by inconsistencies between rod worth and xenon worth in the model. In contrast to Mondays, the xenon concentration is considerably high during the start-up for all operating days. This will lead to extraction of the control rods to compensate for the negative reactivity in the core, contrary to Mondays, when xenon concentration is significantly low after 40–50 hours of shutdown. Thirdly, the overall trend of the $k_{\text{eff}}$ is improving, i.e., getting closer to unity. Unlike FOSEM, the core inventory tracking is considering all the major isotopes inventory that are neutronically important. Table 3 presents 8 values of $k_{\text{eff}}$, each is averaging 92 operational days along with its standard deviation to the total average.

### 6.2. Tracking comparison of U-235 contents in MNR core and a fuel assembly

The next stage of the analysis involved comparison of depletion estimates derived from the FOSEM estimates with those from the OSCAR-4 model. In this calculation we use the control rod average insertion during the reactor operation. This is thought to be an improvement on the approach used for the $k_{\text{eff}}$ estimates described previously. Table 4 shows each date of the data available in MNR for each EOC. These data are plotted in Figure 9 along with the OSCAR-4 calculation.

TABLE 4. EOC first-order semi-empirical method date.

| Cycle I.D. | EOC (day/month/year) |
|---|---|
| 54A | 27/03/2007 |
| 54B | 30/04/2007 |
| 55A | 25/06/2007 |
| 55B | 02/08/2007 |
| 55C | 03/10/2007 |
| 55E | 07/01/2008 |
| 55F | 07/04/2008 |
| 55G | 17/06/2008 |
| 56A | 29/09/2008 |
| 56B | 05/01/2009 |
| 56C | 09/03/2009 |
| 56D | 13/05/2009 |
| 56H | 08/01/2010 |

CNL Nuclear Review Downloaded from pubs.cnl.ca by 76.64.227.45 on 02/05/21
For personal use only.

CNL NUCLEAR REVIEW
VOL 9, NUMBER 1, DECEMBER 2020



CNL Nuclear Review Downloaded from pubs.cnl.ca by 76.64.227.45 on 02/05/21
For personal use only.

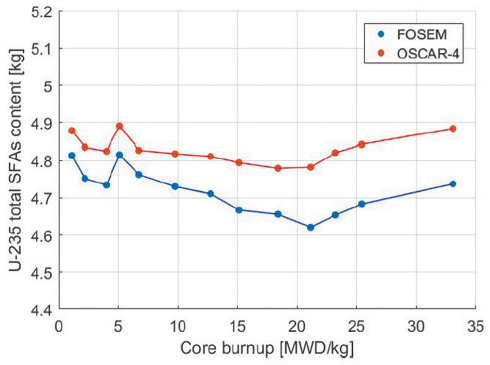


FIGURE 9. Total SFAs U-235 inventory.

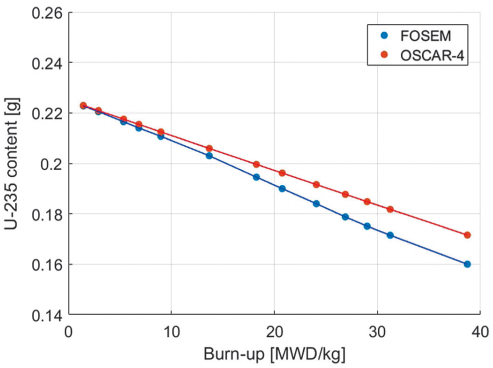


FIGURE 10. MNR-333 U235 content vs. burnup.

The EOC core inventory estimate from the FOSEM approximation shows a noticeably lower U-235 inventory than that from the OSCAR-4 model. The data show an initial burnin period as both calculations start from the same fuel composition estimates. To further examine these differences a detailed tracking of SFA (MNR-333) was selected to present its U-235 depletion over the period of this calculation. The MNR-333 SFA was introduced to the core in the fresh (unirradiated) state in Core Cycle 54A, the first cycle of this calculation. Figure 10 illustrates the U-235 against burnup.

The OSCAR-4 fuel depletion calculation shows a divergence from the FOSEM estimate during the fuel irradiation calculation. A notable discrepancy can already be seen after a number of cycles. This is due to the assumption that all the energy comes from U-235 fission in the FOSEM approximation. This

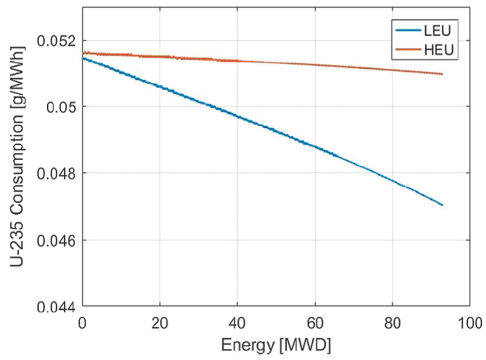


FIGURE 11. HEU and LEU fuel consumption using HEADE cell calculation.

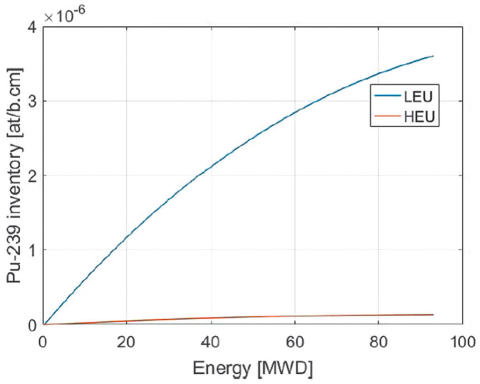


FIGURE 12. HEU and LEU Pu-239 buildup using HEADE cell calculation.

assumption is more accurate for HEU case. Thus, using the same value of $C = 0.05417$ g/MWh for HEU to LEU is not straightforward.

Figures 11 and 12 show the fuel consumption (in g/MWh) variation throughout the fuel irradiation and the Pu-239 buildup, respectively. In LEU fuel, unlike HEU fuel, the U-238 concentration is considerable. This results in a buildup of the Pu-239 and a subsequent contribution to the total fission rate and energy release from Pu-239 fission. As a result, for the same energy generation the U-235 consumption is significantly reduced compared with the estimates from the FOSEM. To further illustrate this effect, Figure 13 shows the U-235 consumption in g/MWh with burnup.

CNL NUCLEAR REVIEW
VOL 9, NUMBER 1, DECEMBER 2020



CNL Nuclear Review Downloaded from pubs.cnl.ca by 76.64.227.45 on 02/05/21
For personal use only.

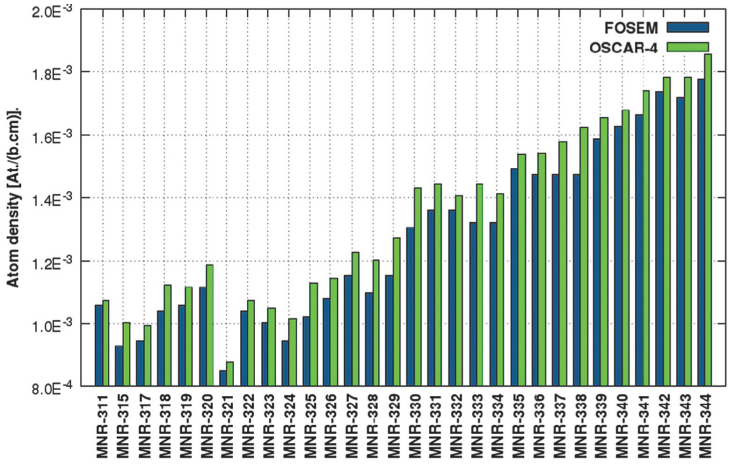


FIGURE 13. U-235 inventory using OSCAR-4 and first-order approximation method.

TABLE 5. Atom density differences.

| Parameter | FOSEM (at/b.cm) | OSCAR-4 (at/b.cm) | Difference (%) |
|---|---|---|---|
| MNR-329 | 1.153E-3 | 1.271E-3 | 10.20 |
| SFAs total average | 1.260E-3 | 1.332E-3 | 5.70 |

At 90 MWD (typical SFA exit burnup in MNR), the consumption of U-235 in LEU is only about half of that in HEU. This calculation was done with HEADE for both HEU and LEU.

The buildup of Pu-239 shows the opposite effect, as shown in Figure 14; compared with LEU, there is almost no buildup of Pu-239 in HEU.

The fuel inventory estimates from FOSEM approximation are lower than the OSCAR-4 code. Table 5 summarizes the maximum difference, which is found in MNR-329, among all SFAs, and the average difference of all SFAs.

The maximum difference that was found in MNR-329 SFA with 10.2% does not solely represent the atom density difference. In fact, this difference includes other uncertainties in both methods as indicated in the methodology, which are out of scope for this study. To explain this difference, MNR-329 was primarily located at high power level between 2 control rods in 5E position (see section 3) until March 2009. Then, MNR-329 was moved to the peripheral region in 2F for the next 2 months. In May 2009, it was moved again to 1C for 5 months before it was lastly moved, in October 2009, to 6D for the rest of the period.

To present the maximum difference that was found in MNR-329 due to the atom density concentration, Equations (3) and (4) are used.

$$\Delta_{\text{U-235}} = \frac{C - \overline{C}}{C} \times 100 \tag{3}$$

where $C$ is the fuel consumption value of the FOSEM approximation and $\overline{C}$ is the average value of the fuel consumption from Figure 11:

$$\overline{C} = \frac{1}{E}\int_0^E C(E)dE \tag{4}$$

where $E$ is the energy release, and $C(E)$ is the consumption value at a specific energy $E$. The difference for MNR-329, at 63.65 MWD in January 2010, was found to be 7.58%. In other words, 2.62% of the difference is due to the other factors that are not related to the fuel inventory such as power distribution.

## 7. Conclusion

Core-follow calculations for MNR were performed using the OSCAR-4 code system. Results of the operational period of 3 years, comprised of 31 cycles, were used to predict the multiplication factor of each start-up critical condition, for a total of 738 days. In addition, a simple FOSEM of U-235

estimates was utilized to compare with OSCAR-4 simulation model to investigate fuel consumption.

It was found that the $k_{\text{eff}}$ is improving, i.e., getting closer to unity, as core inventory is being tracked. This was due to the consumption rate of the U-235 when LEU fuel is being used. Additionally, noticeable peaks were seen when criticality calculation occurred on Mondays. This perhaps due to the CRs worth differences between the actual value to the model value. Further investigation is left as future work.

The OSCAR-4 model U-235 depletion estimates showed notable differences compared with those using the FOSEM, which was found to significantly overestimate U-235 consumption. This overestimation of the fuel depletion in the FOSEM was found due to the lack of consideration of Pu-239 to the energy production. Differences in U-235 inventory in the individual SFAs increase with fuel exposure, to an average of 5.7% and to a maximum of 10.2% for a single SFA.

The findings suggest that OSCAR-4 represents an improvement over the FOSEM for core follow calculations. The OSCAR-4 code for MNR core-follow purposes can better estimate the fuel inventory since all fissile isotopes that contribute to the energy production are considered.

## ACKNOWLEDGEMENTS

The authors would like to thank Chris Heysel, Director of the McMaster Nuclear Reactor, for the support of the MNR Reactor Group in terms of the provision of data, consultation, and guidance, and Drs. Rian Prinsloo and Francois van Heerden from Necsa for their support in the use of the OSCAR-4 code and for providing helpful suggestions.

## REFERENCES

[1] S. Day, 2011, "McMaster Nuclear Reactor: Reactor Specification," Technical Report, submitted to IAEA CRP: Innovative Methods for Research Reactors, Vienna, Austria.

[2] E. Muller, G. Ball, W. Joubert, H. Schutte, C. Stocker, and F. Reitsma, 1994, "Development of a Core Follow Calculational System for Research Reactors," Proceedings of the 9th Pacific Basin Nuclear Conference: Nuclear Energy, Science and Technology Pacific Partnership, Institution of Engineers, Australia, Barton, A.C.T., pp. 1047–1051.

[3] G. Standera, R.H. Prinslooa, E. Müller, and D.I. Tomašević, 2008, "Oscar-4 Code System Application to the Safari-1 Reactor," International Conference on Reactor Physics, Nuclear Power: A Sustainable Resource, Casino-Kursaal Conference Center, Interlaken, Switzerland, 14–19 September 2008.

[4] S. Day, 2012, "McMaster Nuclear Reactor: Benchmark Specification," Technical Report, submitted to IAEA CRP: Innovative Methods for Research Reactors, Vienna, Austria.

[5] Innovative Methods in Research Reactor Analysis: Benchmark against Experimental Data on Neutronics and Thermalhydraulic Computational Methods and Tools for Operation and Safety Analysis of Research Reactors (2008–2013).

[6] M. Mashau, S. Groenewald, and F. van Heerden, 2017, "Application of the Next Generation of the Oscar Code System to the ETRR-2 Multi-Cycle Depletion Benchmark," 18th IGORR Conference, Sydney, Australia, 3–7 December 2017.

CNL Nuclear Review Downloaded from pubs.cnl.ca by 76.64.227.45 on 02/05/21
For personal use only.

# Chapter 4

# Simulation Approach And Code Functionality Assessment Using Deterministic And Monte Carlo Codes System For U-235 Core-Follow Depletion Calculation

Citation:

M. Alqahtani, A. Buijs, and S. Day, 2020, "Simulation Approach And Code Functionality Assessment Using Deterministic And Monte Carlo Codes System For U-235 Core-Follow Depletion Calculation", Progress in Nuclear Energy, doi: 10.12943/CNR.2019.00011

The previous chapter has demonstrated the precision of the OSCAR-4 code system utilization for the MNR core inventory. However, for the purpose of this thesis, the Monte Carlo particle transport code has to be employed for the photon tracking calculations. Since the calculation of the MNR core history using Monte Carlo codes will require considerable computer resources and would be rather cumbersome to follow, this paper determines the feasibility of using the Serpent-2 code system for a long-period of core burnup history. This paper proves that despite control rods movement having been approximated, no significant change was encountered.

Progress in Nuclear Energy 129 (2020) 103501

Contents lists available at ScienceDirect

Progress in Nuclear Energy

journal homepage: http://www.elsevier.com/locate/pnucene

# Simulation approach and code functionality assessment using deterministic and Monte Carlo codes system for U-235 core-follow depletion calculation

Mohammed Alqahtani [a,b,*], Adriaan Buijs [a], S.E. Day [a]

[a] McMaster University, Department of Engineering Physics, Hamilton, Ontario, Canada
[b] KACST, Nuclear Science Research Institute (NSRI), Riyadh, Saudi Arabia

ARTICLE INFO

*Keywords:*
Fuel inventory calculation
Monte Carlo simulation code
Nodal diffusion code

ABSTRACT

Improving the performance of reactor simulation codes and adequately predicting the fuel composition are crucial to increase the accuracy of simulations and the quality of the analysis. McMaster Nuclear Reactor (MNR) follows a strict daily operational and shutdown schedule, except for Sundays. This results in a buildup of neutron poison during the reactor shutdown and hence the Control Rods (CRs) are extracted in the time of the reactor startup. Therefore, tracking MNR core composition using faithful Control Rods (CRs) positions data to estimate the axial fuel inventory profile is not yet established. In this study, nodal diffusion (OSCAR-4) and Monte Carlo (Serpent-2) simulations codes were employed. This study investigates: (1) code-to-code differences in the multiplication factor ($k_{eff}$) and in the axial fuel inventory considering the same burnup step sizes and total energy release with all CRs out; (2) for long cycles of core calculation, Monte Carlo stochastic code is computationally expensive, therefore an adequate temporal discretization steps are studied and identified. The $k_{eff}$ values for the fresh reactor when all rods are out is: 1.1339 and 1.1283, and the results at the end of the burnup calculation is: 1.0101 and 1.0049, for Serpent-2 and OSCAR-4, respectively. In addition, the findings showed that averaging the CRs travel distance, for calculation the fuel inventory, can provide results similar to those with most tracked CRs motion.

## 1. Introduction

The availability of operational data history of U-235 is essential to enhance safety, economics and performance of any nuclear reactor (Determination of research, 1992). McMaster Nuclear Reactor (MNR) uses flux-wire measurements to estimate the U-235 fuel inventory (Alqahtani et al., 2018). Two recent studies at McMaster Nuclear Reactor (MNR) have investigated and validated the U-235 using two simulations codes, OSCAR-4 and Serpent-2, with the operational data history (Alqahtani et al., 2019), and (Alqahtani et al., 2020). However, a challenging problem which arises in this domain is considering each standard fuel assembly (SFA) and control fuel assembly (CFA) as one-node lumped fuel composition. This has been widely adopted at MNR operational estimates since decades (Alqahtani et al., 2019).

The operational schedule of MNR is a daily start-up and shutdown during the week except Sunday. This causes neutron poison, mainly xenon, build-up during the night which results in a need to extract the CRs for the next start-up to reach criticality. Hence, this motion of the CRs will alter the axial power distributions and as a result fuel inventory. To study the impact of the axial fuel inventory in MNR by the CRs motion, different temporal discretization step sizes are investigated using the two simulation codes: Serpent-2 and OSCAR-4.

However, using Monte Carlo simulation code (Serpent-2) to track fuel inventory with a short time-step size for long period i.e. a daily step size for a three-month cycle is computationally expensive. Since the time-consuming transport calculation has to be repeated for each time step, finding an adequate step length is investigated here using Serpent-2 code system.

Previous studies have shown the effect of using realistic axially heterogeneous fuel compositions, several axial layers per fuel assembly, instead of uniform ones for Material Testing Reactor (MTR) type. In reference (Arthur and MalouchCheikhDiop, 2016), the axial fuel

*Abbreviations:* SFA, Standard Fuel Assembly; CFA, Control Fuel Assembly; CR, Control Rod; EOL, End Of Life; FA, Fuel Assembly; HEADE, HEterogeneous Assembly DEpletion; LEU, Low-Enriched Uranium; MGRAC, Multi-Group Reactor Analysis Code; MNR, McMaster Nuclear Reactor; MTR, materials test reactor; CIF, Central Irradiation Facility.

* Corresponding author.
*E-mail addresses:* alqahm1@mcmaster.ca, malqahtani@kacst.edu.sa (M. Alqahtani).

https://doi.org/10.1016/j.pnucene.2020.103501
Received 22 March 2020; Received in revised form 17 July 2020; Accepted 4 September 2020
0149-1970/© 2020 Elsevier Ltd. All rights reserved.

compositions profile on fluxes showed no differences when considering more than seven axial layers. Similarly, in reference (Vutheam Dos et al., 2020), using seven axial layers (meshes) and one radial mesh for each fuel assembly (FA) is enough for precise depletion simulation of the MTR.

No study to date has examined the impact of the control rods (CRs) motion on the axial fuel assemblies composition (U-235). One of the simplest ways of tackling this problem is by dividing the axial fuel assemblies (FAs) into several layers and then analyzing the axial core fuel when CRs position are varying. In this paper we present two types of simulations to study the differences when using the same time-step sizes and total exposure, with all rods out of the core; and to find the adequate time-step size, when the CRs inserted, for core follow calculation. The investigation is performed on the axial adjacent fuel to the CRs, which are the CFAs.

## 2. Methodology

### 2.1. Codes modelling

Two simulation codes were utilized in this paper, OSCAR-4 and Serpent-2. OSCAR4 performs detailed 2D transport calculations on the scale of a single assembly, and to use this solution to produce averaged, or homogenized, parameters for the assembly. Calculation of full 3D core model using nodal diffusion method is used (Müller et al., 1994). Serpent-2 is a continuous-energy reactor physics code that solves the Boltzman equation by using the Monte Carlo method. Once neutron interaction occurs, or non-stable isotopes exist, Bateman equations are solved to provide changes to the material composition (Leppänen and Thesis, 2007).

Predictor-corrector method for calculating the fuel burn-up was used in the both codes. This method is based on two-step calculations: (i) beginning-of-step that uses constant extrapolation or explicit Euler method, and (ii) at the end-of-step where material is depleted over the interval, and new flux and cross sections are calculated. The average of the two fluxes is then used to deplete the fuel in predictor-corrector method. The method that was used in Serpent-2 for solving the Bateman equations describing the changes in the isotopic compositions caused by neutron-induced reactions and radioactive decay is the Chebyshev Rational Approximation Method (CRAM) (Pusa and Leppanen, 2010).

Cross section data are necessary for criticality and fuel depletion calculation. In OSCAR-4, six-neutron-energy group structures were used (HEADE, which performs 2D cell calculation utilizing collision probability method and produces homogenized and condensed cross sections data). The nuclear data used here is WIMS-E 172-group cross section library based on JEF-2.2 (Alqahtani et al., 2020). In Serpent-2, ENDF/BVII.0 cross sections were used in ACE format (Chadwick et al., 2006).

### 2.2. Model description

MNR is an open-pool type Materials Test Reactor (MTR). It consists of 9 by 6 grid, with assemblies that contains Standard Fuel Assemblies (SFAs), Control Fuel Assemblies (CFAs) with low enriched uranium (LEU), graphite reflectors, a beryllium reflector and a central irradiation facility (CIF). The fuel assemblies, in both codes, were divided into seven axial layers to capture the axial distributions of the neutron flux and fuel depletion of each FA and CFA.

In the 3D full core simulation, Serpent-2 captures the geometrical details of the assemblies as well as the out-core details such as beam tubes and additional reflectors. In OSCAR-4, two stages of calculations were performed. First, a 2D cell calculation capturing the geometrical detail and the collapsing of neutron energy group cross section. Then, 3D reactor core calculation using nodal diffusion methods with homogenized cross sections, is constructed using the various cross section sets produced from the 2D calculation. Figs. 1 and 2 present the core configuration used in this work of MNR and the core simulation model using Serpent-2, respectively.

The MNR core contains six CFAs that house the CRs. These CFAs have the same outer dimensions as the standard fuel assemblies. The MNR CFAs contain nine plates, all of which are fuelled (i.e., no dummy plates) and a central aluminum guide to house the CRs. As can be seen from Figs. 1 and 2 that the out-core of the MNR is flanked by a large lead block from the West peripheral and six radial beam-tubes in the North and East peripheral sides. The general core specifications and fuel materials of MNR are given in Table 1 (Day, 2011).

### 2.3. Simulation approach

The depletion calculation was carried out in both codes with the same initial fresh fuel composition. The parameters that are important in core calculation such as $k_{\text{eff}}$, MNR core power levels (prior and after irradiation), and the fuel inventory of U-235 are present in this analysis. The latter will investigate the CRs effect on the axial CFAs fuel inventory. This will include both; finding the adequate number of steps, and OSCAR-4 to Serpent-2 U-235 inventory differences.

In the first part of the study, OSCAR-4 and Serpent-2 simulated the MNR with 48 time-step of five days with all CRs extracted. The total time of irradiation was 240 days and the reactor power used was 5 $MW_{th}$. The total energy released of 1200 MWD was selected based upon the first three CFAs End Of Life (EOL), and the number of steps was selected based on the observable variation on the axial fuel inventory changing.

Second, the calculational time in Serpent-2 code is a challenge therefore, an adequate number of steps has to be identified considering both: (i) possible lowest calculational time, and (ii) insignificant differences in the fuel inventory. This can be done by using different time-step investigation conserving the total energy release.

In this work, we consider the full range of the CRs motion to study the maximum differences that could happen when approximations on the CRs motion are considered. The operational conditions in MNR for the shim CRs extractions should always be minimally extracted 60% (36 cm) to have a sufficient negative reactivity for the shutdown safety purposes. In addition, the exit fuel depletion is nominally 35% U-235 depletion for the CFA (Day et al. Garland).

Several time-step sizes for tracking the CRs were implemented. The core height is 60 cm. The minimum CRs extraction started at 60% (36 cm) and then a step (S) size is added for each additional time step. For instance, the most tracked CRs is 48 time-step (48 S) that means it will need a total of 48 S to reach fully extracted CRs at 60 cm. This will provide the maximum possibility of the CRs variation during MNR operation. Averaging the CRs motion will also be investigated, as per equation (1). Table 2 shows the data used when approximation is considered for handling the averaging CRs travelling in each case. This data will be used to find the adequate number of steps.

$$CR_M = CR_{\text{min.}} + \frac{\sum_{i=1}^{8} CR_i\,(\%) \times t_i}{\sum t_i} \tag{1}$$

where; $CR_M$ is the average CRs used in the model at specific time-step, $CR_{min.}$ is the minimum CRs extraction as per MNR operational condition which is 60%, $CR_i$ is the mid-point of the CRs travelling in each step i for s number of steps, and $t_i$ is the time step length in Day.

The reactor power remained constant during the calculation. In case of power variations during the calculation, the reactor power must be considered in the previous equation with its time duration.

For Serpent-2, 500 cycles with 80,000 neutron histories each were run, with 50 cycles skipped as inactive; therefore, a total of 40,000,000 neutron histories were simulated. The statistical uncertainty in the $k_{\text{eff}}$ was 0.16 mk and a maximum of statistical error in local assembly power is 0.14%. The Shannon entropy converged at the 30th cycle owing to the approximation in the axial seven layers with lumped 16 fuel plates in

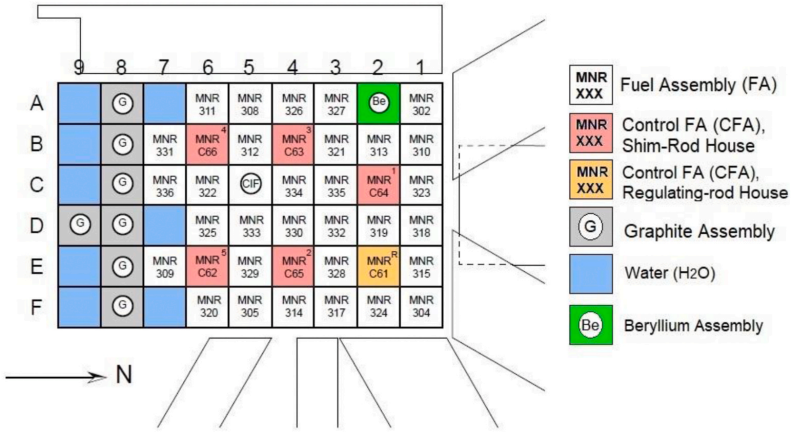


**Fig. 1.** MNR core configuration.

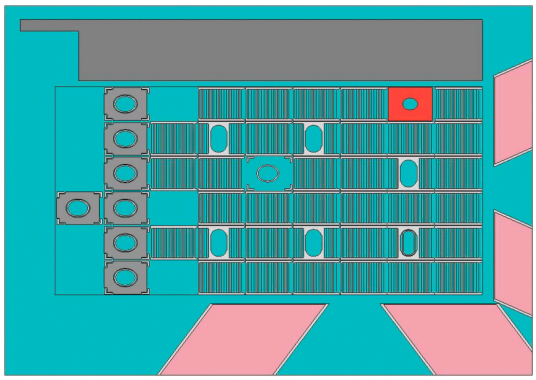

**Fig. 2.** Serpent-2 model of MNR core.

each layer. Therefore, 50 cycles were skipped for fission source convergence.

## 3. Results and analysis

One of the major objectives in this work is to reduce the computational time using Serpent-2 and one solution has suggested is to average the CRs travel. The maximum calculational time in OSCAR-4 was found 2.47 min with 48 time-step size. In Serpent-2, the calculational time is varying significantly in each time-step case. The variation is linear related to the number of time-step used. A total of 20 shared memory multiprocessing (omp) were used in each step in Serpent-2. Table 3 shows the data used when approximation is considered for handling the averaging CRs travelling in each case. This data will be used to find the adequate number of steps.

**Table 1**
MNR specification.

| Parameter | Value and description |
|---|---|
| Core lattice size (x-direction) | 8.1 cm |
| Core lattice size (y-direction) | 7.7 cm |
| Active core height | 60 cm |
| Fuel type | $U_3Si_2$–Al dispersion Al-clad curved plate fuel |
| Enrichment | 19.75 wt% (LEU) |
| Coolant and moderator material | Light water |
| Reflector material | Graphite |
| Fuel meat thickness | 0.051 cm |
| Fuel plate thickness | 0.127 cm |
| Coolant gap size | 0.300 cm |
| Fuel Assembly (FA) atom density | $1.8899 \times 10^{-3}$ at/b.cm |
| Control Fuel Assembly (CFA) atom density | $1.6679 \times 10^{-3}$ at/b.cm |

**Table 2**
Data used in Serpent-2 code.

| No. of Steps | Label | Time-step | CRs Extraction Each Step |
|---|---|---|---|
| (#) | (#S) | (days) | (%) |
| One | 1 S | 240 | 80 |
| Two | 2 S | 120 | 70, 90 |
| Three | 3 S | 80 | 66.67, 80, 93.33 |
| Eight | 8 S | 30 | 62.5, $n_{i-1}$ + 5, ...,97.5 |
| Sixteen | 16 S | 15 | 61.25, $n_{i-1}$ + 2.5, ...,98.75 |
| Twenty four | 24 S | 10 | 60.83, $n_{i-1}$ + 1.67, ...,99.17 |
| Forty eight | 48 S | 5 | 60.42, $n_{i-1}$ + 0.83, ...,99.58 |

### 3.1. All rods out

Fig. 3 shows the multiplication factor ($k_{eff}$) that was tracked during the calculation when both of the models had fully extracted CRs. The burnup calculation was performed here with the same number of steps for both codes, 48 steps with five days per step.

From Fig. 3, the $k_{eff}$ was found at the Beginning of Calculation (BOC) at: 1.1339 and 1.1283, and at the End Of Calculation (EOC): 1.0101 and 1.0049, for Serpent-2 and OSCAR-4, respectively. Considering 48

**Table 3**
Computational time using Serpent-2.

| Label | Time-step | Calculation Time |
|---|---|---|
| (#S) | (days) | (hh:mm) |
| 1 S | 240 | 00:42 |
| 2 S | 120 | 01:26 |
| 3 S | 80 | 02:03 |
| 8 S | 30 | 07:27 |
| 16 S | 15 | 14:12 |
| 24 S | 10 | 22:32 |
| 48 S | 5 | 45:23 |

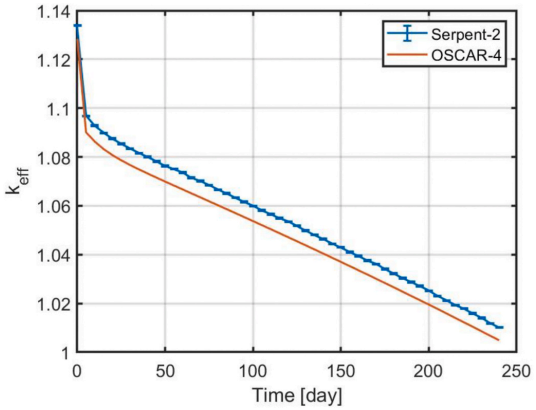


**Fig. 3.** $k_{eff}$ versus the operating time for different simulation codes.

temporal discretization steps, a total of 240 days, was enough to deplete the U-235 to nearly its EOL in three CFAs (MNRC63, MNR-C64, and MNR-C65). Additionally, having the CRs fully extracted for the whole duration of this calculation will provide information on the differences between the two models when considering different calculation methods and different nuclear data libraries. Prior to analyzing the CFAs atom densities resulting from the burn-up calculation, the radial power distribution across the MNR core can be used to predict the depletion behaviour across the core from the two codes. Figs. 4 and 5 show the assembly power fraction distribution in percentage (%) of the total power of 5 $MW_{th}$ for Serpent-2 (L) and OSCAR-4 (R) when both models started with the same initial atom density (fresh fuel) and fully extracted CRs.

Power distributions vary as fuel burn-up occurs due to the accumulation of fission products and depletion of the fissile isotopes. During fuel depletion, fission reaction rate or power distributions in the high burn-up assemblies decrease as shown in the previous figures. Fig. 6 shows the CFAs powers at both BOC and EOC.

Fig. 7 shows the axial U-235 inventory in the CFAs following 48 time-step, with total MNR core energy released of 1200 MWD, with all rods out of the core. Each node represents an 8.57 cm length with a total length of 60 cm. The CFA ID can be identified from Fig. 1.

The uppermost axial node of each CFA has slightly higher concentration than the lowest nodes due to the CRs existence above the reactor core. The overall axial profile for each CFA in OSCAR-4 is more symmetrical than those in Serpent-2. The maximum difference can be seen in the MNR-C65 with 4.3% deviation at 21 cm elevation and 2.2% overall average difference between the two codes along the axial CFA. Even though the methods and the nuclear data libraries used in both codes are different, this deviation is mainly due to the local power differences between the two codes, see Fig. 5.

### 3.2. Effect of the CRs averaging travelling on the axial fuel inventory

Prior to comparing axial fuel inventory (U-235) using the Serpent-2 and OSCAR-4, a code self-investigation was implemented to simulate the MNR with several temporal discretization steps, see Table 3. For each step, the average CRs travel equation (1) was used. This was important to find an adequate number of steps that can be used when core-follow calculation is utilized. The adequate number of steps consider both the calculational time and the non-significant change in the axial atom density profile ( < 1%). The following Figs. 8 and 9 show the axial U-235 fuel inventory in the most depleted three CFAs.

For those with more than one time-step, the number of steps to deplete the fuel inventory does not have a significant impact on the axial fuel distribution profile. In both codes, a minimum of two time-step (2 S) demonstrates an axial U-235 profile similar to those with higher time-step. In other words, varying the CRs with a maximum of 20% (12 cm) is still providing results similar to those with 0.83% (0.5 cm) in each step when CRs average travel is considered.

From the short review above, the results confirm that the impact of averaging the CRs motion using equation (1) on the axial U-235 fuel depletion is not significant. Therefore, considering the CRs average travel can still provide information similar to those with the detailed tracking CRs positions.

### 3.3. U-235 inventory comparisons between OSCAR-4 and Serpent-2

It was previously demonstrated that no considerable discrepancies can be found when more than 1 S is considered. The following Fig. 10 shows the fuel inventory with 2 S using Serpent-2 and OSCAR-4 codes system.

Similar axial fuel inventory profile has been observed between the codes. The maximum differences between the two codes were found at the uppermost axial nodes in the three CFAs (MNR-C63, MNR-C64 and MNR-C65) with 5.5%, 5.5% and 5%; and 2.7%, 2.8% and 3.6% average difference over the axial CFA. One of the major factors that contribute to this discrepancy is the CRs worth. Insertion of different CRs worth can cause the power distribution to peak toward the bottom and/or absorb more in the local insertion. Table 4 shows the CRs worth using the two codes models when the core is loaded with fresh fuel.

Each CR has different negative reactivity worth based on the local neutron flux. The collective CRs worth is different than the sum of each individual CR. Higher negative reactivity worth results in higher neutron absorption, and hence lower local power. The maximum three CRs worth are found in the same region as the maximum CFAs inventory differences located. Another important factor to be considered in analyzing the axial fuel inventory depletion is the thermal neutron flux. Fig. 11 shows the axial CFA thermal neutron flux used in Fig. 10

| | 7 | 6 | 5 | 4 | 3 | 2 | 1 |
|---|---|---|---|---|---|---|---|
| A | | 2.05 | 2.50 | 3.03 | 3.09 | | 1.82 |
| B | 1.85 | **1.66** | 3.46 | **2.51** | 3.73 | 3.51 | 2.19 |
| C | | 3.15 | | 4.56 | 4.17 | **2.41** | 2.44 |
| D | 2.03 | 2.84 | 3.92 | 4.22 | 4.09 | 3.67 | 2.35 |
| E | 1.77 | **1.65** | 3.04 | **2.34** | 3.39 | **1.93** | 1.92 |
| F | | 1.93 | 2.24 | 2.58 | 2.43 | 2.11 | 1.41 |

| | 7 | 6 | 5 | 4 | 3 | 2 | 1 |
|---|---|---|---|---|---|---|---|
| A | | 2.13 | 2.58 | 3.03 | 3.24 | | 1.94 |
| B | 2 | **1.62** | 3.48 | **2.5** | 3.85 | 3.51 | 2.33 |
| C | | 3.2 | | 4.48 | 4.16 | **2.34** | 2.56 |
| D | 2.19 | 2.8 | 3.85 | 4.08 | 3.99 | 3.42 | 2.38 |
| E | 1.92 | **1.63** | 3.06 | **2.25** | 3.29 | **1.82** | 1.93 |
| F | | 2.03 | 2.24 | 2.47 | 2.38 | 1.96 | 1.36 |

**Fig. 4.** Assembly power fraction (%) map for the fresh core, Serpent-2 (L) and OSCAR-4 (R).

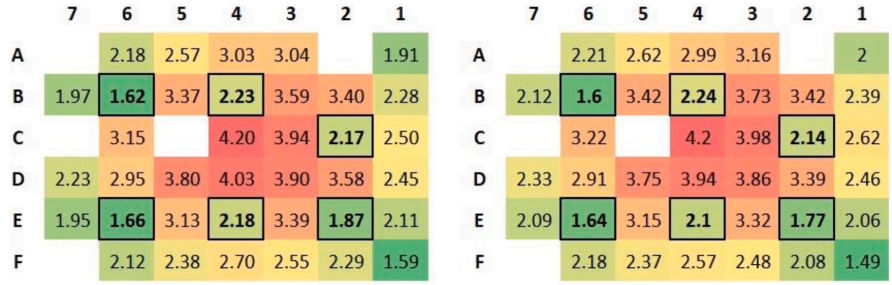


**Fig. 5.** Assembly power fraction (%) map for the depleted core, Serpent-2 (L) and OSCAR-4 (R).

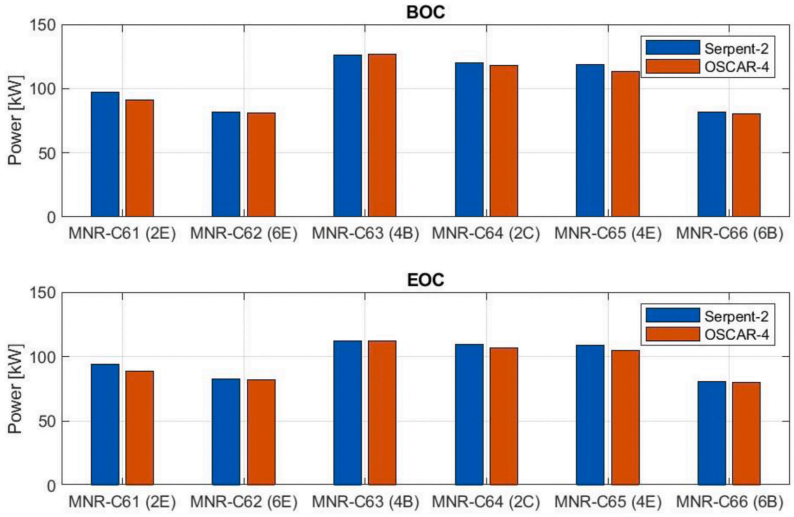


**Fig. 6.** CFAs powers at BOC and EOC.

calculation in the three CFAs (MNR-C63, MNR-C64, and MNR-C65).

The CRs effect plays a major role in the thermal neutron flux of the upper-half CFAs.

However, no significant changes have been observed in the lower-half CFAs when the CRs have been withdrawn. The major cause to the differences between the two codes is the radial/assembly powers, see Figs. 4 and 5.

This work is limited as changes in fission product concentrations (e.g. xenon, samarium) during the reactor shutdown and self shielding were not studied. Nevertheless, at this level of understanding we believe that fission products will not have a significant impact on the U-235 profile as it was shown in Figs. 4 and 5 when power distribution between BOL and EOL did not vary significantly.

## 4. Conclusion

MNR Core-follow calculation analysis for 240 days was performed using the OSCAR4 and Serpent-2 code systems. Various modelling approaches were investigated to study the effect of the CRs average travelling on the axial CFAs fuel inventory. Although approximations were made in the CRs motion, no loss of accuracy was found in terms of the fuel concentration is encountered when considering higher than one-

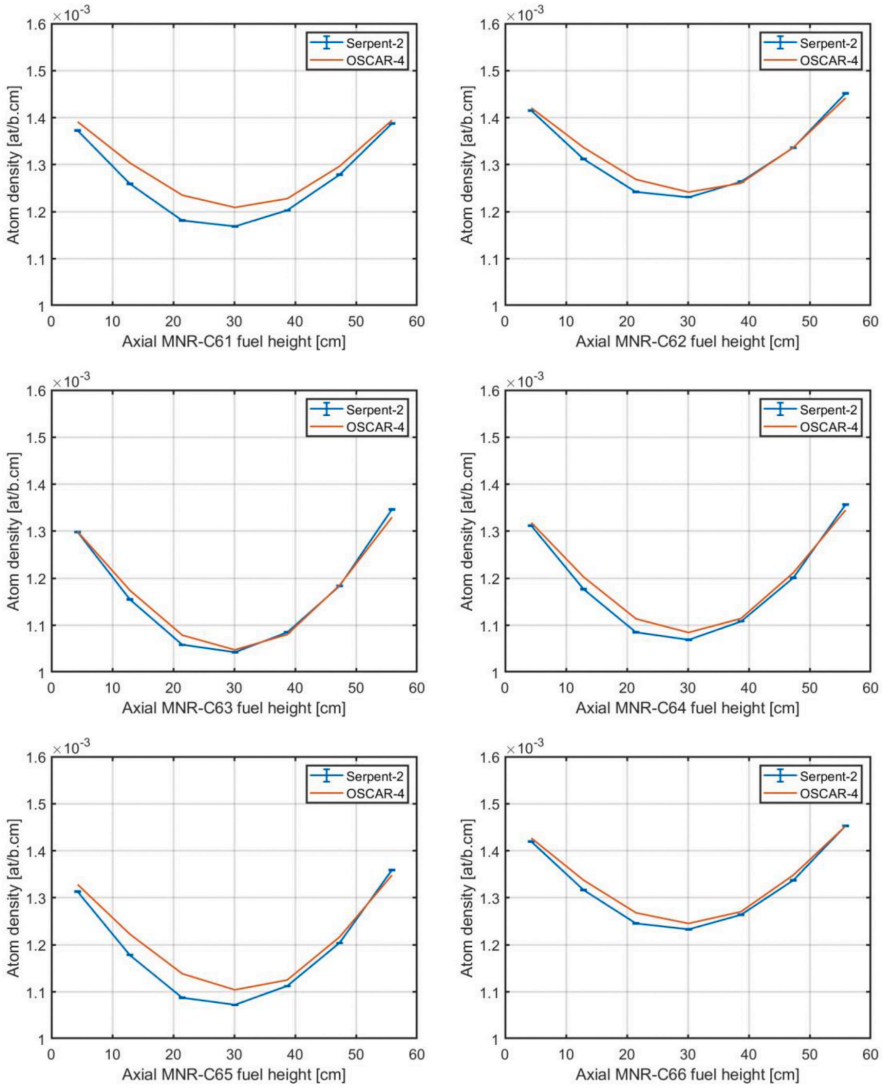


**Fig. 7.** Axial CFAs U-235 atom densities.

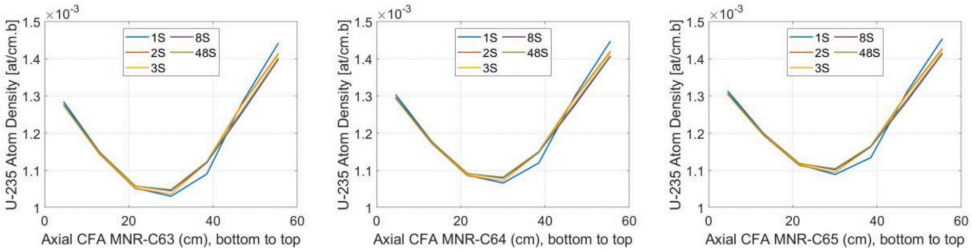


**Fig. 8.** OSCAR-4 U-235 fuel concentration for different time-step.

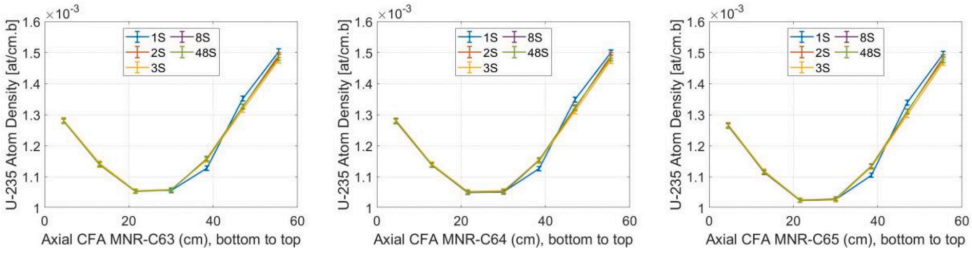


**Fig. 9.** Serpent-2 U-235 fuel concentration for different time-step.

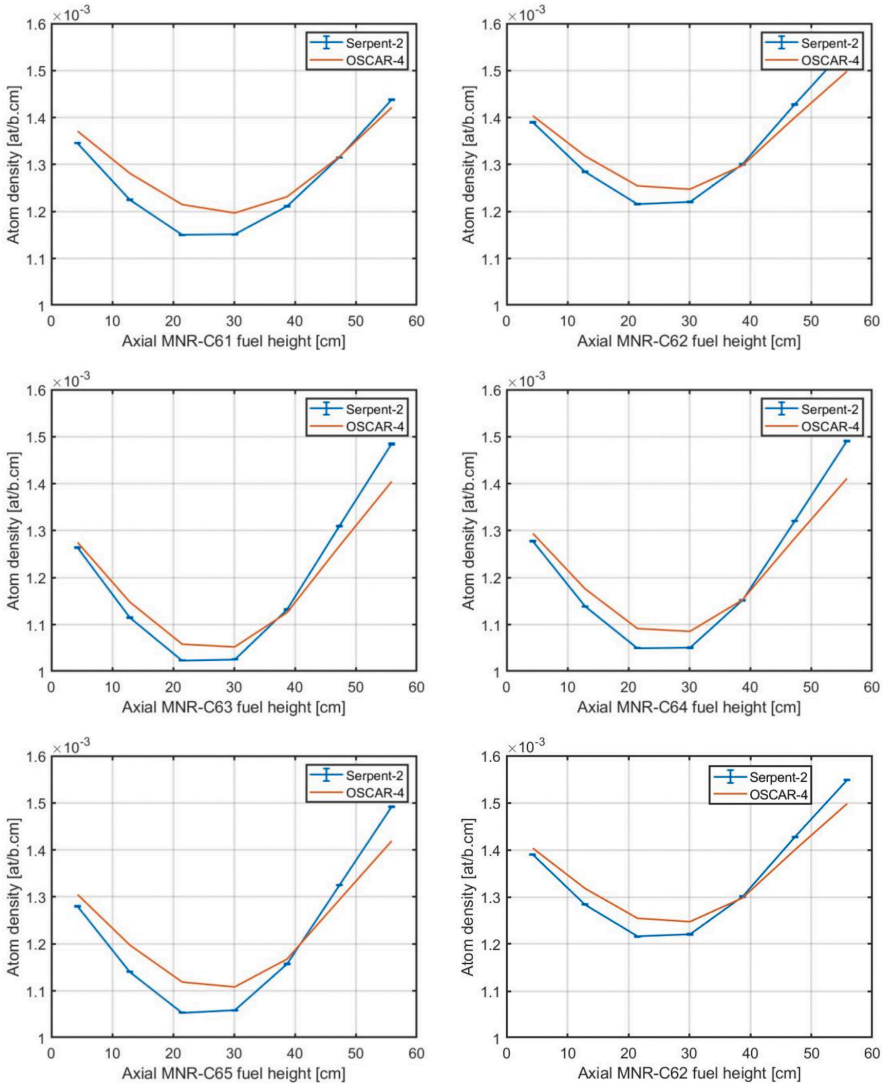


**Fig. 10.** Axial CFAs U-235 atom densities with two-step (2 S) size.

**Table 4**
CRs worth in Serpent-2 and OSCAR-4.

| CRs Label | OSCAR-4 (mk) | Serpent-2 (mk) | Differences (mk) |
|---|---|---|---|
| CR-C61 | 3.28 | 3.98 ± 0.19 | 0.71 ± 0.19 |
| CR-C62 | 8.90 | 11.62 ± 0.21 | 2.79 ± 0.21 |
| CR-C63 | 21.43 | 27.67 ± 0.18 | 6.52 ± 0.18 |
| CR-C64 | 23.94 | 30.52 ± 0.21 | 6.80 ± 0.21 |
| CR-C65 | 19.03 | 26.17 ± 0.20 | 7.25 ± 0.20 |
| CR-C66 | 7.63 | 10.57 ± 0.19 | 3.04 ± 0.19 |
| **Collective CRs worth** | 70.72 | 90.12 ± 0.20 | 19.40 ± 0.20 |

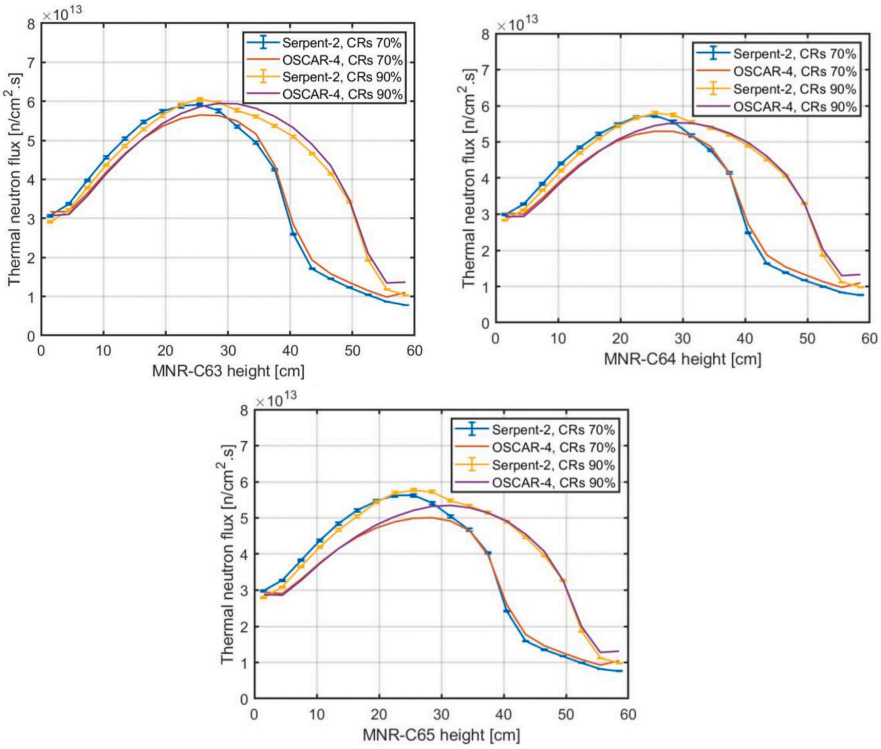


**Fig. 11.** Serpent-2 U-235 fuel concentration for different time-step.

time step. In this investigation, it was found that the highest difference of the fuel inventory, when fuel is fresh and all CRs are out, was found in MNR-C65 with 4.3% in the lower-middle node and 2.2% for the average axial U-235. Whereas, when averaging the CRs travelling, the fuel inventory profile between codes was found similar in the three CFAs. The highest node difference between the two simulations were found in the upper most node of MNRC63 and MNR-C64 with 5.5%, and for assembly average difference was in the MNR-C65 with 3.6%.

Averaging the CRs movement using Serpent-2 code for MNR core-follow calculation should be able to estimate the fuel inventory in a very good agreement as if a detailed CRs tracking is considered.

## Author contribution

Mohammed Alqahtani: Conceptualization, Methodology, Validation, Formal Analysis, Investigation, Writing - Review & Editing, Visualization. Adriaan Buijs: Supervision. Simon Day: Supervision.

## Declaration of competing interest

The authors declare that they have no known competing financial interests or personal relationships that could have appeared to influence the work reported in this paper.

## Acknowledgments

The authors would like to thank Chris Heysel, Director of the McMaster Nuclear Reactor, for his support, and Dr. Rian Prinsloo and Dr. Francois van Heerden from Necsa. The first author wish to express their thanks to Dr. Dave Novog, McMaster University, for his advice in developing this research, and to Elizabeth MacConnachie for her assistance in part of this work.

## Appendix A. Supplementary data

Supplementary data to this article can be found online at https://doi.org/10.1016/j.pnucene.2020.103501.

## References

Alqahtani, M., Day, S., Buijs, A., 2018. Flux-wire measurements and fuel burn-up estimate comparisons with simulations for core-follow calculations at MNR reactor. In: CNS 38th Annual Conference and 42nd Annual CNS/CNA Student Conference. Canadian Nuclear Society (CNS).

Alqahtani, M., Day, S., Buijs, A., 2019. OSCAR-4 code system comparison and analysis with a first-order semi-empirical method for core follow depletion calculation in McMaster nuclear reactor (MNR). CNL Nuclear Review.

Alqahtani, M., Buijs, A., Day, S., 2020. Serpent-2 and OSCAR-4 computational tools compared against McMaster nuclear reactor improved operational data history for U-235 fuel inventory tracking, local power tracking and validation of multiplication factor. Annals of Nuclear Energy.

Arthur, Péron, Malouch, Fadhel, Cheikh Diop, 2016. Improvement of nuclear heating evaluation inside the core of the osiris material testing reactor. EPJ Web Conf. 106, 05006 https://doi.org/10.1051/epjconf/201610605006, 01.

Chadwick, M.B., Oblozinsky, P., Herman, Michal, Greene, N.M., McKnight, R.D., Smith, D.L., Young, P.G., MacFarlane, R.E., Hale, G.M., Frankle, S.C., Kahler, A.C., Kawano, T., Robert Little, D.G., Madland, P., Moller, R.D., Mosteller, Philip Page, Talou, Patrick, Trellue, H., van der Marck, Steven, 2006. Endf/b-vii.0: next generation evaluated nuclear data library for nuclear science and technology. Nucl. Data Sheets 107 (12), 2931–3060. https://doi.org/10.1016/j.nds.2006.11.001.

Day, S.E., 2011. Mcmaster Nuclear Reactor Specification. Technical report (IAEA CRP: Innovative Methods for Research Reactors).

S. E. Day, M. P. Butler, and Wm J. Garland. Calculations in support of the mnr core conversion. In 24th International Meeting on Reduced Enrichment for Research and Test Reactors.

Technical Report IAEA-TECDOC- 633. Determination of research reactor fuel burnup, 1992. IAEA.

Leppänen, J., 2007. Development of a New Monte Carlo Reactor Physics Code. D.Sc Thesis. Helsinki University of Technology.

Müller, E.Z., Ball, G., Joubert, W.R., Schutte, H.C., Stocker, C.C., Reitsma, F., 1994. Development of a core follow calculational system for research reactors. In: 9th Pacific Basin Nuclear Conference: Nuclear Energy, Science and Technology Pacific Partnership; Proceedings of the. Institution of Engineers, Australia page 1047.

Pusa, M., Leppanen, J., 2010. Computing the matrix exponential in burnup calculations. Nucl. Sci. Eng.

Vutheam Dos, Lee, Hyunsuk, Jo, Yunki, Lemaire, Matthieu, Kim, Wonkyeong, Choi, Sooyoung, Zhang, Peng, Lee, Deokjung, 2020. Overcoming the Challenges of Monte Carlo Depletion: Application to a Material-Testing Reactor with the Mcs Code. Nuclear Engineering and Technology. https://doi.org/10.1016/j.net.2020.02.003. ISSN 1738-5733. http://www.sciencedirect.com/science/article/pii/S1738573319304681.

# Chapter 5

# Serpent-2 and OSCAR-4 Computational Tools Compared against McMaster Nuclear Reactor Improved Operational Data History for U-235 Fuel Inventory Tracking, Local Power Tracking and Validation of Multiplication Factor

Citation:

M. Alqahtani, A. Buijs, and S. Days, 2020, "Serpent-2 and OSCAR-4

Computational Tools Compared against McMaster Nuclear Reactor Improved Operational Data History for U-235 Fuel Inventory Tracking, Local Power Tracking and Validation of Multiplication Factor", Annals of Nuclear Energy, doi: 10.1016/j.anucene.2020.107590

This paper introduces a method of the measurement-based MNR core inventory using a fuel correction factor. This factor has been superimposed on the MNR fuel inventory of the operational data documents. The MNR core tracking was implemented using the daily core-follow in OSCAR-4 and rods 3-5 steps in Serpent-2, where each step is less than those used in the previous research. It was shown that the method had improved the results for the whole period of the comparisons. No divergence was seen when a longer period of calculation was carried out, This method proves that superimposing the correction factor for the MNR core measurement-based inventory is crucial for any future code utilized for calculation/analysis purposes.

Annals of Nuclear Energy 145 (2020) 107590

Contents lists available at ScienceDirect

Annals of Nuclear Energy

journal homepage: www.elsevier.com/locate/anucene

# Serpent-2 and OSCAR-4 computational tools compared against McMaster nuclear reactor improved operational data history for U-235 fuel inventory tracking, local power tracking and validation of multiplication factor

M. Alqahtani [a,b,*], A. Buijs [a], S.E. Day [a]

[a] McMaster University, Department of Engineering Physics, Hamilton, Ontario, Canada
[b] Nuclear Science Research Institute (NSRI), KACST, Riyadh, Saudi Arabia

ARTICLE INFO

*Article history:*
Received 23 January 2020
Received in revised form 20 April 2020
Accepted 9 May 2020

*Keywords:*
Fuel inventory tracking
Simulation code validation
Operational data history
Monte Carlo simulation code
Nodal diffusion code
Fuel assembly power

ABSTRACT

The tracking of fuel inventory is important for safety and for knowledge of the flux distribution. In a research reactor, tracking of the reactor core fuel composition using simulation code is crucial for fuel management strategy, such as by optimizing the core pattern for sample irradiation purposes and for providing an economical fuel cycle length. Operational data history for the McMaster Nuclear Reactor (MNR) is a valuable asset for comparing and validating simulation code. A previous study examined U-235 content using the nodal diffusion code Overall System for CAlculation of Reactors (OSCAR-4) against standard MNR operational data and recommended considering the Pu-239 content in the energy production in the standard operational data. In this work, a new method was implemented by introducing a Fuel Inventory Correction (FIC) factor for improving the U-235 operational data records. U-238 and Pu-239 code-to-code tracking comparisons were also employed. The maximum difference between U-235 at end of life (EOL) and the updated operational data history was 2.43% and 6.97% for Serpent 2 and OSCAR-4, respectively. The FA power profile tracking showed a similar response whenever fuel shuffling and/or refueling occurred, with a maximum different of 16% (30 kW) in one cycle. The multiplication factors for the two sets of code differed systematically, averaging 0.9982 and 1.0051 for Serpent 2 and OSCAR-4, respectively.

© 2020 Elsevier Ltd. All rights reserved.

## 1. Introduction

Lack of knowledge of the fuel inventory in a nuclear reactor leads to underestimation of important reactor core parameters such as the effective multiplication factor ($k_{eff}$) and the neutron flux/power distribution when codes simulation are implemented. In a research reactor, the estimation of fuel inventory is highly important for reactor safety and for the optimization of neutron flux at irradiation sites for radioisotope production purposes. A large number of existing researches have studied the reactor core parameters such as fuel burnup, multiplication factor and power distribution (Amin et al., 2017), fuel depletion and buildup of plutonium (Aldawahrah et al., 2018; Khattab and Dawahra, 2011; Dawahra et al., 2015; Dawahra et al., 2015).

Frequent refuelling and/or reshuffling fuels in nuclear research reactors and continuously changing core conditions provide opportunities for developing a reactor-specific database of core-flow parameters and flux distributions that can be used for benchmarking (International Atomic Energy Agency, 2008).

In the McMaster Nuclear Reactor (MNR), U-235 fuel inventory measurement is a routine that occurs during each reload/shuffle cycle. Therefore, to perform core analysis to simulate processes in any given time using computer code, operational data of U-235 is necessitated by those computational tools. Previous studies of fuel inventory using OSCAR-4 code (Standera et al., 2008) with MNR operational data history have focused on U-235 content

*Abbreviations:* CFA, control fuel assembly; CIF, central irradiation facility; CR, control rod; CRAM, Chebyshev rational approximation method; EOL, end of life; FA, fuel assembly; FIC, fuel inventory correction; HEADE, the 2D cell calculation module of OSCAR-4; HEU, high-enriched uranium; LEU, low-enriched uranium; MGRAC, Multi-Group Reactor Analysis Code; MNR, McMaster Nuclear Reactor; MTR, materials test reactor; MWd, megawatt-days; OSCAR-4, nodal diffusion code; Serpent 2, Monte Carlo simulation code; SFA, standard fuel assembly.

* Corresponding author.
*E-mail addresses:* alqahm1@mcmaster.ca, malqahtani@kacst.edu.sa (M. Alqahtani).

https://doi.org/10.1016/j.anucene.2020.107590
0306-4549/© 2020 Elsevier Ltd. All rights reserved.

(Alqahtani et al., 2019). The study covered a calculation period of three years (2007–2010) and showed a diverging difference each cycle between the two calculation methods during core-follow inventory calculation due to the lack of consideration of some fissile isotopes, mainly Pu-239, in the MNR measurement-based estimate method of U-235.

Therefore, tendency to perform best fuel inventory estimates for the purpose of reactor core optimization, safety and simulation codes validation. This paper provides a method for adjusting the measured fuel inventory by introducing a U-235 fuel inventory correction (FIC) factor to be utilized and implemented to the measurement data. In addition, the Monte Carlo simulation code (Serpent 2) reactor physics calculation will be used along with OSCAR-4 nodal diffusion deterministic code to validate and compare some operational parameters such as $k_{\text{eff}}$ and the U-235 fuel inventory measured using the flux-wire method. The code-to-code comparison will additionally present an evaluation of the confidence of the two sets of code by comparing their results against each other.

## 2. Methodology

### 2.1. Modeling codes

In general, there are two kinds of numerical code for conducting reactor core analysis: deterministic and probabilistic (International Atomic Energy Agency, 2019). Deterministic code is used widely for core analysis and requires simplifications and/or approximations in the geometry and the physics. The OSCAR-4 code is a nodal-diffusion-based deterministic code system used for reactor calculation support. OSCAR-4 consists primarily of a 2D cell calculation named HEADE which uses nuclear data from the WIMS 172-group based on JEF2.2 library collapsed into six energy groups. The 3D core calculation is then performed by Multi-Group Reactor Analysis Code (MGRAC) for utilization in depletion and reactor calculations. Once all cycles are built, the OASYS system in OSCAR-4 is used to automate the core-follow calculation. Application to the MNR using OSCAR-4 was previously studied in Alqahtani et al. (2019) to model the MNR core for the tracking of fuel composition.

The other method is the Monte Carlo method (probabilistic), which has fewer or no approximations and provides high-fidelity models for snapshot calculations. In many applications, the Monte Carlo method requires powerful computer resources owing to the detailed geometry description and the number of histories for tracking particles. The Monte Carlo Serpent 2 code is continuous-energy reactor physics code that solves the Boltzmann equations by using the Monte Carlo method. The Bateman equations are solved to account for changes in material composition due to fuel irradiation (Leppänen, 2015). The burnup calculation mode method used in Serpent 2 for solving the Bateman equations (describing the changes in the isotopic compositions caused by neutron-induced reactions and radioactive decay) is the Chebyshev rational approximation method (CRAM) using the default order values of 14 for the CRAM order (Pusa and Leppänen, 2010). The cross section library used in Serpent 2 is ENDF/B-VII in ACE format (Chadwick et al., 2006).

In this study, we applied both of the computational tools described in this section for conducting the McMaster Nuclear Reactor (MNR) simulation calculation. In both sets of simulation codes, the predictor–corrector method for calculating fuel burnup is used. This method is based upon two-step calculations performed at the beginning and the end of each step. The flux and cross section at the beginning of the step are used to deplete the fuel, and then the flux and cross section at the end of the step are calculated. In the predictor–corrector method, the averages of the two parameters are used to deplete the fuel.

### 2.2. Model description

The MNR is an open-pool-type materials test reactor (MTR). It consists of 9 by 6 assemblies that contain standard fuel assemblies (SFAs), control fuel assemblies (CFAs) with low-enriched uranium (LEU), graphite reflectors, a beryllium reflector, and a central irradiation facility (CIF).

In both sets of code, the fuel assemblies were divided into seven axial zones. This was necessary to capture axial distributions of the neutron flux and fuel depletion of each fuel assembly (FA) and CFA.

Serpent 2 captures the geometrical details of the assemblies as well as the out-of-core details such as beam tubes and additional reflectors. In OSCAR-4, two stages of calculations were performed. First, a 2D cell calculation capturing the geometrical detail and using energy condensation. Then, the 3D reactor core calculation with homogenized cross sections. Fig. 1 presents the MNR core configuration for one of the cycles used in this calculation. As can be seen from the figure, the outer core region of the MNR is flanked by a large lead block on the western periphery and six radial beam tubes on the north and east sides. The general core specifications and fuel materials of the MNR are given in Table 1 (Day, 2011).

### 2.3. Operational estimation of U-235 fuel inventory

A measurement using the flux-wire irradiation method is performed in each of the 32 fuel assemblies to determine the fuel burnup and/or depletion across the MNR core. One of the important parameters used in evaluating the fuel burnup/depletion is the U-235 consumption value [g/MWh]. This value is used together with the operational energy released [megawatt-days (MWd)] to estimate the local fuel burnup/depletion. Unlike use with the high-enriched uranium (HEU) fuel type, with the LEU fuel type the U-235 consumption valuel varies as the fuel burns (Alqahtani et al., 2019). In order to provide better operational fuel inventory data to be used in simulation code, an FIC factor will be applied and demonstrated along with the standard U-235 estimate obtained using the flux-wire method. The U-235 consumption value with LEU accounts for the energy production from other fissile isotopes; details will be discussed in Section 3.1.

### 2.4. Simulation approach

The standard operating schedule at MNR is 14 h/d Monday through Friday, with an extra shift of 8 h on some Saturdays. In the OSCAR-4 code, daily fuel inventory tracking was used, 14 h of operation and 10 h for decay shutdown, during the entire calculation period (2007–2013). This tracked the fuel inventory concentration explicitly.

The Monte Carlo probabilistic code Serpent 2 is expensive in terms of time, especially when a daily core-follow calculation needs to be applied. Therefore, temporal discretization using several time steps was applied with the aim of reducing the discretization error due to the use of constant reaction rates in the depletion calculations. However, using large time-step can lead to cause large flux change and hence inaccurate results. Therefore, small time-step to capture the flux shape over time is implemented. For instance, the maximum step-length used in Serpent-2 was around 15 days step size with 3 $MW_{th}$ power. This leads to extract energy from the hottest FA with 1.8 MWD/kgU burnup-step size. The Serpent 2 model of the MNR core is shown in Fig. 2.

The MNR server, which uses CentOS Linux computing platform, was used to run Serpent 2 code system in OpenMP parallel computing. The simulation run in OpenMP mode used was 35 parallel threads. Five hundred cycles of 80,000 neutron histories each were run, with 70 cycles skipped as inactive; therefore, a total of 40,000,000 neutron histories were simulated at each burn step.

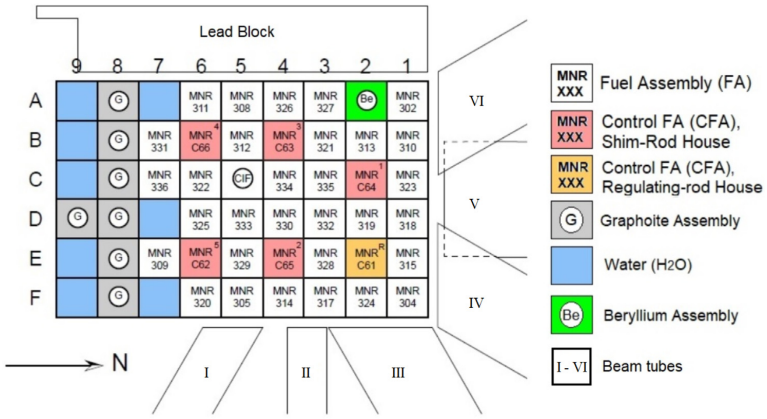


**Fig. 1.** MNR core cross section.

**Table 1**
MNR specifications (Day, 2011).

| Parameter | Value and description |
|---|---|
| Core lattice size (*x*-direction) | 8.1 cm |
| Core lattice size (*y*-direction) | 7.7 cm |
| Active core height | 60 cm |
| Fuel type | $U_3Si_2$-Al dispersion Al-clad curved plate fuel |
| Enrichment | 19.75 wt% (LEU) |
| Coolant and moderator material | Light water |
| Reflector material | Graphite |
| Fuel meat thickness | 0.051 cm |
| Fuel plate thickness | 0.127 cm |
| Coolant gap size | 0.300 cm |
| Number of plates per assembly | 16 fuelled and 2 dummy (external) |
| Fuel atom density | $1.88994 \times 10^{-3}$ at/b.cm |
| Control fuel atom density | $1.66794 \times 10^{-3}$ at/b.cm |

The maximum statistical error in the nodal assembly power was less than 0.14%. The Shannon entropy converged at approximately the 40th cycle. This was due to the geometrical division made in the axial core, by which each FA and CFA was divided into seven layers, lumping all inventory together in one node per layer. Fig. 2 shows the MNR model using Serpent 2 code system (L), and thermal flux distribution (R).

## 3. Results and analysis

### 3.1. Implementation of the correction factor

In the MNR, following measurement of the local assembly flux and collection of the recorded operational plant data (energy released in MWd), the U-235 consumption value is used continuously throughout the fuel's life to estimate the fuel depletion. A value of 0.05417 g/MWh has been used since the time when the reactor core was fully HEU fueled. In 2007, however, the MNR core was completely converted to using LEU fuel. Unlike use with HEU, with LEU the U-235 consumption value changes constantly as the fuel burns. With HEU, the concentration of the U-235 is so highly enriched that all energy produced by the fuel comes only from U-235. Even at end of life (EOL), the energy produced from non-U-235 actinides- in HEU is still negligible. Table 2 shows the energy production from HEU and LEU fuel at EOL (50% depletion) using OSCAR-4.

Given the values in Table 2, it is still acceptable to consider the consumption of an HEU fuel a constant value in the early stage of fuel life. However, LEU fuel produces significant energy from actinides other than U-235, and therefore, it is not efficient to estimate U-235 with LEU fuel by using a constant value for consumption. Accordingly, in order to adjust the recorded MNR data for U-235 to reliably estimate the core FAs, an FIC factor is introduced in this study. This factor changes continuously as the fuel burnup changes. Fig. 3(L) shows the fuel depletion content calculated using

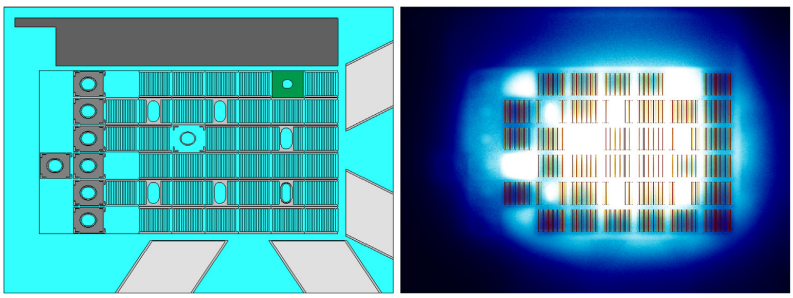

**Fig. 2.** Serpent 2 simulation code model of MNR core (L), and thermal flux distribution (R).

**Table 2**
Fraction of fission power from actinides for high-enriched uranium (HEU) and low-enriched uranium (LEU) at end of life (EOL).

| | HEU (%) | LEU (%) |
|---|---|---|
| U-235 | 99.54 | 91.21 |
| U-236 | 0.03 | 0.03 |
| U-238 | 0.01 | 0.42 |
| Pu-239 | 0.38 | 7.6 |
| Pu-241 | 0.03 | 0.73 |

the MNR and OSCAR-4 consumption value. As expected, MNR depletes more U-235 than OSCAR-4 owing to the U-235 consumption value constant used. Unlike OSCAR-4, where other fissile isotopes, i.e. Pu-239, can contribute to the energy production and hence lower consumption of U-235. Fig. 3(R) shows the FIC factor extracted from both methods of calculating depletion by dividing the MNR/HEU consumption value by the OSCAR-4/LEU value.

As described in Table 1, the MNR fresh fuel contains 225 g (1.88994 $10^{-3}$ atoms/(b.cm)) of U-235, and nominally the fuel removal is usually applied when approximately 50% depletion is reached. From Fig. 3, as expected from the information given in Table 2, less LEU fuel content is consumed using OSCAR-4 (with LEU fuel) than MNR fuel as the fuel burns. The lesser the extent to which the fuel is enriched, the greater the contribution of energy released from other fissile materials, in this case mainly Pu-239. The variation in fuel depletion as the fuel releases energy systematically alters the fuel content across the core. The effect of this variation can therefore be accounted for by applying an FIC factor to the operational recorded data, based on the values in Fig. 3 (R).

### 3.2. Validation of simulation code criticality data against operational data

Throughout the code validation, criticality operational data ($k_{eff} = 1$) were used as a benchmark for validating and comparing the simulation code used. Here, we examine the methodology used to apply the FIC factor to the initial material composition extracted from the operational data.

The MNR is a daily-operation reactor and is usually filled with irradiation samples. According to the MNR operational data, throughout the entire six-year calculation period, the reactor is shut down on December 24 and begins operation again at the beginning of the following year. This provides an opportunity to compare the $k_{eff}$ values under both the absence of xenon and the absence of samples. Fig. 4 presents the $k_{eff}$ values for the first operational day of each year along with the positions of the critical rods for each calculation.

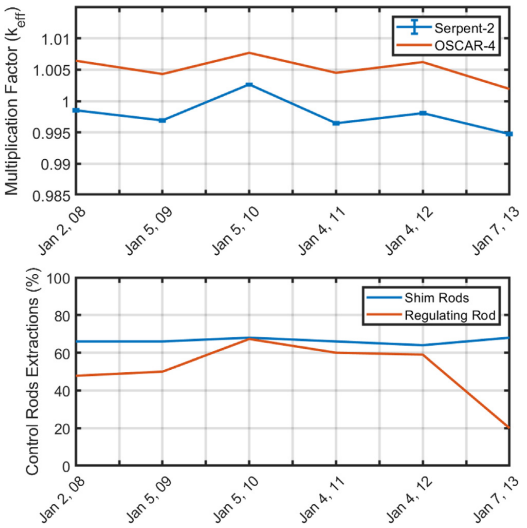


**Fig. 4.** Behavior of xenon concentration during the operational week of the measurement.

A systematic difference can be seen between the two multiplication factors. The MNR houses five shim rods and one regulating rod. The operational limits for the control rod (CRs) are usually maintained at no less than 60% and 20% extraction for the five-shim rods and one-regulating rod, respectively. Therefore, studying the CRs' worth is important for gaining an improved understanding of the differences between the code systems when all rods reach their limit of extraction.

The regulating rod's worth did not show a significant difference between the sets of code: 2.23 mk and 1.76 mk for Serpent 2 and OSCAR-4, respectively. Whereas for the five shim rods worth extraction limit, however, there was a notable difference between the two sets of code: 34.39 mk and 23.92 mk, respectively. Serpent 2 has a higher rod worth, and this is reflected in the multiplication factor, as seen in Fig. 4.

### 3.3. U-235 operational plant data with simulation code

OSCAR-4 and Serpent 2 code sets were used to simulate the MNR core for a period of six years (2007–2013). The data on four FAs for the entire calculation period are presented in this paper.

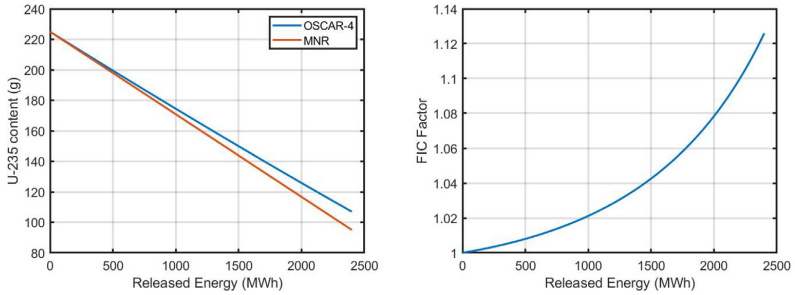


**Fig. 3.** Fuel depletion (L) (Alqahtani et al., 2019), and fuel inventory correction (FIC) factor (R).

These FAs were selected for having the shortest periods of energy release (depletion) in order to track the depletion throughout the period since its BOL. The initial condition of the depletion values for these FAs were as follows: MNR-329, 13%; MNR-330, 6.5%; MNR-332, 0.5%; and MNR-333, 1%. The amounts of U-235 in the four FAs under all four methods were compared. Fig. 5 shows the U-235 atom density as tracked using the four methods applied. The standard deviation in the flux-wire method was calculated in reference (Alqahtani et al., 2018).

The FIC factor increases exponentially as the fuel burns; this means that the flux-wire method for calculating MNR fuel depletion will tend to show higher depletion values. As can be seen in Fig. 5, the U-235 atom density under the four methods employed started at the same concentration except under the flux-wire

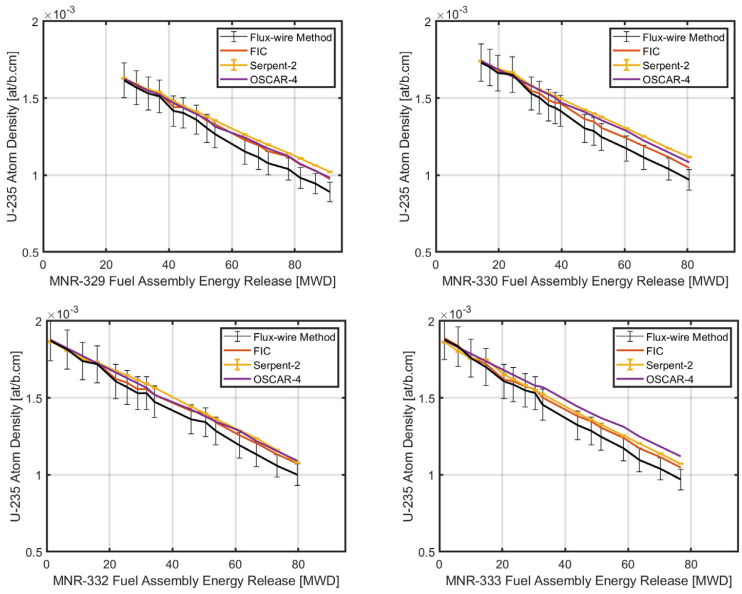


**Fig. 5.** U-235 atom density with energy release.

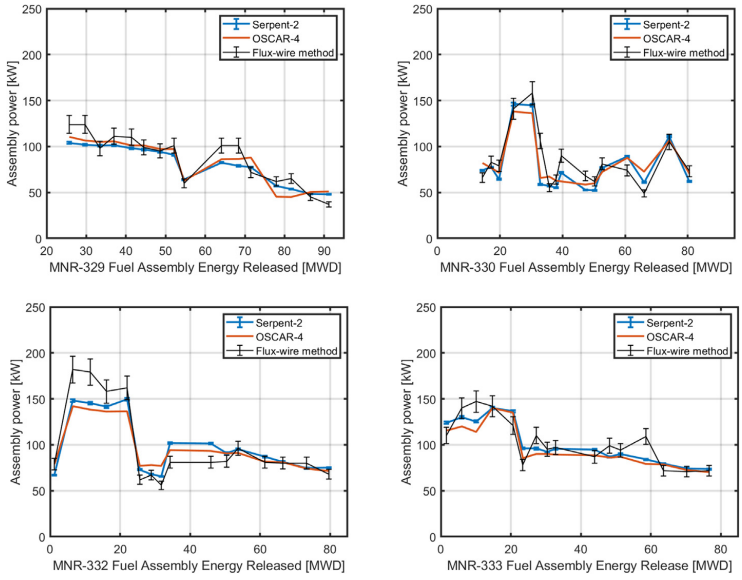


**Fig. 6.** FA power vs. energy released.

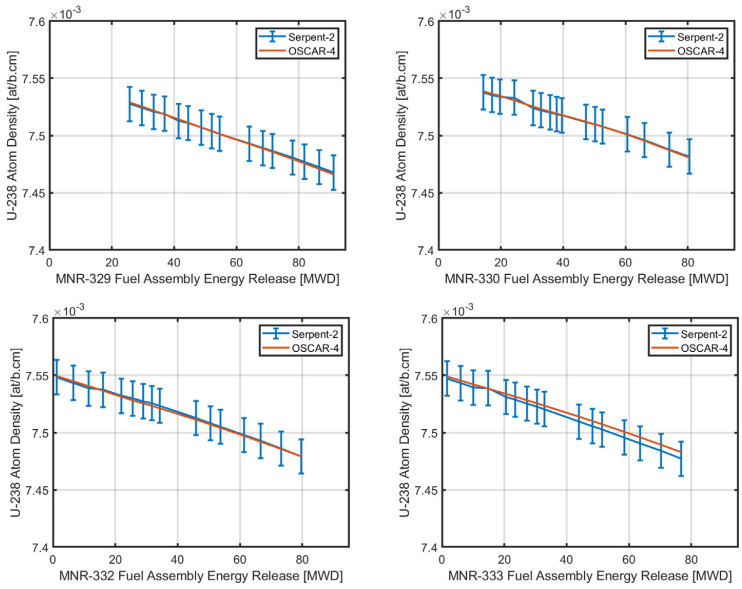


**Fig. 7.** Tracking of U-238 concentrations.

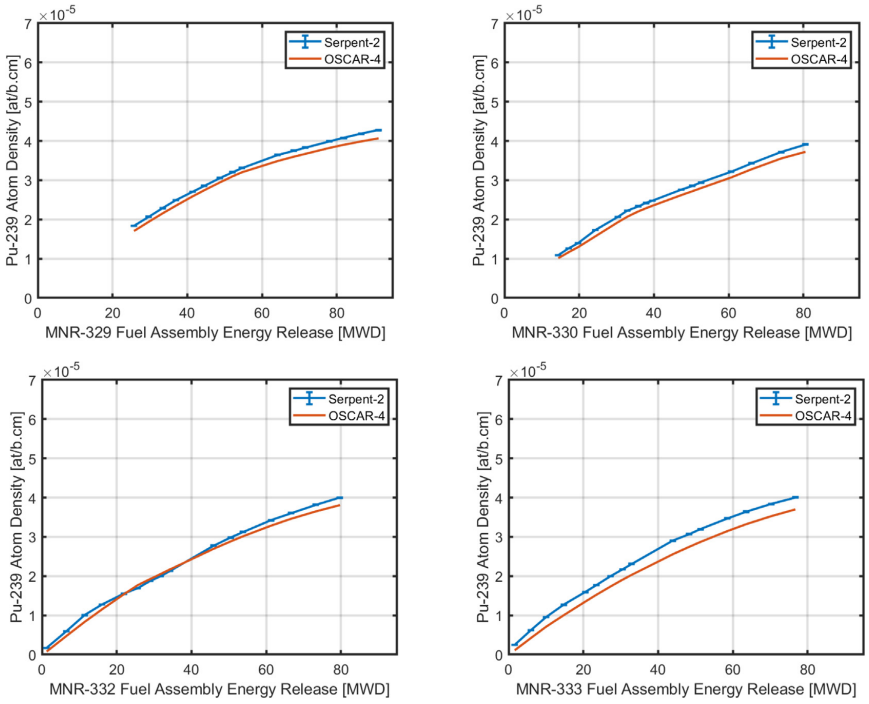


**Fig. 8.** Pu-239 tracking concentration.

method, which had a negligible lower concentration. All of the core FAs were depleted using operational core-follow history data.

One of the four methods, the flux-wire method always gave the lowest U-235 content, whereas the other three methods varied from one FA to another. Fuel time exposure was conserved under all methods, whereas FA local power varied with the method owing to the uncertainty in each method. The previous study was performed using Serpent 2 to estimate the flux-wire measurement uncertainty for estimating the local power/flux (Alqahtani et al., 2018). The flux wire is assumed to sit in the near center of each FA. However, the position of the wire may deviate from this assumed position. The uncertainty in flux-wire positioning was found to fall within the range of maximum standard deviation of 7% depending on the flux distribution inside the FA channels and FA locations. Fig. 6 shows the FA power as tracked during the core-follow calculation period along with the error bars that were extracted from the flux-wire positioning.

In Fig. 6, the main cause of the variation in the FA power is due to the fuel shuffling. This will lead the FA power to increase particularly in the region of high neutronic importance, and vice versa. Local assembly power is inevitably reflected in the U-235 atom results; i.e., the OSCAR-4 core-follow method in MNR-333 appears to provide the lowest power throughout nearly the entire calculation period. Therefore, a higher U-235 atom density is expected at the EOL calculation, as seen in Fig. 5.

### *3.4. Comparison of inventory of major isotopes between OSCAR-4 and Serpent 2*

U-235 enrichment at EOL is about 9–11%, whereas the U-238 concentration at EOL is considerably higher, about 85–87%, a major contributor of isotope content in each FA. U-238 produces energy from high-energy neutrons, and that energy is about 0.4–0.5% throughout the FA's life (Table 2). Similarly, Pu-239 is the major energy contributor after U-235. This only happens when U-235 reaches a depletion of greater than 3%, which is around 75 operational days from its initial loading at MNR core of $3MW_{th}$. Pu-239 energy production reaches 7–8% at EOL. Therefore, it is vital to track the concentrations of these isotopes when different methods and approaches are employed. All statistical errors from Serpent 2 simulation code showed in this section is below than 0.2 % and it is represented as an error bar in all figures. Fig. 7 illustrates the U-238 concentrations as tracked during the calculation period.

Pu-239 is created by the transmutation of high concentrations of U-238 into U-239 which then rapidly undergoes two -$\beta$ decays, transforms into Np-239, and via a second -$\beta$ decay is transformed into Pu-239:

$$238_{92}U + {}^{1}_{0}n \rightarrow {}^{239}_{92}U \rightarrow {}^{239}_{93}Np \rightarrow {}^{239}_{94}Pu$$

Fig. 8 shows the evolution of Pu-239 during the calculation period.

The buildup of Pu-239 is a result of neutron irradiation of the U-238. The maximum difference was found in MNR-333 at EOL with 0.08% ($5.92 \times 10^{-6}$ at/b.cm) and 7.5% ($3.07 \times 10^{-6}$ at/b.cm) for U-238 and Pu-239, respectively. These two maximum differences are negligible in comparison to the total three major isotopes presented in this section which is $8.62 \times 10^{-3}$ at/b.cm. Even though two methods and approaches were used, the inventory concentrations of U-235, U-238 and Pu-239 demonstrated very good agreement.

## 4. Conclusion

Adjusted operational core history data for a six-year period were used and compared with simulations by the OSCAR-4 and Serpent 2 code systems. The two methods use different approaches and different models. The OSCAR-4 code system uses a detailed daily core-follow calculation, whereas Serpent 2 uses a few burn-step sizes per cycle. The criticality calculation ($k_{eff}$) at the beginning of each year, when there is zero xenon poison, was also studied.

The highest difference in the U-235 fuel inventory values was found in MNR-333, with a 6.97% difference between OSCAR-4 and the FIC factor method at EOL. This is mainly due to the local power assembly. The calculated $k_{eff}$ criticality values were found to be systematically different owing to the difference in CR worth. The absolute difference in the range of reactivity values was approximately 4–6 mk and 3–5 mk for OSCAR-4 and Serpent 2 with the unity, respectively. The major isotope (U-238) content showed similar behavior under the two code systems throughout the calculation period except for MNR-333, for which a local power difference was found in the two code systems. This was reflected by the change in the Pu-239 difference for this FA.

The MNR core-follow calculation using Serpent 2 code with consideration of few time-step sizes per cycle should be able to estimate the fuel inventory in very good agreement with detailed daily core-follow tracking.

## CRediT authorship contribution statement

**M. Alqahtani:** Conceptualization, Methodology, Software, Validation, Formal analysis, Investigation, Writing - review & editing, Visualization. **A. Buijs:** Supervision. **S.E. Day:** Supervision.

## Declaration of Competing Interest

The authors declare that they have no known competing financial interests or personal relationships that could have appeared to influence the work reported in this paper.

## Acknowledgments

The authors would like to thank Chris Heysel, Director of the McMaster Nuclear Reactor, for his support in providing the reactor documents that are needed for this study. Special thanks to Dr. Dave Novog for his constructive recommendations on the results. Also, the authors would like to thank Dr. Rian Prinsloo and Dr. Francois van Heerden from Necsa for their help at the beggining of this study.

## Appendix A. Supplementary data

Supplementary data associated with this article can be found, in the online version, athttps://doi.org/10.1016/j.anucene.2020.107590.

## References

Amin, E.A., Bashter, I.I., Hassan, Nabil M., Mustafa, S.S., 2017. Fuel burnup analysis for IRIS reactor using MCNPX and WIMS-D5 codes. Rad. Phys. Chem. 131, 73–78. https://doi.org/10.1016/j.radphyschem.2016.10.019. ISSN 0969–806X. URL: http://www.sciencedirect.com/science/article/pii/S0969806X16306107.

Aldawahrah, Saadou, Dawahra, S., Khattab, K., Saba, G., Boush, M., 2018. Calculation of fuel burnup and radionuclide inventory for the HEU and potential LEU fuels in the IRT research reactor. Results Phys. 11, 564–569. https://doi.org/10.1016/j.rinp.2018.09.044. ISSN 2211–3797. URL: http://www.sciencedirect.com/science/article/pii/S2211379718316243.

Khattab, K., Dawahra, S., 2011. Calculation of fuel burnup and radionuclide inventory in the Syrian miniature neutron source reactor using the GETERA code. Ann. Nucl. Energy 38 (6), 1442–1446. https://doi.org/10.1016/j.anucene.2011.01.030. ISSN 0306–4549. URL: http://www.sciencedirect.com/science/article/pii/S030645491100051X.

Dawahra, S., Khattab, K., Saba, G., 2015. Calculation of fuel burnup and radionuclide inventory in the 10MW MTR type research reactor using the GETERA code. Ann. Nucl. Energy 78, 89–92. https://doi.org/10.1016/j.anucene.2015.01.009. ISSN

0306–4549. URL: http://www.sciencedirect.com/science/article/pii/S0306454915000109.

Dawahra, S., Khattab, K., Saba, G., 2015. Calculation of fuel burnup and radioactive inventory in the CANDU reactor using the GETERA and MCNP4C codes. Int. J. Nucl. Energy Sci. Technol.

International Atomic Energy Agency, 2008. Safety Analysis for Research Reactors. Technical report. Safety Reports Series No. 55..

Standera, Gerhardt, Prinslooa, Rian H., Müllerb, Erwin, Tomaševic, Djordje I., 2008. OSCAR-4 code system application to the SAFARI-1 reactor..

Alqahtani, M., Day, S., Buijs, A., 2019. OSCAR-4 code system comparison and analysis with a first-order semi-empirical method for core follow depletion calculation in McMaster nuclear reactor (MNR). CNL Nucl. Rev.

International Atomic Energy Agency, 2019. Benchmarking against experimental data of neutronics and thermohydraulic computational methods and tools for operation and safety analysis of research reactors. Technical report. IAEA-TECDOC-1879..

Leppänen, J., 2015. PSG2/Serpent – a continuous-energy Monte Carlo Reactor Physics burnup calculation code. VTT Technical Research Centre of Finland. User manual, 2015..

Pusa, M., Leppänen, J., 2010. Computing the Matrix Exponential in Burnup Calculations. Nucl. Sci. Eng.

Chadwick, M.B., Obložinský, P., Herman, Michal, Greene, N.M., McKnight, R.D., Smith, D.L., Young, P.G., MacFarlane, R.E., Hale, G.M., Frankle, S.C., Kahler, A.C., Kawano, T., Little, Robert, Madland, D.G., Moller, P., Mosteller, R.D., Page, Philip, Talou, Patrick, Trellue, H., Marck, Steven van der, 2006. Endf/b-vii.0: Next generation evaluated nuclear data library for nuclear science and technology. Nucl. Data Sheets 107, 2931–3060. https://doi.org/10.1016/j.nds.2006.11.001.

Day, S.E., 2011. Mcmaster nuclear reactor: Benchmark specification. Technical report. Submitted to IAEA CRP: Innovative methods for research reactors..

Alqahtani, M., Day, S., Buijs, A., 2018. Flux-wire measurements and fuel burn-up estimate comparisons with simulations for core-follow calculations at MNR Reactor. Can. Nucl. Soc.

# Chapter 6

# Experimental Measurement And Monte Carlo Code Simulation Of The Gamma Heating At Different Irradiation Sites In A Nuclear Research Reactor

Citation:

M. Alqahtani, A. Buijs, and S. Days, 2020, "Experimental Measurement And Monte Carlo Code Simulation Of The Gamma Heating At Different Irradiation Sites In A Nuclear Research Reactor", Nuclear Engineering and Design, doi: 10.1016/j.nucengdes.2020.110690

Previous chapters have extensively studied and analyzed the fuel compositions for the MNR core. In this paper, 27 gamma heating measurements have been performed in both axial and radial irradiation sites in the MNR core using the gamma thermometer apparatus. An up-to-date fuel composition extraction from the MNR core has been employed in the Serpent-2 code system. The comparisons of the measurements and the operational multiplication factor ($k_{eff} = 1$) have been conducted with the Serpent-2 code. The results have demonstrated that even though the measurement was carried out in 2019, a very good agreement of the effective multiplication factor with MNR critical rods position has been observed. In addition, a comparable of the gamma heating with the measurement results have been observed. To this extent, the methods used in this thesis allow the improvement of prediction capabilities of the Serpent-2 code, and aid in the accurate development of any future code utilization in the MNR core.

Nuclear Engineering and Design 364 (2020) 110690

Contents lists available at ScienceDirect

Nuclear Engineering and Design

journal homepage: www.elsevier.com/locate/nucengdes

# Experimental measurement and Monte Carlo code simulation of the gamma heating at different irradiation sites in a nuclear research reactor

M. Alqahtani[a,b,*], A. Buijs[a], S.E. Day[a]

[a] McMaster University, Department of Engineering Physics, Hamilton, Ontario, Canada
[b] Nuclear Science Research Institute (NSRI), KACST, Riyadh, Saudi Arabia

ARTICLE INFO

*Keywords:*
Irradiation site
Gamma heat
Gamma thermometer
Fuel assembly
Multiplication factor

ABSTRACT

Interaction of radiation with matter results in heat generation and in effect, changes in the irradiation sample's quality. Knowledge about heat deposition within the irradiation sites can go a long way in enhancing the safety and quality of the irradiation condition. To measure such results, SCK-CEN Gamma Thermometer (GT) is used for experimentally measuring Gamma Heating (GH) during the operation of McMaster Nuclear Reactor (MNR) at three irradiation sites. In addition, Monte Carlo reactor physics code (Serpent-2) is also used for modeling the MNR in order to compare as well as validate it against experimental and operational measured data such as the multiplication factor ($k_{eff}$) during the operational day against the actual values (unity), the experimentally measured GH values. After finding a difference of 0.45% at the beginning of the day and 0.32% at the end of the day in the $k_{eff}$, a comparable GH profile was observed between the measurement and the calculation. Additionally, the average axial differences of GH results found in the beryllium irradiation site (2A), and the graphite irradiation sites (8B and 8E) are 4.71%, 10.71%, and 11.72%.

## 1. Introduction

A 3 $MW_{th}$ open-pool McMaster Nuclear Reactor (MNR) is widely used for radioisotopes productions among several applications and experiments. MNR is known to house various irradiation sites, both inside and outside the reactor core. The open-pool design makes it feasible to access those irradiation sites. In many cases, samples are encapsulated before being placed for irradiation purposes. As a result, coolant is prevented from flowing through the irradiated sample (target). In any nuclear reactor, Gamma Heating (GH), which is a result of interaction of radiation with matter, can significantly contribute to the matter/sample heat generation, particularly in the absence of the direct contact coolant. Evaluation of the nuclear heat, mainly GH, at any irradiation site is one of the main important parameters for safety evaluation of in-pile irradiation samples (IAEA, 2003). For this reason, irradiation samples are typically considered under controlled conditions for high quality production. In many cases, the GH in the MNR core irradiation samples can alter both molecular structure and neutron cross section by raising its temperature and in effect, lack of optimal irradiation condition (IAEA, 2003; Harrell et al., 2018). Previous study was carried out at MNR core to irradiate medical isotope device based on holmium-166 and caused massive damage to the microspheres. According to this study, GH is the primary cause for the microspheres sample damage (Heysel et al., 2018).

A significant amount of heat is deposited their energy out of the fission sites during the reactor operation (≈15%) (Lamarsh and Baratta, 1982). This energy deposition, or the nuclear heat, arises from different types of radiations; scattered neutron, prompt gamma, delayed gamma and radiative capture emitted during the fission, decay and activation processes. All these interactions will result in heat generation/deposition at any point inside the reactor. In all irradiation samples, the GH is the main contributor to total heating (Lemaire et al., 2015). Hence, it is imperative to study the GH in those sites to gauge the safety and efficacy of irradiation targets.

In this study, experimental measurement of the GH is performed by the differential temperature thermo-couple Gamma Thermometer (GT). More specifically, GT was placed in three different irradiation sites during the reactor operation to axially measure the GH. The reactor power remained constant at 3 $MW_{th}$ and the control rods (CRs) extraction positions were recorded during the measurement campaign. Additionally, Monte Carlo Serpent-2 code was used for modeling the MNR core to be compared and validated against the measurement data.

## 2. McMaster nuclear reactor (MNR) description

The MNR is an MTR-type reactor with a core of low enriched

* Corresponding author.
*E-mail addresses:* alqahm1@mcmaster.ca, malqahtani@kacst.edu.sa (M. Alqahtani).

https://doi.org/10.1016/j.nucengdes.2020.110690
Received 12 February 2020; Received in revised form 7 May 2020; Accepted 8 May 2020
Available online 21 May 2020
0029-5493/ © 2020 Elsevier B.V. All rights reserved.

**Table 1**
A general description of the MNR facility and core specifications.

| Parameter | Specification |
|---|---|
| Type of reactor | Open-pool MTR |
| Maximum/nominal power | 5/3 $MW_{th}$ |
| Maximum neutron flux (3 $MW_{th}$) | $5.8 \times 10^{13}$ $n/cm^2$ s |
| Coolant and moderator | light water |
| Reflector | graphite and beryllium |
| Coolant circulation | natural circulation or forced downward flow |
| Fuel type | $U_3Si_2$-Al dispersion Al-clad plate fuel |
| Fresh SFA and CFA atom density | $1.89 \times 10^{-3}$ and $1.67 \times 10^{-3}$ at/b.cm |
| Enrichment | 19.75 % |
| Control system | 5 Ag-In-Cd shim safety rods and 1 stainless steel rod |
| Plate, fuel meat and cladding thickness | 0.127, 0.051 and 0.038 cm |
| Core lattice size x and y | 8.1 and 7.709 cm |
| Core height | 60 cm |

uranium (LEU) fuel. The MNR core grid comprises of six by nine assemblies wherein there are 32 standard fuel assembly (SFA), six control fuel assembly (CFA), seven graphite reflector assemblies and one beryllium assembly (Day, 2011; Alqahtani et al., 2019). The LEU fresh fuel is made up with 19.75% enrichment. Light water is used for moderating and cooling the reactor core. MNR contains several irradiation sites, both inside and outside the core. The in-core irradiation sites are situated in the graphite reflector (G) and beryllium reflector (Be). The MNR core lattice size for all assemblies are 8.1 cm by 7.709 cm. The inner irradiation diameters of beryllium and graphite reflectors are 3.81 and 3.50 cm, respectively. Table 1 shows the MNR general description, Fig. 1 demonstrates the MNR core configuration, and Fig. 2 shows the cross-sectional view of the SFA and the CFA.

## 3. Method

### 3.1. Measurement set-up

The GH measurement campaign was performed on Tuesday, October 08, 2019 in MNR core to axially map the GH in three different irradiation sites. More specifically, the GH measurement was performed at 20:15 at night. MNR is a daily operating reactor, therefore it is preferable to run the measurement few hours following the reactor start-up to burnout the excess of xenon concentration in order to avoid a high Control Rods (CRs) fluctuation.

A small dimensions Gamma Thermometer (GT), manufactured by the SCK-CEN in Belgium, was used to perform the measurement (Aarestad, 1992). The GT measures the gamma heating through the differential temperature thermocouple between hot and cold junctions. Notably, the hot junction is insulated in the core of the GT, whereas the cold junction is placed 6 cm above, outside the GT core, and establishes contact with coolant water. Fig. 3 and 4 illustrate the GT attached to metallic in-pile and out-of-pile instrument cables, as well as its cross-sectional view, respectively.

The GT and the differential thermocouple are made of AISI 304 and AISI 316L stainless steel material, respectively. The hot junction, which forms the inner GT core, is insulated by Argon gas at 1.25 MPa. It can mainly be heated, and is eventually higher than the cold junction, when GH is present. Light particles such as gamma rays will generate heat (GH) when they interact with the GT core. In contrast, the cold junction is continuously cooled by the coolant flow and can be assumed to have a temperature similar to the coolant temperature. Both inlet and outlet reactor coolant temperatures were recorded at around 30 and 36 Celsius degree. The GT is connected to a K-type thermocouple which processes data (voltage) whenever there are different temperatures between hot and cold junction. The signals processing of the different temperatures (voltage creating) is recorded to a PC adjacent the reactor pool on a frequency of 1 Hz.

The GT is mounted in an instrument rig to be placed in any irradiation site i.e. graphite and beryllium reflectors. The rig comprises of both an inner race and outer body. The outer body is fixed after being mounted on the graphite/beryllium site whereas the inner race is axially movable. The GT outer rig can fit inside the irradiation site. The movable inner rig, with a diameter of 1.27 cm, allows the GT instrument to sit laterally anywhere within 1.27 cm. A detailed description of the mounted GT can be found in reference (Stoll, 2016).

The GT instrument can be axially positioned at any elevation from A to I. The axial elevations differences between one level and another is about 5 cm. The inner race contains a guide tube that is attached to the lower part and can then be placed within any irradiation site. The calibration factor specified by the supplier of the GT sensitivity is equal to 44.7 ± 4.5 °C g/W.

For each axial elevation changes, the shim rods (SRs) and regulating rod (RR) extraction positions were recorded during the measurement, 100% is fully extracted and vice versa with respect to the fuel height. The SRs were only change 0.7%, from 78.3 to 79% extraction, during all the measurement campaigns, whereas the RR was ranged from 65 to 72% when the GT was located in 2A and from 40 to 45% when it was in 8B and 8E. Table 2 illustrates the GT axial changes in 8B assembly with CRs extractions in (%). Measurement was performed twice top-to-bottom and bottom-to-top in each irradiation site.

The axial elevations points of the GT rig are the A to I levels. Each level has a GH value inside the irradiation site in the reactor core from the bottom to top, respectively. These levels are different between beryllium and graphite reflectors owing to the different base level positions between the two reflectors, which is around 3.2 cm lower in the graphite reflector.

The three different sites were selected based on the most accessible adjacent sites to the reactor core. The reactor power was recorded during measurement campaign at 3 ± 0.02 $MW_{th}$. The GT was axially

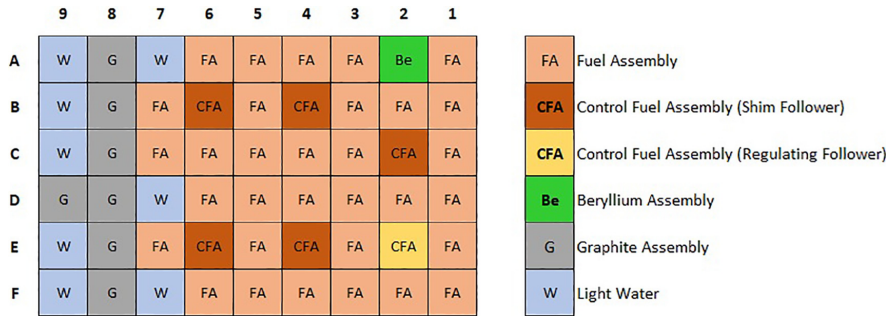


**Fig. 1.** MNR core configuration.

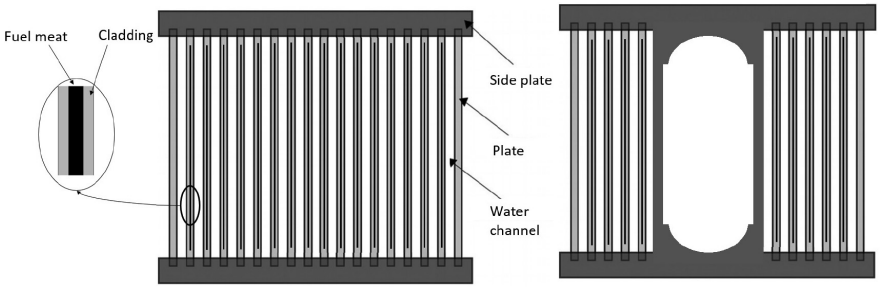


**Fig. 2.** Cross-sectional views of SFA (L), and CFA (R).

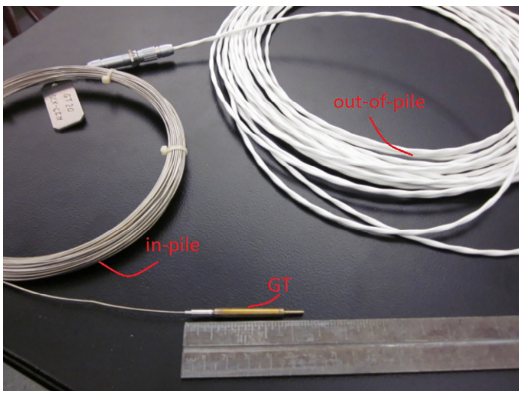


**Fig. 3.** GT attached to the cables.

moved by the mounted rig in each site to measure the GH. This was done twice from Bottom-To-Top (BTT) and Top-To-Bottom (TTB) subsequent to which an average of the two measurements is calculated. For each axial GH measurement, either BTT or TTB, an average of ten GH values was obtained after a period of five time constants. This will yield less uncertainty when collecting several data points.

### 3.2. Calculation

#### 3.2.1. Calculation process

A full 3D core Monte Carlo neutron and photon transport model Serpent-2 has been used to validate and compare parameters against operational and measured data. The photon physics in Serpent-2 was implemented in 2015 (Kaltiaisenaho, 2016). Recent development has been undertaken for photon physics to estimate the energy deposition at any location inside a reactor core.

**Table 2**
GT axial elevations and data recorded in 8B.

| Axial Elevation | GT Data Collection | Five SRs (%) | RR (%) |
|---|---|---|---|
| A | 21:57:30 | 79 ± 0.30 | 40 ± 0.30 |
| B | 21:59:50 | 79 ± 0.30 | 40 ± 0.30 |
| C | 22:01:50 | 79 ± 0.30 | 40 ± 0.30 |
| D | 22:04:11 | 79 ± 0.30 | 42 ± 0.30 |
| E | 22:06:25 | 79 ± 0.30 | 43 ± 0.30 |
| F | 22:09:03 | 79 ± 0.30 | 44 ± 0.30 |
| G | 22:12:35 | 79 ± 0.30 | 44 ± 0.30 |
| H | 22:15:05 | 79 ± 0.30 | 45 ± 0.30 |
| I | 22:22:55 | 79 ± 0.30 | 45 ± 0.30 |

In Serpent-2, energy deposition calculation is performed every time a photon or a neutron interaction occurs. In photon interaction, the energy deposition calculation uses analog method for tracking photons event-by-event. Photon interaction deposits their energy by: photo-electric effect, Compton scattering and pair production. Whereas in neutron, other than fission, the energy deposition is calculated using kinetic energy released in materials (KERMA) coefficients. As described in reference (Tuominen et al., 2019), the nuclear heating, or neutron/photon heating, calculation in Serpent-2 can be expressed as

$$H(E) = \sum \sum \rho_i k_{ij}(E)\Phi(E) \quad (1)$$

where $\rho_i$ is the number density of nuclide i, $k_{ij}$(E) is the KERMA coefficient for nuclide i and reaction j at incident energy E, and Φ(E) is the scalar neutron/photon flux. Nuclear data processing NJOY (Macfarlane et al., 2018) can be used to calculate KERMA coefficients, which is necessary for neutron heat deposition.

The energy deposition treatment in Serpent-2 is calculated on the basis of the user's needs. Four modes (0–3) exist for calculating the energy deposition: constant energy deposition per fission, local energy deposition, local photon energy deposition and coupled neutron-photon transport. The most advanced energy deposition mode, coupled neutron-photon transport (mode 3), is used in this investigation (Tuominen

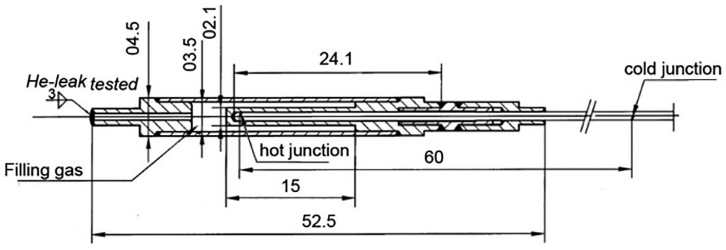


**Fig. 4.** Cross-sectional view of the GT built by SCK-CEN (Fourmentel et al., 2013).

et al., 2019). In this mode, the fission site energy deposition, which is calculated based on ENDF MF1 MT458 data (Trkov et al., 2018), is given by

$$E_{fiss,i} = EFR + EB \quad (2)$$

Where EFR denotes the fission products' kinetic energy, and EB is the delayed beta energy. The two components from the previous equation deposit their energy at the fission site. Meanwhile particles such as photon and neutron dissipate their energy through the medium.

The delayed gamma energy deposition in Serpent-2 can be calculated by using one of the two different calculation methods: (1) by solving Bateman equations to produce delayed gamma source then the calculation can be read from a binary file. Once the binary file of fission products and activated materials in the reactor is created, the secondary simulation calculation can be used to estimate the delayed gamma, (2) or by approximating delayed gamma energy deposition with the same distribution as the prompt gamma energy distribution (Tuominen et al., 2019). The approximated delayed gamma energy deposition is used for this study as it provides a significant reduction in the calculation time.

#### 3.2.2. Monte Carlo Serpent-2 modelling of the MNR

It is important to consider several parameters when validating or comparing results of the experimental measurement with the computational code. These parameters include: core configuration, reactor power, CRs extraction position, as well as fuel core inventory. All these parameters were thoroughly considered and recorded during the measurement.

The MNR Serpent-2 model includes the reactor core, the reflector and the surrounding beams – all of which are modelled explicitly as described in Section 2.

The MNR core inventory modelling in Serpent-2 was extracted on the basis of the reactor core operational data history at the date of measurement. The implementation of the fuel compositions extraction from the measurement-base estimate followed the procedure utilized in reference (Alqahtani et al., 2020). The nuclear data library used in this model is ENDF/B-VII.1 (Chadwick et al., 2011).

The GT instrument was modeled with the same materials that were provided, see Section 3.1. All the statistical uncertainties are kept lower than 1.5% in all GH calculations with 10,000 active histories and 80,000 particles per history, a total of $8 \times 10^8$ particles. The calculational time performed of this simulation were 39 h with 20 OpenMD parallel threads. Owing to the computational expense associated with the calculational time, a simple approximation in the GT calculation model was implemented by assuming the energy deposition occurred between the hot and cold junctions. Fig. 5 illustrates the MNR Serpent-2 model used in this work, see Section 2 for a detailed description.

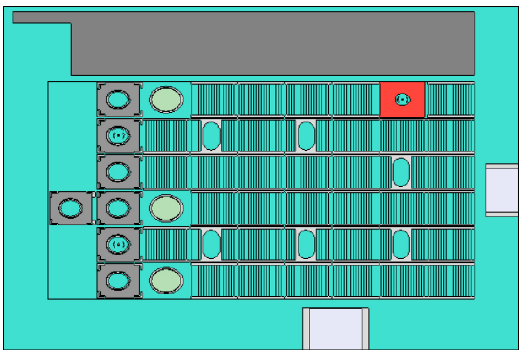

**Fig. 5.** MNR Serpent-2 model.

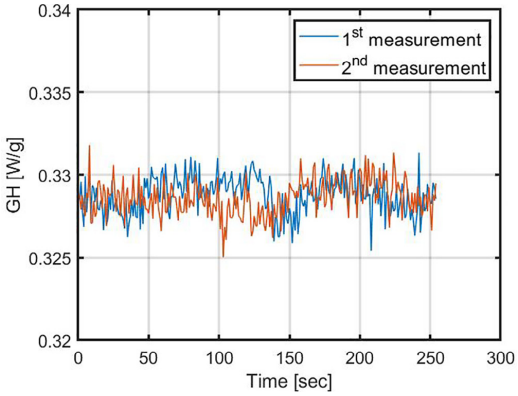


**Fig. 6.** Measured GH in two different times.

## 4. Results and analysis

### 4.1. Uncertainty quantification (UQ)

A series of measurements and simulations were conducted to evaluate some parameters that can influence the calculated/measured GH quantities. These results can be affected by several factors owing to the uncertainty caused by the reactor conditions, measurement conditions and calculation approximation such as CRs position, reactor power and GT spatial positioning, among others. Therefore, to ensure proper treatment of these uncertainties, several sources of uncertainties associated with the measurement are discussed. Other uncertainties related to the nuclear data and dimensional tolerance are disregarded.

#### 4.1.1. Minor contributions

One of the main kinds of calculation uncertainties is the physical approximations made by the computer code model. The GT dimension is small, see Fig. 4, therefore moving the instrument in each measurement and simulating the model is computationally expensive. To avoid that, the GT length was assumed to be all throughout the axial irradiation sites. A number of simulations were conducted to evaluate the effect of such parameters. The differences of these approximations were seen within the relative statistical error ($< 0.6\%$). Therefore, this assumption will help reducing the calculation time, which is 9 axial points in each irradiation site (27 times reduction).

Other recorded reactor operational and instrumental uncertainties are not seen significant such as: reactor power, which can be assumed to be proportional to the GH results, $3 \pm 0.02$ MW $_{th}$; CRs position fluctuations $\pm 0.5$ %; and electronic noise with a maximum around $\pm$ 0.8% from the average value. The latter can be seen in Fig. 6. In addition, studying uncertainty of the short-live isotopes decay was performed during the measurement. This is done by measuring each GH in two different times. Fig. 6 shows two measured GH at the same axial point and irradiation site (beryllium) in two different times (≈1 h different). No variation can be seen from the two measured GH in Fig. 6 and the GH values are seen within the electronic noise.

Aside from estimated uncertainties from the measured and calculated GH values, other assumptions that have inherent uncertainties need to be evaluated, such as the assumption of the cold junction temperature being similar to the hot junction ambient temperature, see Section 3.1. The average temperature difference between the inlet and the outlet core flow obtained from the MNR control room is $5.55 \pm 0.05$ °C. The distance between the hot and cold junction is 6 cm, see Fig. 4, and the core height is 60 cm. The MNR core flow is downward with inlet and outlet temperature above and below the core,

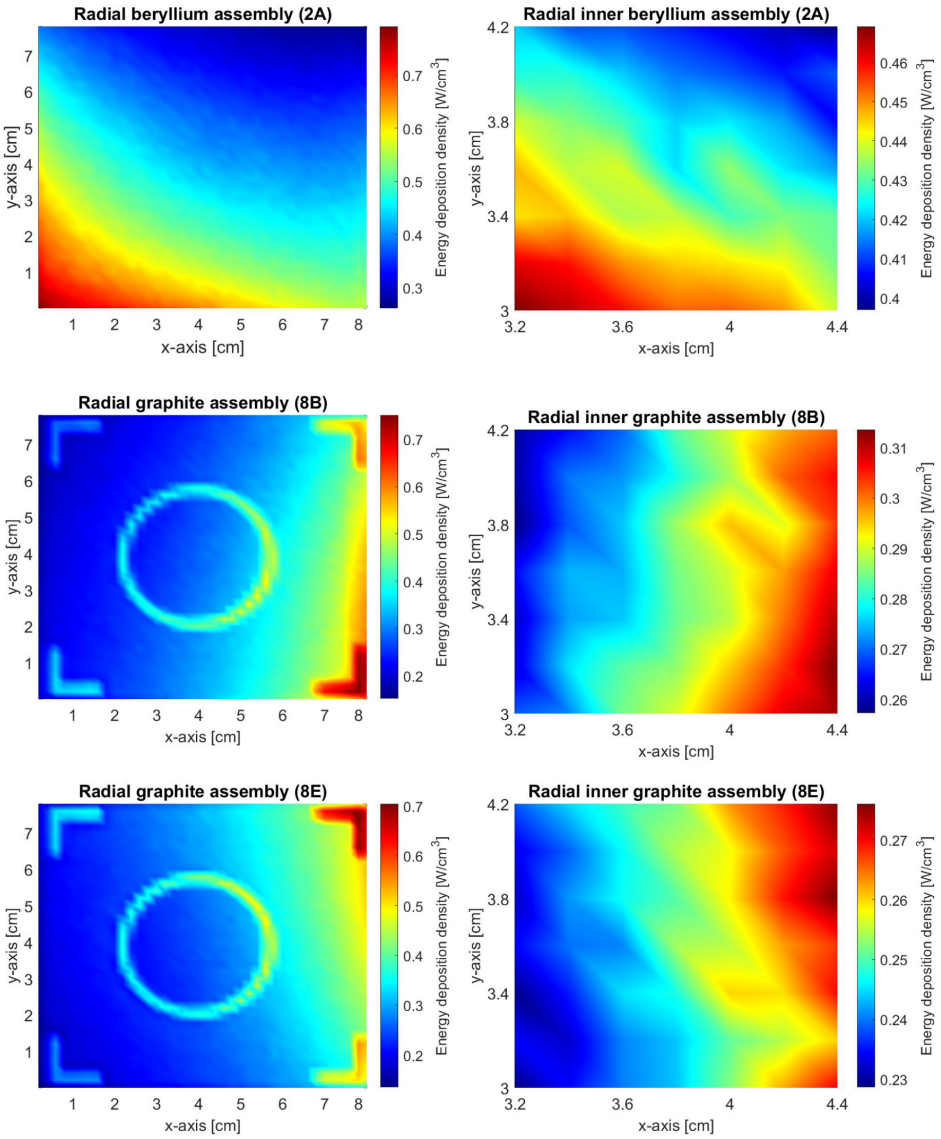


**Fig. 7.** Irradiation sites and inner lateral placement energy deposition density [W/cm$^3$].

respectively. This means that the ambient GT temperature between the two junctions is not exactly uniformed; the cold junction temperature is slightly underestimated (colder). These deviation in the temperature differences contribute to the uncertainty associated with the GH measurement. Therefore, assuming a linear axial temperature increment between inlet and outlet temperatures core (≈0.1 °C/cm) can induce uncertainty in the GH of 1.4%.

#### 4.1.2. Major contributions

In order to optimize the measurement results, measurements should always be accompanied by its uncertainty. Lack of uncertainties studies, especially those with major influences, may lead to underestimate the GH deposition, which then leads to the possibility of drawing inconsistent conclusions about the fidelity of code simulation. In this section, major uncertainties are studied by Serpent-2 code and illustrated along with the measured values in Section 4.1.1. Those are: (i) the GT radial (lateral) placement inside the irradiation site, and (ii) the maximum and minimum CRs extraction position.

Energy Deposition Density (EDD) will be used in studying the radial GT position in unit [W/cm$^3$] to demonstrate the average EDD distribution across different reflector assembly. The only different between EDD and GH is the density division. Fig. 7 illustrates the EDD across the three irradiation sites (L) as well as the lateral GT placement (R). The irradiation site, in Fig. 7 (L), represents the complete radial cross

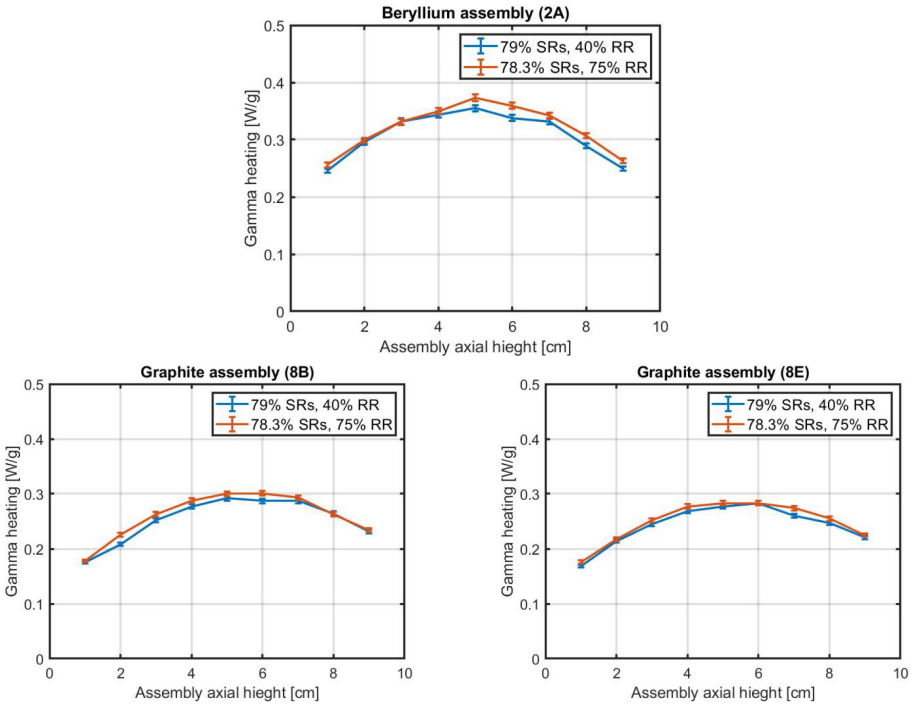


**Fig. 8.** GH calculation in three irradiation sites with different RR positions.

**Table 3**
Summary of the uncertainty terms in each irradiation site.

| | Uncertainty Estimate (%) | | |
|---|---|---|---|
| | Beryllium (2A) | Graphite (8B) | Graphite (8E) |
| Power | 0.7 | 0.7 | 0.7 |
| Electronic noise | 0.8 | 0.8 | 0.8 |
| Lateral placement | 4.1 | 5.1 | 5.0 |
| Temperature Differences | 1.4 | 1.4 | 1.4 |
| Combined $u_{c_k}(y)$ | 4.5 | 5.4 | 5.3 |

sectional assembly 8.1 by 7.709 cm, whereas the lateral GT placement in Fig. 7 (R) focuses in the possibilities of the GT locations inside the irradiation site in Fig. 7 (L). The variations in EDD is primarily attributed to the photons interaction variation as the material mass number and/or density changes.

As expected, the EDD is hotter at the corners toward the MNR core centre, refer to Fig. 7 (L), same for GT lateral placement (R). In the three reflector assemblies, the standard deviation of the lateral GT placement shows 4.1%, 5.1% and 5% from the central irradiation placement for site 2A, 8B and 8E, respectively.

On the other hand, the GH uncertainty existence due to the CRs variation is inevitable. For that reason, two Serpent-2 models were used with different CRs positions, considering the maximum and minimum extraction positions during each measurement which are: 79% and 78.3% for the five SRs, and 75% and 40% for one RR. Fig. 8 shows the GH calculations in the three irradiation sites with different CRs extraction positions.

As can be seen from Fig. 8, the GH in the beryllium irradiation site is the most vulnerable to the CRs changes. The upper half part shows a higher GH when RR is 75% extraction owing to the higher local flux and hence local power near to the RR. Whereas the impact of the CRs on the axial GH in the majority points of the graphite sites are within the statistical uncertainty error. This deduces that the CRs fluctuation in this measurement does not significantly impact the GH in the graphite irradiation sites. This may be attributed to the insignificant change in SRs (0.8%) and the RR distant from the graphite irradiation sites, as seen Fig. 1. Therefore, in order to simulate and compare the GH calculations with measured values, CRs extractions in the beryllium site need to be precisely considered. Fortunately, as mention in Section 3.1, the RR fluctuation during the GH measurement in the beryllium site was solely moved 7% (65–72%), therefore an average of the RR extraction will be used which is 68.5%.

It is difficult to draw conclusions from uncertainties lying within the statistical errors, therefore some of minor uncertainties discussed previously will not be considered in the final combined uncertainty. Table 3 summarizes and tabulates all uncertainties that will accompany the measured values. The final combined uncertainty for each irradiation site was calculated as following (International Bureau of Weights and Measures, 2011)

$$u_{c_k}^2(y) = \sum_{i=1}^{N} u_i^2(y) \tag{3}$$

Where $u_{c_k}(y)$ is the combined uncertainty of an estimate y (GH), irradiation site k, and $u_i(y)$ is the uncertainty of each independent parameter defined in this section.

### 4.2. Comparison with operational and measurement results

The calculated $k_{eff}$ was compared to the actual value of unity ($k_{eff} = 1$) when CRs positions were in a critical position on Tuesday (measurement day). The reactor operated on Monday for 14 h and was shutdown for 10 h before being resumed on Tuesday. The calculated

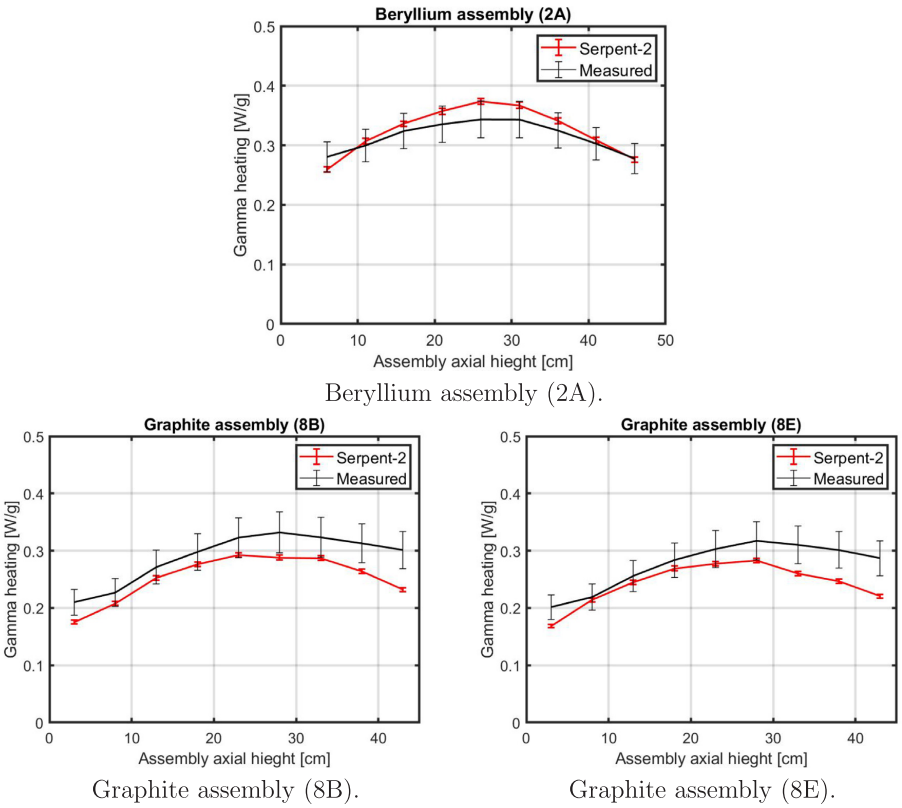


Beryllium assembly (2A).

Graphite assembly (8B). Graphite assembly (8E).

**Fig. 9.** Calculated and measured NH in [W/g] in three different irradiation positions.

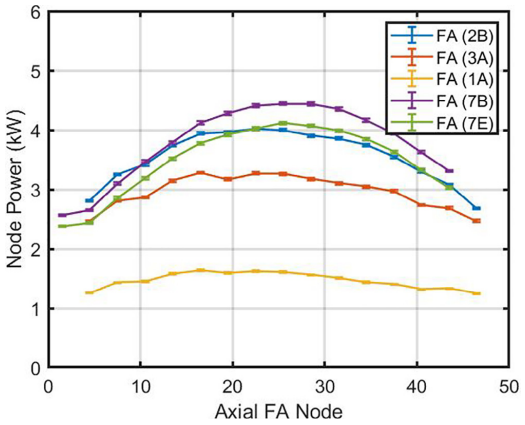


**Fig. 10.** FA axial power profile using Serpent-2 model.

$k_{eff}$ on Tuesday at the beginning of day (BOD) using Serpent-2 with 95% confidence interval is 1.00451 ± 0.00028, whereas the $k_{eff}$ at the beginning of the measurement time, which is about at the End Of Day (EOD), is 1.00322 ± 0.00028.

The bias of the calculated $k_{eff}$ from expected values ($k_{eff}$ = 1.00) are 0.45% and 0.32% Δk. Several conclusions can be drawn from the $k_{eff}$ biases that include: (i) the exact time of the MNR full power start-up as xenon concentration is usually peaked on the next day (7-9 h following shutdown); (ii) the CRs biases in both operator's recording time and the extraction position uncertainty (± 0.5%), (iii) unlike CFAs, the axial fuel burnup of the SFAs were modelled symmetrical, which in turn can cause a positive reactivity to the reactor core. The axial fuel burnup distribution of the MNR core are asymmetry, more burnup toward the lower region, due to the persistent existence of the CRs in the upper region of the MNR core.

All the calculation results and statistics-related uncertainties of the GH that were previously presented in the UQ are collected and considered in the measured GH results. Fig. 9 illustrates both the measured and calculated GH values. In the three irradiation sites, three axial GH results were presented: the beryllium irradiation site (2A) is surrounded by three fuel assemblies and as expected, it has the highest GH values. Meanwhile, the GH values of the other two irradiation sites have GH values are very similar to each other due to the lower power neighboring, and only one fuel assembly neighboring from one side.

A comparable GH profile was observed in the three irradiation sites between Serpent-2 and measurement values. The axial calculated values are systematically greater than the measured experimental ones in the beryllium assembly, with the exception of the values with the axial peripheries; the opposite were also observed in the graphite assemblies.

An average difference, in the Be (2A) site, of 4.71% was observed with measured values. In addition, an average of 10.71% and 11.72% were observed in the graphite assembly 8B and 8E. One limitation of

our implementation of the 3D FA calculation is that it was assumed to have an identical axial power distribution, cosine shape. However, in order to implement the exact modeling, the control rods insertion effect on FAs has to be considered, not only on the CFAs. Consequently, the differences between the measured and calculated GH can be attributable to that limitation. The GH profile is higher in the beryllium assembly (2A), the major attributable to this is the nearest FAs powers, as illustrated in Fig. 10.

The discrepancies between the two values, calculated and measured GH, are expected owing to the power distribution differences, which in turn, has a direct impact on the GH values. Although the maximum axial power is seen in FA (7B), which is next to graphite site (8B), the GH values are seen to be higher in the beryllium irradiation site. This is due to the higher power when summing the adjacent FAs located around the beryllium site (1A, 3A and 2B).

The three axial GH values are considered to be a strong reason for damage in some material target. These values will be taken into consideration for any future irradiation samples conditions.

## 5. Conclusion

An experimental instrumentation measurement of the GH at three different irradiation sites in the MNR core were measured and simulated. The results of the measurement were used, in addition to the operational multiplication factor, as a benchmark, in order to compare and validate them with a Monte Carlo Serpent-2 code model. Major and minor uncertainties quantification in both measured and calculated GH were analyzed and studied.

The biases of calculated $k_{eff}$ from operational value are higher by 0.45% and 0.32% $\Delta k$ for BOD and EOD, respectively. Most of the calculated GH results are in a good agreement within the measured GH uncertainties described in Section 4.1. A systematic higher GH was observed in the beryllium sites and the opposite in the graphite sites. This study is significant in that it provides a framework of a new methodology of comparing MNR measurement data with simulation codes.

Future research could examine the impact of the axial asymmetric fuel burnup distribution on the GH results. In addition, study of the cold junction temperature inside the reactor core could also provide additional important information to the measured GH values.

## CRediT authorship contribution statement

**M. Alqahtani:** Conceptualization, Methodology, Software, Validation, Formal analysis, Investigation, Writing - review & editing, Visualization. **A. Buijs:** Supervision. **S.E. Day:** Supervision.

## Declaration of Competing Interest

The authors declare that they have no known competing financial interests or personal relationships that could have appeared to influence the work reported in this paper.

## Acknowledgement

Authors would like to thank reactor staff for their help during the experiment. Also, thanks to the reactor manager Rob Pasuta for providing the fuel burnup distribution at the date of the measurement. Finally, I wish to acknowledge Dr. Dave Novog for his valuable suggestions during this study.

## Appendix A. Supplementary data

Supplementary data associated with this article can be found, in the online version, athttps://doi.org/10.1016/j.nucengdes.2020.110690.

## References

Aarestad, O., 1992. In-core instrumentation for LWRs, presented at IAEA meeting on in-core instrumentation and in-situ measurements in connection with fuel behaviour, held in Petten, The Netherlands. URL: https://inis.iaea.org/collection/NCLCollectionStore/_Public/28/018/28018794.pdf.

Alqahtani, M., Days, S.E., Buijs, A., 2019. OSCAR-4 Code System Comparison and Analysis with a First-Order Semi-Empirical Method for Core-Follow Depletion Calculation in McMaster Nuclear Reactor (MNR), CNL Review.

Alqahtani, M., Days, S.E., Buijs, A., 2020. Serpent-2 and OSCAR-4 computational tools compared against mcmaster nuclear reactor improved operational data history for U-235 fuel inventory tracking, local power tracking and validation of multiplication factor. Ann. Nucl. Energy.

Chadwick, M., Herman, M., Obložinský, P., Dunn, M., Danon, Y., Kahler, A., Smith, D., Pritychenko, B., Arbanas, G., Arcilla, R., Brewer, R., Brown, D., Capote, R., Carlson, A., Cho, Y., Derrien, H., Guber, K., Hale, G., Hoblit, S., Holloway, S., Johnson, T., Kawano, T., Kiedrowski, B., Kim, H., Kunieda, S., Larson, N., Leal, L., Lestone, J., Little, R., McCutchan, E., MacFarlane, R., MacInnes, M., Mattoon, C., McKnight, R., Mughabghab, S., Nobre, G., Palmiotti, G., Palumbo, A., Pigni, M., Pronyaev, V., Sayer, R., Sonzogni, A., Summers, N., Talou, P., Thompson, I., Trkov, A., Vogt, R., [van der Marck], S., Wallner, A., White, M., Wiarda, D., Young, P., 2011. Endf/b-vii.1 nuclear data for science and technology: Cross sections, covariances, fission product yields and decay data. Nucl. Data Sheets 112 (12), 2887–2996. https://doi.org/10.1016/j.nds.2011.11.002.. Special Issue on ENDF/B-VII.1 Library. URL:/http://www.sciencedirect.com/science/article/pii/S009037521100113X.

Day, S., 2011. McMaster Nuclear Reactor Specification. IAEA CRP 1496: Innovative Methods for Research Reactors.

Fourmentel, D., Reynard-Carette, C., Lyoussi, A., Villard, J.F., Malo, J.Y., Carette, M., Brun, J., Guimbal, P., Zerega, Y., 2013. Nuclear heating measurements in material testing reactor: a comparison between a differential calorimeter and a gamma thermometer. IEEE Trans. Nucl. Sci. 60 (1), 328–335.

Harrell, C., Djonov, V., Fellabaum, C., Volarevic, V., 2018. Risks of using sterilization by gamma radiation: the other side of the coin. Int. J. Med. Sci. 15, 274–279. https://doi.org/10.7150/ijms.22644.

Heysel, C., Armstrong, A., Bennett, J., Werger, E., Naperstkow, Z., Pasuta, R., 2018. Customized irradiation sites for medical isotope production. Can. Nucl. Soc. 50.

International Bureau of Weights and Measures, 2008. Evaluation of measurement data – guide to the expression of uncertainty in measurement, JCGM.

Kaltiaisenaho, T., 2016. Implementing a photon physics model in serpent 2; fotonify-siikkamallin kehittäminen serpent 2-koodiin, G2 pro gradu, diplomityö (2016–06-14). URL:/http://urn.fi/URN:NBN:fi:aalto-201606172612.

Lamarsh, J.R., Baratta, A.J., 1982. Introduction to Nuclear Engineering. Addison-Wesley, Reading, Massachusetts.

Lemaire, M., Vaglio-Gaudard, C., Lyoussi, A., Reynard-Carette, C., 2015. For a better estimation of gamma heating in nuclear material-testing reactors and associated devices: status and work plan from calculation methods to nuclear data. J. Nucl. Sci. Technol. 52, 1–9. https://doi.org/10.1080/00223131.2015.1009957.

Macfarlane, R., Muir, D.W., Boicourt, R.M., Kahler, A.C., Conlin, J.L., 2016. The NJOY Nuclear Data Processing System, Tech. Rep. LA-UR-17-20093. Los Alamos National Laboratory.

Manual for reactor produced radioisotopes, Tech. Rep. IAEA-TECDOC-1340. International Atomic Energy Agency IAEA, 2003.

Stoll, K., 2016. A time-dependent description of in-core gamma heating in the mcmaster nuclear reactor (Ph.D. thesis). McMaster University.

Trkov, A., Herman, M., Brown, D.A., 2018. ENDF-6 Formats Manual – Data Formats and Procedures for the Evaluated Nuclear Data Files ENDF/B-VI, 555 ENDF/B-VII and ENDF/B-VIII (Tech. Rep. BNL-203218-2018-INRE). Brookhaven National Laboratory.

Tuominen, R., Valtavirta, V., Leppänen, J., 2019. New energy deposition treatment in the serpent 2 monte carlo transport code. Ann. Nucl. Energy 129, 224–232. https://doi.org/10.1016/j.anucene.2019.02.003.

# Chapter 7

# Time-dependent and MCNP-6.2 Code Evaluations of Gamma Heating

This chapter describes the study of measuring and evaluating gamma heating such as time-dependent gamma heating, decay gamma heating, as well as integrated decay GH to the nuclear transport MCNP-6.2 code calculation. Also, the MCNP-6.2 code was compared with the prompt GH from Serpent-2 to as well as the total GH with different evaluation of the secondary GH.

## 7.1 Introduction

During reactor operation, gamma rays are mainly produced by fission processes. In addition, gamma decay, especially with short half-lives, can also contribute to total gamma heating. As a result, the amount of gamma heating is a measure of local power generation. Additionally, minutes following reactor shutdown, high fuel burnup is more radioactive (high GH) than those with low fuel burnup.

This chapter presents calculational and experimental analyses for the GH aiming at developing high-quality models. A few other factors have been studied to explore their effect on the GH level using the GT instrument, see appendix C. Additionally, analysis of the experimental GH results of two different time-dependent GH scenarios is presented as follows: (i) reactor operation (RO) GH time-dependent for five consecutive years (2016-2020), and (ii) reactor decay (RD) GH following MNR shutdown. Lastly, the Monte Carlo N-Particle MCNP-6.2 model will be utilized to calculate the GH and compare with the measurement and Serpent-2 code.

## 7.2 Time-Dependent Reactor-Operation Gamma-Heating (TD-RO-GH)

Over the past few years (2016–2020), the MNR core has not altered its core burnup configuration or distribution significantly. However, fuel shuffling and/or loading is part of the MNR core fuel management routine. These changes cause core reactivity variation, and consequently, neutron and photon flux fluctuations across the core.

Any disturbance may lead to changes in the GH. Therefore, GH evaluation based on measurements in which both time and core changes are considered will be investigated. Figure 7.1 presents the GH collected data at the beryllium site (2A) throughout the past four years. Each value is an average of hundreds of measured values at the central axial point. All uncertainty contributions, which were described in chapter 6, are included in each measured value.

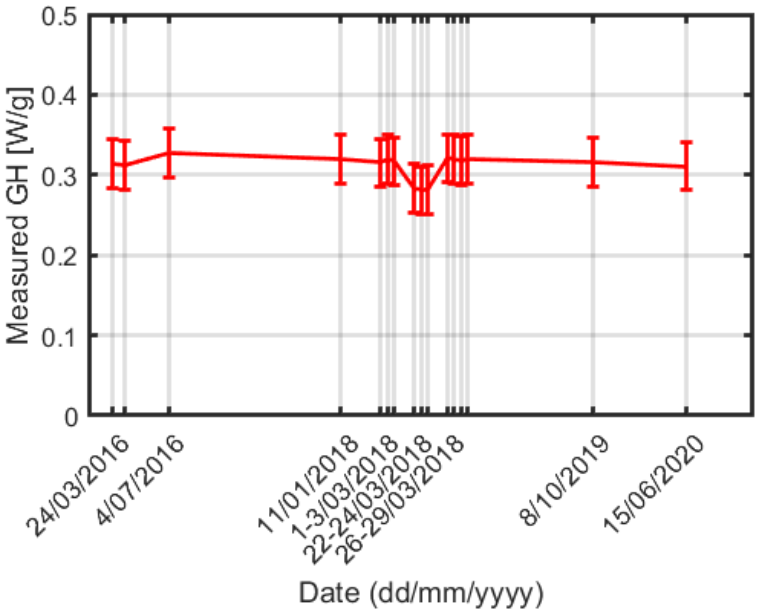


FIGURE 7.1: Measured gamma heating on several days during the period 2016-2020.

Even though the core pattern and/or configuration is different in each measurement, no significant changes have been observed in the GH values. A recently published work [22] was performed for local neutron flux level variation in one of the irradiation sites and concluded that despite that the core shuffling that had been performed, no change in the local flux was observed during the five months in operation.

However, in March 2018, it was found that the GH suffered a drop during a week of operation. Although the GT instrument was kept in the same position, a change of about 7-8% was observed. Subsequently, it was found that due to the failure in the RTD calibration, which indicated a higher reactor power than the actual power. This resulted in an apparently lower GH on 22-24 of March before correct calibration was performed.

Another cause for such fluctuations in Figure 7.1 could be the fuel burnup distribution across the MNR core. During the last four years, the MNR core follows a certain burnup distribution across the core and as a result no disturbance in fluxes may encounter. The fresher the fuel assembly, the higher neutron importance will have and as a result increase in local power. Figure 7.2 shows the MNR U-235 depletion in (%) distribution for each measured GH shown in Figure 7.1.

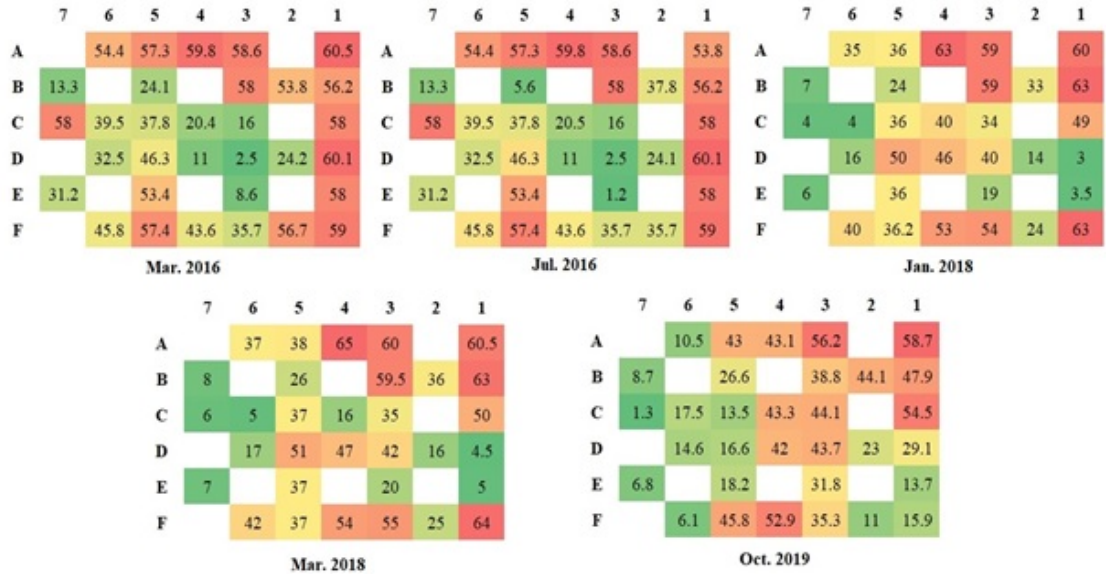


FIGURE 7.2: Fuel depletion distribution in (%) for the measured GH shown in Figure 7.1.

Altering the core burnup distribution can cause fluctuations in local power levels, thus changing GH values. To demonstrate, the Serpent-2 Monte Carlo code was utilized to calculate local power distribution, see Figure 7.3, considering the core burnup distribution shown in Figure 7.1.

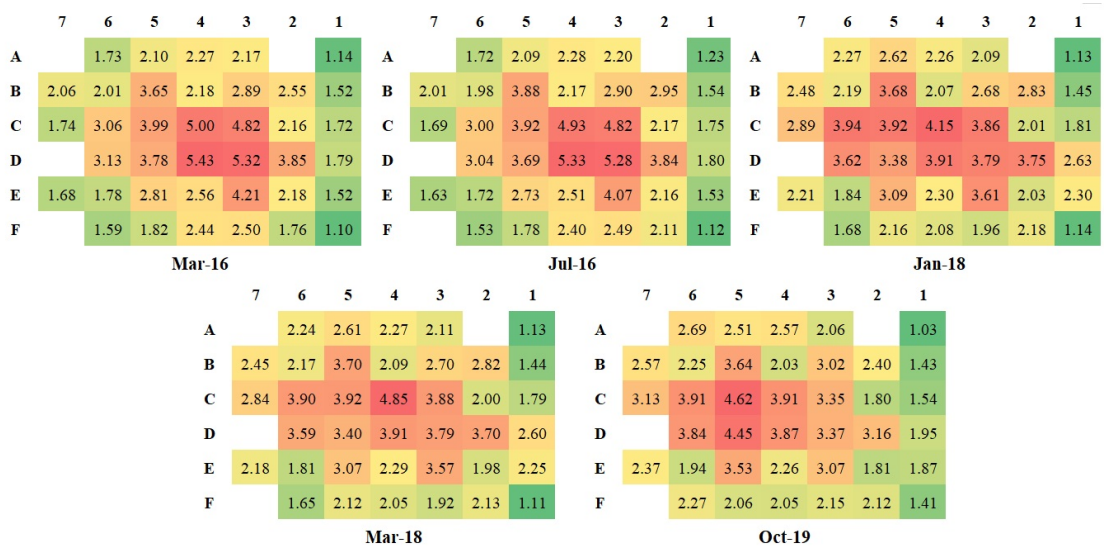


FIGURE 7.3: Local power assembly fraction distribution in (%) for the measured GH shown in Figure 7.1.

## 7.3 Time-Dependent Reactor-Decay Gamma-Heating (TD RD GH)

### 7.3.1 Calculated RD-GH During Reactor Operation

Radioactive decay heat plays an important role in nuclear safety. It contributes to the heat generation during both the reactor operation and reactor shutdown. Some radioactive isotopes are extremely radioactive and decay within a very short time—they usually have

half lives of seconds or a few minutes, while others stay for years contained in the fuel.

Decay heat estimation relies heavily on computer code predictions. Therefore, instead of approximating the decayed heat using a correction factor, as in chapter 6, a delayed gamma source would have to be produced by solving the Bateman equations. This feature will be used to calculate the decay heat for all MNR fuel nodes. Figure 7.4 shows the calculated and measured GH results in four irradiation assemblies.

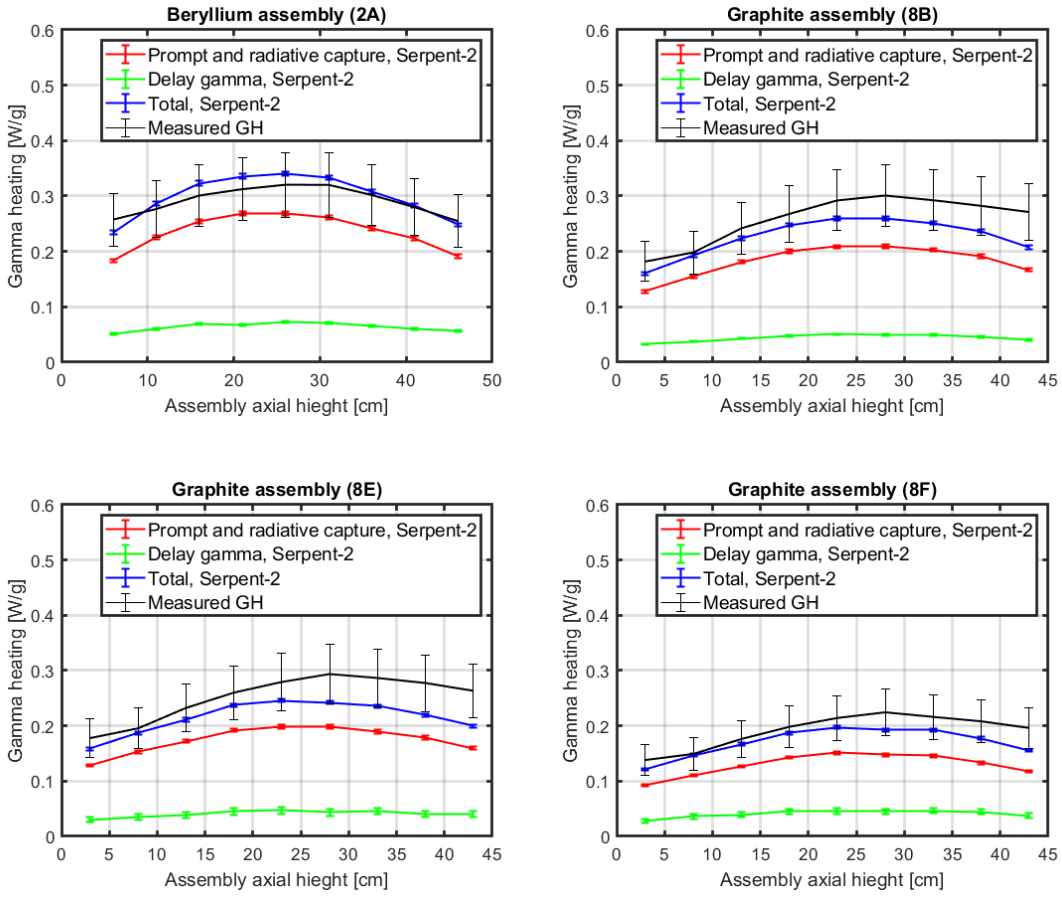


FIGURE 7.4: Measured and calculated axial gamma heating.

Most of the calculated gamma decay heat values fall within $21 \pm 0.5$ % and $19 \pm 0.5$ % of the total GH generation for the Be and the graphite assemblies, respectively. One reason for this $\approx 2$ % difference is the surrounding fuel burnup, which is higher in the Be assembly's surroundings than in the graphite assemblies' surroundings, see Figure 7.2.

### 7.3.2 Measured and Calculated Decayed GH

It was previously demonstrated that following the reactor shutdown, the decay heat starts to decay exponentially before reaching a level of heat corresponding to the surrounding fuel assemblies' burnup and distance. In this section, the decayed GH will be considered for the rod drop method where all neutron population following reactor shutdown is cut off shortly after the rods drop. Figure 7.5 shows the measured and calculated decay GH following the reactor shutdown at the center axial for different irradiation sites, 2A and 8A.

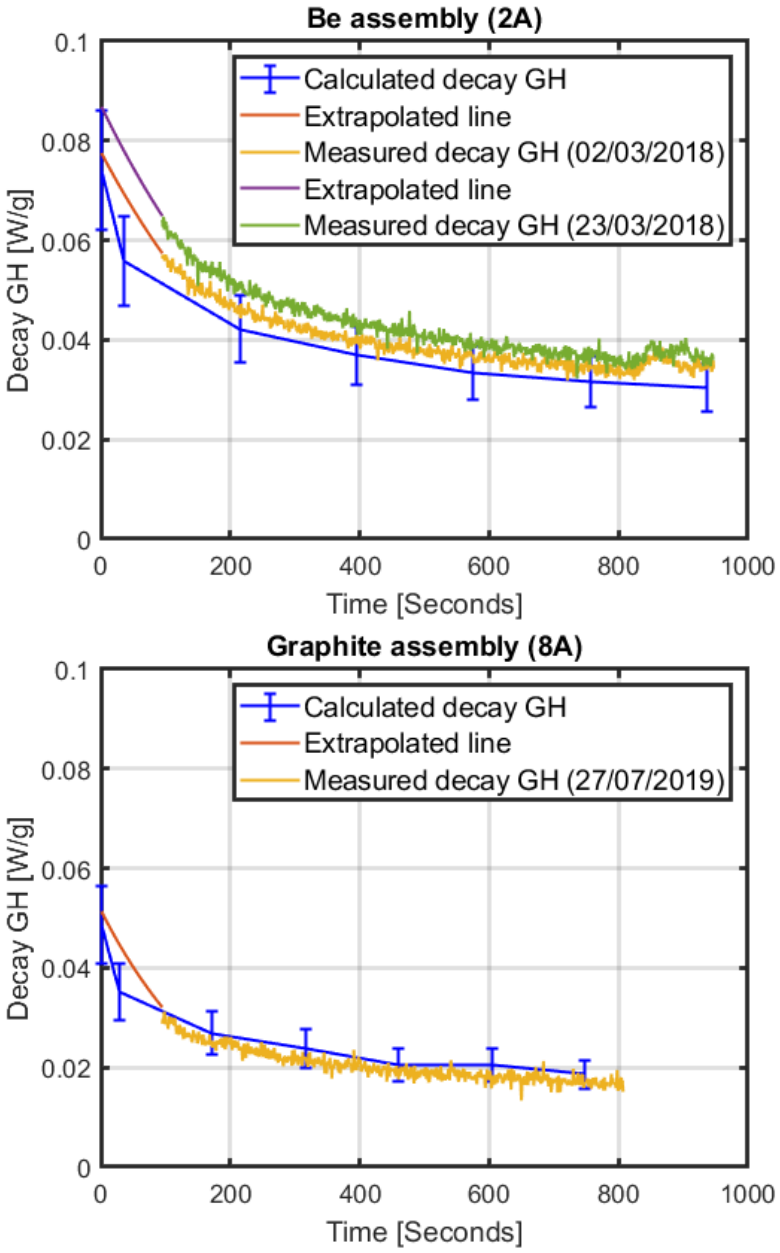


FIGURE 7.5: Decay GH at two irradiation sites.

The measured and calculated GH values in Figure 7.5 were in close agreement. The corresponding calculated delayed GH values at time zero for all figures fall within 24 ± 2.0 % for the total GH

generation. Additionally, the decay GH profiles following the reactor shutdown for both measured and calculated GH were comparable. It is noteworthy that the difference between the delayed GH after 500 seconds in all irradiation sites can only be attributed to the surrounding number of fuel assemblies, burnup and distance.

While multiple measurements of the decayed GH may allow the effects of fuel burnup to be determined through purely experimental methods, no significant variation in the GH results was observed. Nevertheless, this scenario has been observed and can only be true when core burnup pattern distribution was relatively conserved. A significant change in the core burnup pattern was made to further investigate this issue and study the impact of the fuel burnup core change on the GH levels. This was done by shuffling the fresh fuel assemblies from locations 7B and 7E with the high burnup fuel assemblies in 3A and 1A, and vice versa. Figures 7.6 and 7.7 show the GH levels considering both cases, before and after fuel shuffling for MNR core 2019 and MNR random core, respectively.

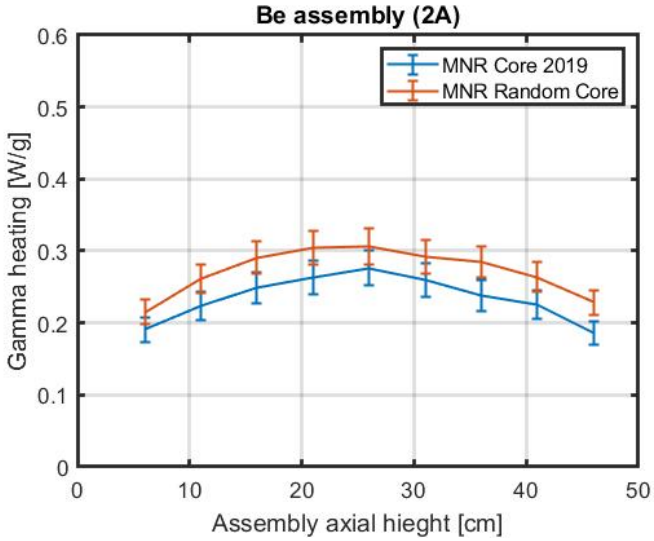


FIGURE 7.6: Prompt GH in Be assembly, before and after core configuration change.

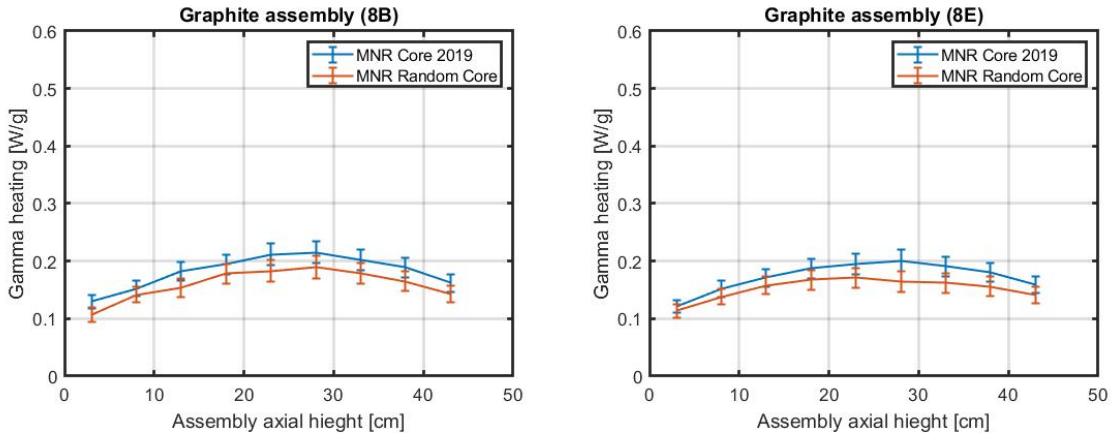


FIGURE 7.7: Prompt GH in graphite assembly, before and after core configuration change.

The computational results in Figure 7.6 and 7.7 indicate that the effect of the fuel shuffling on the GH calculations led to a 10% deviation on the GH values. This occurred only if fresh fuels were loaded/moved from one half of the core to the other.

## 7.4 Implementation of The Monte Carlo MCNP-6.2 Code

Code simulations are tools that are continuously needed for development and investigation in nuclear research and the nuclear industry. Measurements and operational data available can be used as a benchmark for simulation codes. Monte-Carlo code MCNP-6.2 has been utilized to evaluate the multiplication factor and GH. In addition, the Serpent-2 calculation will also be compared with MCNP-6.2. The atom density used in MCNP-6.2 was taken from the Serpent-2 code in each calculation, where the FIC factor in the fuel concentration was previously applied. This was the first time the atom density was updated from the core composition 54A from 2007 in the MCNP-6.2 model for the MNR.

### 7.4.1 MCNP6.2 Multiplication Factor Calculation

The purpose of this section is to calculate the multiplication factor $k_{\text{eff}}$ as well as the GH values using the MCNP-6.2 code with the corrected number density obtained from previous chapters. The results of the MCNP-6.2 will be compared with the measured and operational data, and two-simulation codes used in this research (Serpent-2 and OSCAR-4). Figure 7.8 shows the MNR core (55E, Jan. 2008) model as implemented MCNP-6.2.

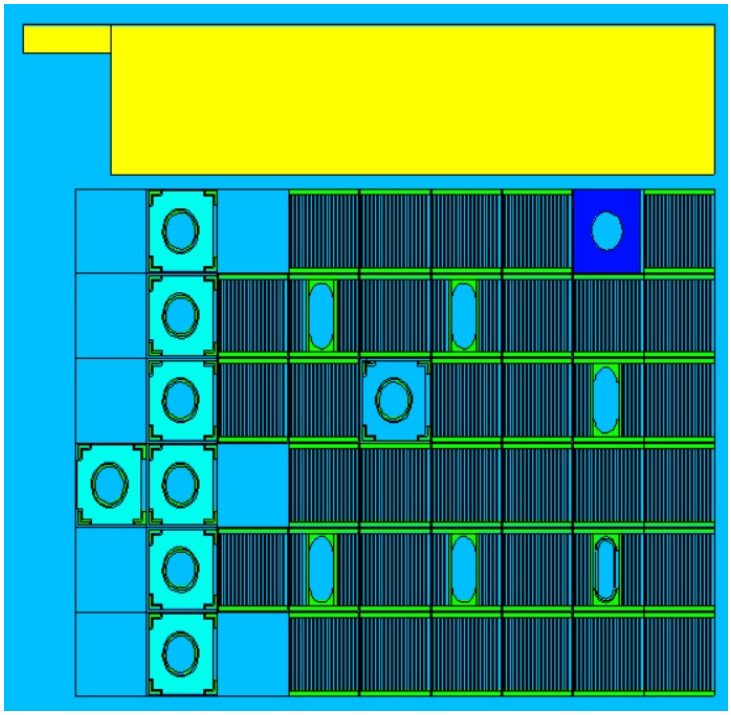

FIGURE 7.8: MNR core 55E, Jan. 2008, as modelled in MCNP6.

In this model, a pathway similar to that of the multiplication factor calculation was followed. The detail of the procedures was explained in chapter 4. The core patterns selected for this calculation were based on the absence of the major core neutron poison Xe-135. As documented in the MNR core history, the core shutdown period lasts for a minimum of ten days before the reactor starts up at the beginning of the year. The atom densities used in MCNP-6 were taken from the Serpent-2 code, about 360 isotopes for each node (273 nodes), with around 100,000 isotopes. In the MCNP-6.2 model, all statistical uncertainties of less than 2.5% were achieved by running the KCODE calculations with 15,000 particles per history and 2500 active histories. Figure 7.9 shows the multiplication factor for six consecutive years using three simulation codes.

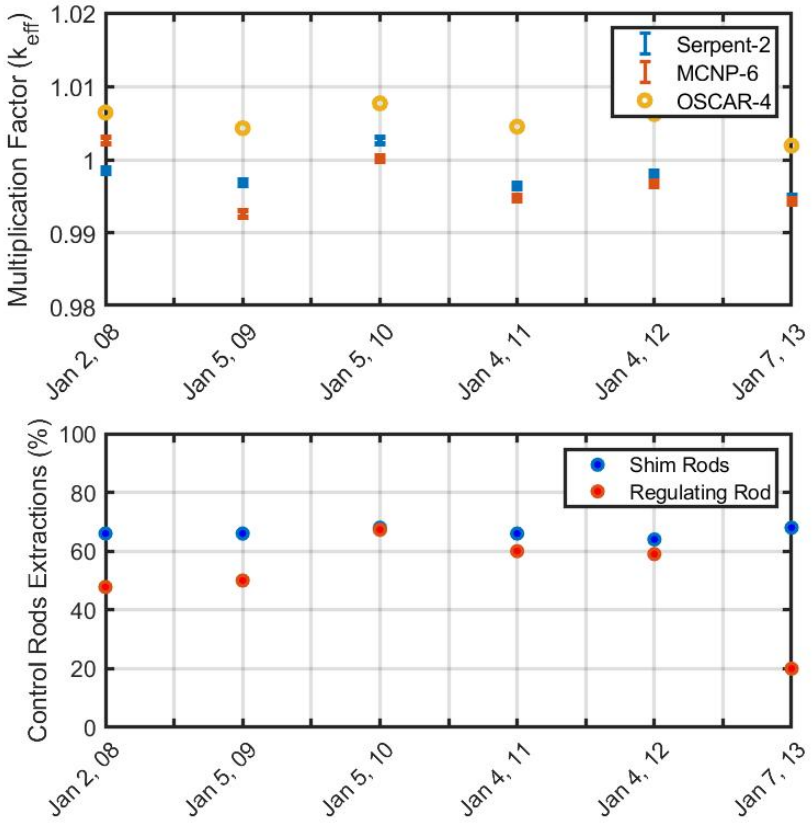


FIGURE 7.9: The multiplication factor and the critical rods positions for six consecutive years.

As previously demonstrated, the major cause of the differences between the Serpent-2 and OSCAR-4 multiplication factors is the difference in control rods worth between them. Accordingly, MCNP-6 and Serpent-2 used the same method for calculating the neutron transport equation and thus have quite similar control rod worths. The maximum difference was near 1 mk.

### 7.4.2 Axial Primary Gamma Heating

Another parameter compared, in addition to the multiplication factor, was the axial GH at four different irradiation sites, see Figure 7.10. Those axial GH values were compared with the Serpent-2 simulation model. In both models, prompt GH values were axially compared in 36 points inside the core.

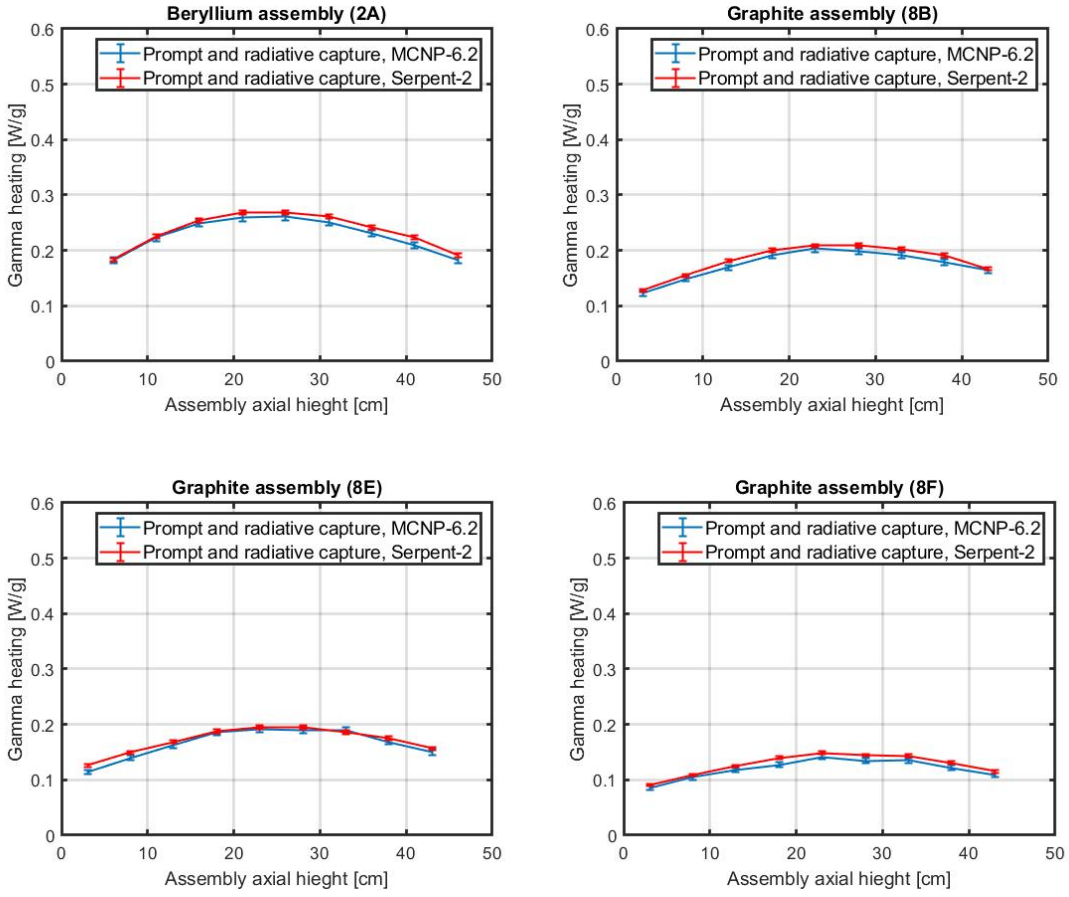


FIGURE 7.10: Prompt GH in four irradiation sites using Serpent-2 and MCNP-6.2.

The MCNP-6.2 results tie in well with previous Serpent-2 studies. Overall, the MCNP-6.2 GH results agree with those calculated by

Serpent-2. A similar conclusion can be drawn when comparing the two codes.

### 7.4.3 Integrating Measured Delayed GH with the MCNP-6.2 Calculated Prompt GH

The delayed measured and calculated GH components evaluated in section 7.6.2 were around 30% of the total GH generation. This fraction of delayed GH contribution will be implemented into the calculated prompt GH from MCNP-6.2, see Figure 7.11.

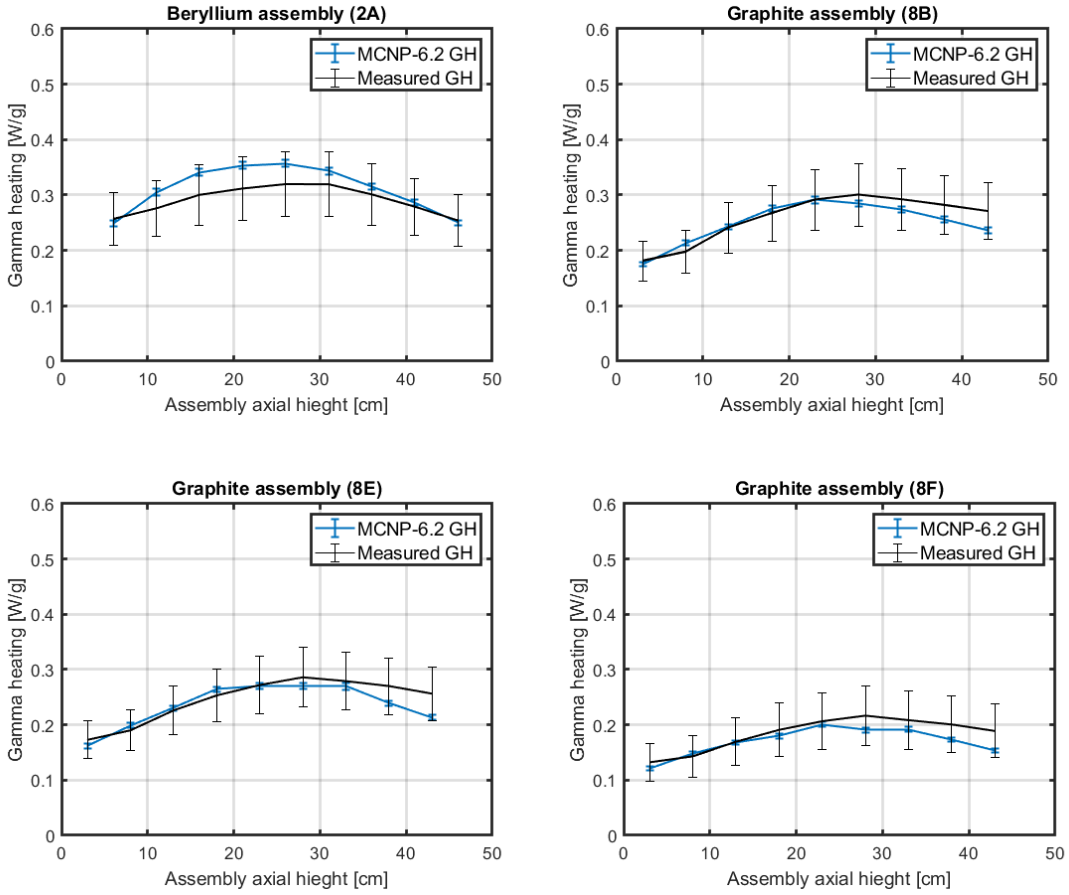


FIGURE 7.11: MCNP-6.2 GH against measured GH in four irradiation sites.

The results in Figure 7.11 confirm that the integrated measured GH with the prompt calculated GH is a great option for estimating the total GH, as opposed to a calculational process such as those used in Figure 7.4. The results are consistent with what has been found in Figure 7.4. In fact, implementing the delayed GH from the measured estimate is not even computationally expensive in terms of calculation.

As previously mentioned, one limitation of these methods is that they lack the asymmetric axial fuel inventory. Even though this

limitation is not a major concern, future study is recommended.

Additionally, these findings provide information about the aggregation of measurement data to the calculated GH. In fact, during the last seven years of collected measured GH results, it is found that the delayed GH is contributing to the total GH with around 30 $\pm$5 % of the total GH.

# Chapter 8

# Summary, Conclusion and future work recommendation

## 8.1 Summary

This thesis describes unique contributions to the understanding of the McMaster Nuclear Reactor (MNR) core, specifically related to fuel consumption and management, and gamma heating calculations and measurements. The work offers several advancements that aid in the MNR core optimization and code validation. The methodologies presented in this thesis regarding fuel consumption also apply to all other material testing reactor types (MTR).

In this work, a set of existing codes was applied for the first time to the MNR to be benchmarked against the measurements and reactor operation plant data. The codes used are the deterministic code OSCAR-4, which includes both the 2D HEADE code and the 3D MGRAC code, and the stochastic Monte Carlo reactor physics simulation codes Serpent-2, and MCNP-6.2. The MNR plant data were employed along with gamma heating (GH) measurements to assist and verify the simulation codes for MNR as well as to evaluate

the GH in the MNR core. In addition, time-dependent GH measurements, both while MNR was operating and shortly after it shut down, were investigated for a period of five years.

Chapter 3 presented the OSCAR-4 code comparison and analysis with the MNR fuel depletion from the flux-wire measurements. The results diverged over the calculation period. This was mainly due to the lack of Pu-239 energy production estimates from the MNR plant data. The findings suggested that OSCAR-4 provides a better option for core-follow calculation than operational estimates as it includes all fissile isotopes during the reactor core calculation as well as the axial fuel inventory distribution. Based on the operational schedule and reactor power in this study, around six years of core-follow simulation would be needed to be completely independent of the initial operation MNR fuel estimate.

In chapter 4, the Monte Carlo code Serpent-2 was introduced to compare against the OSCAR-4 code. The same conditions were applied to study the variation and discrepancies between them. Unlike the OSCAR-4 code, the Serpent-2 code averaged the control rods (CR) travel distance during the calculation, while the OSCAR-4 calculation kept accurate track of their positions. The Serpent-2 and OSCAR-4 codes were checked, and their performance is demonstrated and assured to be comparable. Although the CRs' motion was averaged with two burn steps over the 240 days with 5 $MW_{th}$ in Serpent, accuracy loss was not observed for the fuel concentration inventory. In fact, it showed that for both codes, the CRs' averaging is a promising option for long-cycle core follow calculations.

Chapter 5 focused on improving the MNR operational fuel consumption calculation by considering all fissile isotopes rather than

only U-235. The results showed that the fuel assemblies are removed from the core with an overestimation of the U-235 consumption around $\approx$ 13% (30 g). In this work, a new method has been applied to correct the MNR U-235 data history by implementing fuel inventory correction (FIC) factor. The fuel inventory results following FIC factor implementation were broadly consistent with the simulation codes OSCAR-4 and Serpent-2. The divergence in the fuel inventory was solved, and the multiplication factor was improved. The finding here suggests that it is possible to apply the FIC factor to existing conservative fuel burnup estimates to produce more accurate estimates consistent with estimates from detailed burnup modeling.

Chapter 6 continued comparing and benchmarking simulation codes with measurement data. In this part, the FIC factor, presented in chapter 5, was used to update the fuel inventory core depletion configuration map at the measurement date. The reactivity bias showed 3.2 and 4.5 mk at the beginning and end of the measurement, respectively. The gamma heating showed a good agreement in the beryllium assembly, with an average difference of 4.71%, and a systematic difference in the graphite assemblies, of 10.71% and 11.72%. Nevertheless, most of the 27 GH values are within the uncertainty ranges. The results here also introduce confidence in the simulation codes used since the beginning of this research. Therefore, it is vital to consider the FIC factor in any future work that requires simulation comparison with MNR.

In chapter 7, the time-dependent gamma heating (GH) was investigated during reactor operation over the course of five years. It was found that unless a significant change in the core burnup distribution

took place, the GH values were not significantly affected. Also covered in this chapter is the decayed GH, which occurs shortly after the reactor shut down. It was experimentally evaluated and compared with the simulation model. To experimentally estimate the decayed GH, it is crucial to acquire the negative reactivity insertion to discount the prompt GH. MCNP-6.2 was implemented to account for the prompt GH. The results of the prompt GH from MCNP-6.2 was compared with Serpent-2 simulation. A very good agreement was seen between the two codes, MCNP-6.2 and Serpent-2, in regard to the prompt GH. The decayed measured GH was integrated to the calculated prompt GH from MCNP-6.2 to evaluate the total GH. It was shown that implementing the measured decayed GH to the MCNP-6.2 calculation provided a promising option than calculation of the decayed GH.

## 8.2 Summary of novelties

Overall, the studies presented in this doctoral dissertation represent important steps forward for MNR core simulations and GH evaluations. These studies contribute new knowledge about:

- The OSCAR-4 and Serpent-2 code systems, which were implemented and used for core-follow calculation over a period of six years (2007-2013).
- Improving MNR operational data (mainly U-235) to emulate the actual fuel data. This was done by implementing the FIC factor and considering all fissile isotopes.

- GH measurements in several irradiation sites. The measurements were carried out during both MNR operation and shutdown. These values can be used for all future irradiations to estimate the level of GH. No change was observed in the GH for a five-year period of time.
- GH calculations employed using the Serpent-2 and MCNP-6.2 simulation codes. These calculations were compared against the measurement data and showed very good agreement.

## 8.3 Future work recommendations

Based upon the results of the studies performed in this thesis, further investigation in the following research areas would be valuable:

- Apply the OSCAR-4 code for a full collision-probability solution (STYX), or use the Serpent-2 code, for generating cross sections in the control rods regions.
- Develop a methodology for evaluation of the overall recoverable energy ($Q$-value) in the MNR core.
- Implement the MCNP-6.2 model for decayed GH calculation.
- Investigate the MNR core structure and the assembly of irradiation materials, such as beryllium and graphite, as they have been in the core for about 60 years.
- Write a program/script to link the MNR operational data for any cycle considering the FIC factor along with all fissile isotopes.
- Commission the other GT at the MNR for comparison to this work, providing a valuable data-base for the MNR core.

- Use neutron flux experiments from the MNR history to validate the methodology of the fuel inventory and code modelling applied in this work.

## 8.4 Conclusion

The MNR operational data can be used following the implementation of the FIC factor in any future simulation code. The OSCAR-4, Serpent-2 and MCNP-6.2 codes can be used to calculate the MNR safety core parameters. In addition, Serpent-2 and MCNP-6.2 can be used to evaluate the GH at any location. The application of these codes will help to optimize and quickly determine desired reactor core parameters. Additionally, the GH values were quantified in 37 points across the MNR core. Acquiring this information on GH, which is the main cause of irradiation damage, is very important for future irradiation applications. Finally, time-dependent GH was determined and showed no significant variation, especially when reactor core burnup configuration was not significantly altered.

# Appendix A

# Fuel plates inventory concentration at End-Of-Life (EOL)

In this research, it was assumed that the 16 radial fuel plates per each SFA are lumped into one node. In this section, the SFA EOL across the 16 fuel plates is presented. This will provide information on the reliability of assuming only one lumped radial inventory per 16 fuel plates. Figure A.1 shows the MNR SFA surrounded on one side by the MNR coolant, and by a reflective boundary condition on the other sides. Figure A.2 shows the U-235 fuel concentration across all 16 fuel plates.

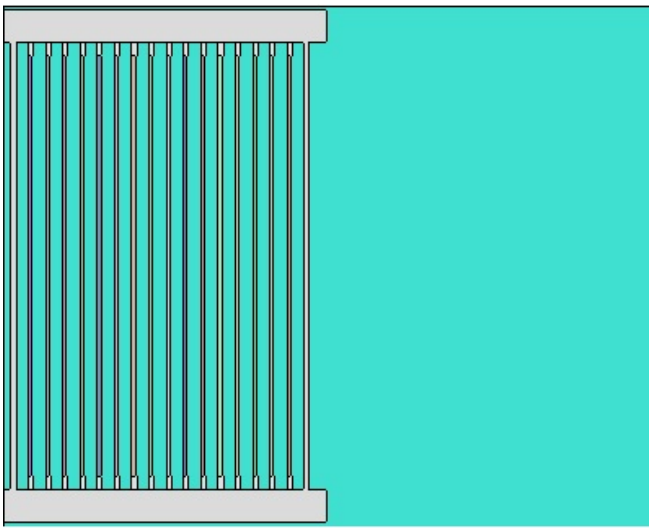

FIGURE A.1: Fuel assembly surrounded by water.

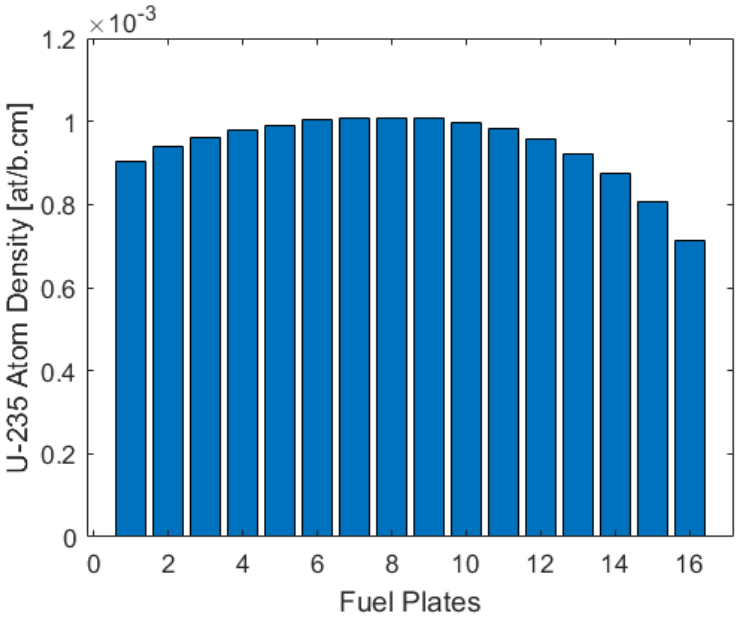


FIGURE A.2: Fuel plate inventory across 16 MNR fuel plates.

Even though the SFA was surrounded by a moderator (water), no significant change was seen across the radial U-235 fuel concentration. Therefore, assuming only one radial node per 16 nodes provides a reliable information.

# Appendix B

# Asymmetrical profile of the MNR fuel assembly

It was mentioned in the thesis that the U-235 axial asymmetrical isotope distribution may influence the axial results of the GH. In this section, the worst case scenario was considered with an end-of-life (EOL) of two fuel assemblies (FA) with 50% depletion as presented in Figure B.1. The two SFA here are: (i) symmetrical axial SFA number density, and (ii) the asymmetrical MNR SFA. Both of the SFA contains around $8.25 \times 10^{-3} at/b.cm$. From Figure B.1, it was found that a slight difference in the axial U-235 concentration profile. Future work was suggested to study this effect on the GH values.

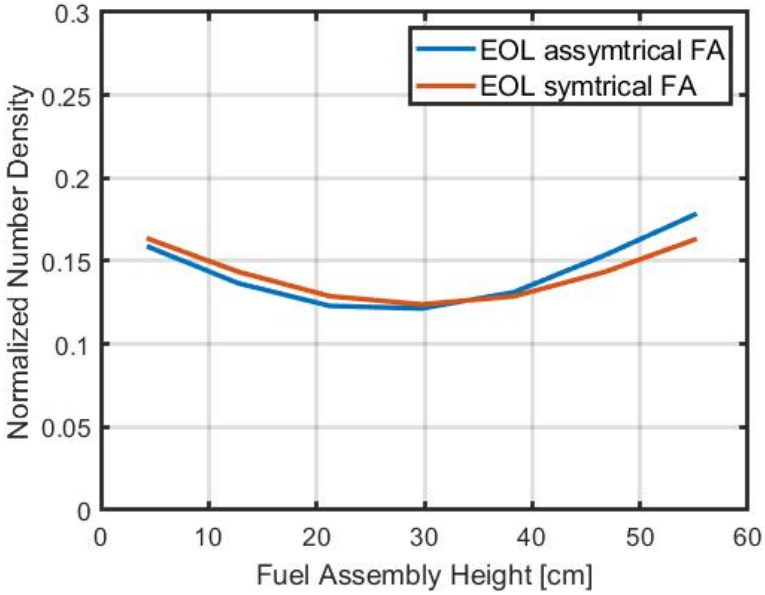


FIGURE B.1: Symmetrical and asymmetrical fuel assembly behaviour at the EOL.

# Appendix C

# Uncertainty quantification

## Experimental lateral GH variation

Chapter 6 provided estimation of the lateral uncertainty GH distribution across the Be assembly and the inner GT location. The latter has been experimentally measured in four lateral sites in the same irradiation assembly. Figure C.1 shows the GH values in [W/g] at each lateral GT position. The red dots represent the GT position inside the rig.

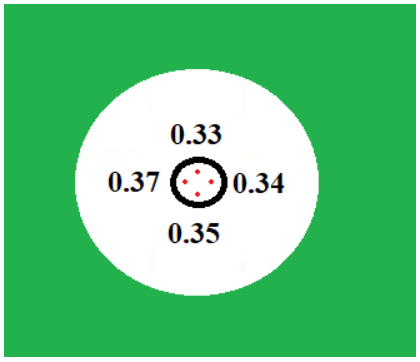


FIGURE C.1: GH values in [W/g] at four GT locations inside the Be assembly.

It can be seen that the lateral GH uncertainty varied around 10% when the GT moved radially inside the Be assembly. This was estimated in chapter 6 using Serpent-2 and was found at 9% with 95%

uncertainty interval.

## GT instrument uncertainty and combined uncertainty

In chapter 6, all uncertainties related to environmental change conditions and noises from the instruments were quantified. However, the instruments' calibration error are missing from these uncertainties and can also contribute to the combined total uncertainty. One such instrument is the RTD for MNR core power measurement.

MNR uses a class B type RTD which has a tolerance bias (acceptable limits of variance) based on the RTD's environment temperature. Figure C.2 illustrates the RTD's tolerance versus the temperatures [23].

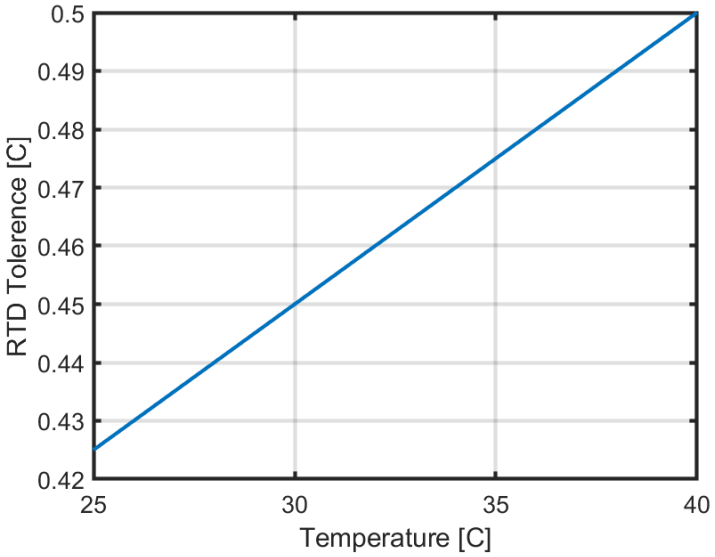


FIGURE C.2: RTD tolerance versus temperature.

The inlet and outlet temperatures in MNR are $30 \pm 0.11$ °C and $35.5 \pm 0.1$ °C, respectively. As seen in Figure C.2, the average bias of the temperature difference — which eventually becomes similar to the reactor power difference — is around 0.47°C. This difference seems low; however, it corresponds to a bias in reactor power of about 8.3%. This uncertainty should also be considered whenever GH measurement is performed at the MNR. Additionally, the GT instrument also has a 10% uncertainty. This means that the GH measured by GT can be estimated to within 10% at best. Combining the uncertainties here along with the uncertainties in the previous work, we get a 16.7% uncertainty, corresponding to confidence limits of about 95 %. This combined uncertainty will be used for all future GH values.

# Appendix D

# Serpent-2 simulation analysis of the local power, neutron flux, photon flux and GH

The local fuel assemblies' powers at MNR are proportionally following the MNR total power, which nominally operates at 3 $MW_{th}$. Figures D.1, D.2 and D.3 show the power, photon and neutron distribution across the MNR core of October 2019.

| | 9 | 8 | 7 | 6 | 5 | 4 | 3 | 2 | 1 |
|---|---|---|---|---|---|---|---|---|---|
| A | W | G | W | 0.60 | 0.55 | 0.55 | 0.44 | Be | 0.22 |
| B | W | G | 0.58 | 0.49 | 0.80 | 0.44 | 0.64 | 0.51 | 0.30 |
| C | W | G | 0.72 | 0.86 | 1.00 | 0.84 | 0.71 | 0.38 | 0.33 |
| D | G | G | W | 0.87 | 0.96 | 0.83 | 0.72 | 0.67 | 0.41 |
| E | W | G | 0.56 | 0.43 | 0.76 | 0.48 | 0.65 | 0.39 | 0.40 |
| F | W | G | W | 0.51 | 0.45 | 0.44 | 0.46 | 0.45 | 0.30 |

FIGURE D.1: Local assemblies powers normalized to the maximum assembly power of 122 kW.

| | 9 | 8 | 7 | 6 | 5 | 4 | 3 | 2 | 1 |
|---|---|---|---|---|---|---|---|---|---|
| A | 0.16 | 0.25 | 0.37 | 0.52 | 0.59 | 0.58 | 0.50 | 0.38 | 0.26 |
| B | 0.21 | 0.33 | 0.54 | 0.74 | 0.85 | 0.81 | 0.72 | 0.57 | 0.38 |
| C | 0.24 | 0.39 | 0.64 | 0.87 | 1.00 | 0.96 | 0.85 | 0.66 | 0.44 |
| D | 0.23 | 0.40 | 0.62 | 0.84 | 0.98 | 0.96 | 0.86 | 0.70 | 0.47 |
| E | 0.21 | 0.34 | 0.52 | 0.69 | 0.81 | 0.81 | 0.75 | 0.62 | 0.43 |
| F | 0.18 | 0.27 | 0.38 | 0.50 | 0.56 | 0.56 | 0.54 | 0.46 | 0.33 |

FIGURE D.2: Local assemblies photon flux normalized to the maximum assembly photon flux of $1.56 \times 10^{14}$ photons/cm$^2 s$.

| | 9 | 8 | 7 | 6 | 5 | 4 | 3 | 2 | 1 |
|---|---|---|---|---|---|---|---|---|---|
| A | 0.10 | 0.26 | 0.42 | 0.53 | 0.61 | 0.60 | 0.53 | 0.43 | 0.25 |
| B | 0.13 | 0.33 | 0.52 | 0.73 | 0.84 | 0.81 | 0.72 | 0.56 | 0.34 |
| C | 0.15 | 0.38 | 0.61 | 0.86 | 1.00 | 0.97 | 0.84 | 0.64 | 0.40 |
| D | 0.16 | 0.38 | 0.63 | 0.82 | 0.98 | 0.97 | 0.85 | 0.66 | 0.42 |
| E | 0.12 | 0.30 | 0.46 | 0.65 | 0.78 | 0.78 | 0.72 | 0.59 | 0.38 |
| F | 0.07 | 0.20 | 0.33 | 0.43 | 0.51 | 0.52 | 0.48 | 0.40 | 0.27 |

FIGURE D.3: Local assemblies neutron flux normalized to the maximum assembly neutron flux of $9.53 \times 10^{13}$ neutrons/cm$^2 s$.

The hot-spot fuel assembly in terms of local power, neutron flux and gamma flux is at location 5C. This indicates that the neutron and gamma fluxes are strongly proportional to the local power. However, the GH distribution does not necessarily follow the exact distribution of the gamma flux, especially when the core consists of multiple assemblies that are not fuelled or that contain a dense material.

Figure D.4 shows the radial distribution of the GH in the MNR core.

| | 9 | 8 | 7 | 6 | 5 | 4 | 3 | 2 | 1 |
|---|---|---|---|---|---|---|---|---|---|
| A | 0.04 | 0.11 | 0.11 | 0.52 | 0.57 | 0.56 | 0.47 | 0.20 | 0.24 |
| B | 0.06 | 0.15 | 0.53 | 0.63 | 0.84 | 0.68 | 0.70 | 0.54 | 0.35 |
| C | 0.06 | 0.17 | 0.63 | 0.86 | 1.00 | 0.94 | 0.82 | 0.55 | 0.41 |
| D | 0.08 | 0.17 | 0.18 | 0.83 | 0.98 | 0.93 | 0.83 | 0.68 | 0.44 |
| E | 0.06 | 0.15 | 0.49 | 0.58 | 0.80 | 0.68 | 0.72 | 0.52 | 0.41 |
| F | 0.04 | 0.11 | 0.11 | 0.47 | 0.52 | 0.52 | 0.50 | 0.44 | 0.30 |

FIGURE D.4: GH distribution normalized to the maximum GH value of 2.28 W/cm$^3$.

The photon flux in the Be assembly (2A) is higher than the photon flux in fuel assembly (1A), see Figure D.2. However, the GH shows higher in (1A), see Figure D.4. This confirms that GH is a consequence of radiation (gamma) interaction with the material.

# Appendix E

# Gamma thermometer (GT) dip test calibration

Calibration of the GT using the dip-test method was performed to estimate the unknown constants needed in the calibration factor as well as the GT time constant. The GT is placed in boiling water to bring the entire GT (inner and outer body) to approximately 100°C. Then, it was quickly removed from the boiling water and placed into an ice bath. The thermocouple's output recording are shown in Figure E.1.

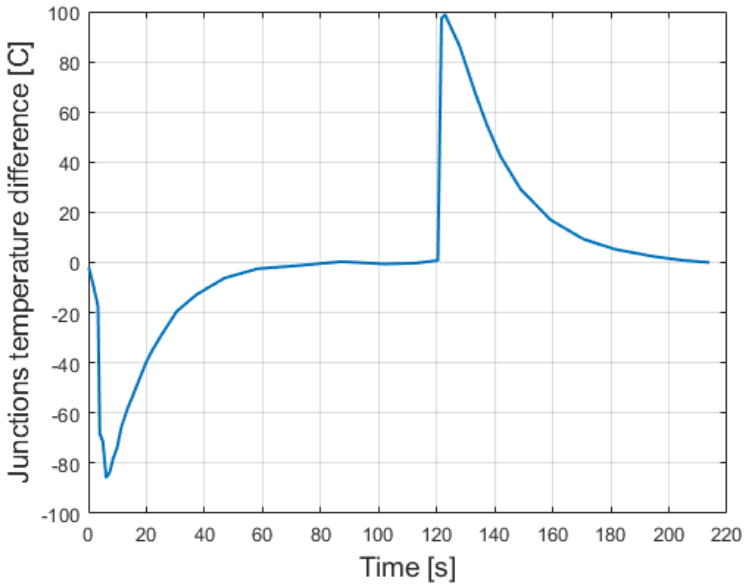


FIGURE E.1: Experimental GT dip-test method (hot-to-cold).

The time constant of the GT is found to be approximately 21 seconds. This value is an important parameter in describing the response of the GT.

# Bibliography

[1] IAEA, "Applications of research reactors," Tech. Rep. No. NP-T-5.3, International Atomic Energy Agency, Vienna, January 2014.

[2] IAEA, "Research reactors for the development of materials and fuels for innovative nuclear energy systems," Tech. Rep. No. NP-T-5.8, International Atomic Energy Agency, Vienna, Austria, 2017.

[3] D. Fourmentel, P. Filliatre, L. Barbot, J. F. Villard, A. Lyoussi, B. Geslot, H. Carcreff, J. Y. Malo, and C. Reynard-Carette, "Comparison of thermal neutron flux measured by $^{235}$u fission chamber and rhodium self-powered neutron detector in mtr," IEEE Transactions on Nuclear Science, vol. 61, no. 4, pp. 2285–2290, 2014.

[4] N. Xoubi, S. A. Darda, A. Y. Soliman, and T. Abulfaraj, "An investigative study of enrichment reduction impact on the neutron flux in the in-core flux-trap facility of mtr research reactors," Nuclear Engineering and Technology, vol. 52, no. 3, pp. 469–476, 2020.

[5] IAEA, "Research Reactor Application for Materials under High Neutron Fluence," tech. rep., 2011. IAEA-TECDOC-1659.

[6] M. Lemaire, C. Vaglio-Gaudard, A. Lyoussi, and C. Reynard-Carette, "For a better estimation of gamma heating in experimental reactors and devices: Stakes and work plan from calculation methods to nuclear data," 2013 3rd International Conference on Advancements in Nuclear Instrumentation, Measurement Methods and their Applications (ANIMMA), 2013.

[7] IAEA, "Applications of research reactors," Tech. Rep. No. NP-T-5.3, International Atomic Energy Agency, Vienna, January 2014.

[8] C. Heysel, A. Armstrong, J. Bennett, E. Werger, Z. Naperstkow, and R. Pasuta, "Customized Irradiation Sites For Medical Isotope Production," vol. 50, Canadian Nuclear Society (CNS), 2018.

[9] A. Tonchev, J. Silano, J. Wilhelmy, and M. Gooden, "Fission Gamma-Ray Spectra Relevant to Post-Detonation Debris Analysis," Tech. Rep. LLNL-TR-765862, LLNL and LLAL, January 2019.

[10] A. Tonchev and J. S. J. W. M. Gooden, "Fission Gamma-Ray Spectra Relevant to Post-Detonation Debris Analysis," Tech. Rep. LLNL-TR-765862, Lawrence Livermore National Laboratory, 2019.

[11] M. Kowalok, Adjoint methods for external beam inverse treatment planning. PhD thesis, 2004.

[12] M. Dehart, A Discrete Ordinates Approximation to the Neutron Transport Equation Applied to Generalized Geometries. PhD thesis, Texas AM University, 1992.

[13] A. Haghighat, ed., (2021). Monte Carlo methods for particle transport (pp. 85-90). Taylor and Francis Group.

[14] J. F. Briesmeister, MCNP-A General Monte Carlo N-Particle Transport Code, Manual, Version 4.A. Los alamos national laboratory report LA-12625-M, 1993.

[15] LANL, RSICC computer code collection. Radiation Safety Information Computational Center, 2013.

[16] J. Duderstadt and L. Hamilton, (1976). Nuclear reactor analysis (pp. 133-140). New York: Wiley.

[17] T. Kaltiaisenaho, "Photon transport physics in Serpent 2 Monte Carlo code, Computer Physics Communications," 2020.

[18] Necsa, South Africa, "Axial homogenization model," tech. rep., 2008. MGRAC Methodology.

[19] W. M. Stacey, (2007). Nuclear Reactor Physics (pp. 303-383).

[20] S. Day, "Mcmaster nuclear reactor: Benchmark specification," tech. rep., 2011. Submitted to IAEA CRP: Innovative methods for research reactors.

[21] M. Chadwick, M. Herman, P. Obložinský, M. Dunn, Y. Danon, A. Kahler, D. Smith, B. Pritychenko, G. Arbanas, R. Arcilla,

R. Brewer, D. Brown, R. Capote, A. Carlson, Y. Cho, H. Derrien, K. Guber, G. Hale, S. Hoblit, S. Holloway, T. Johnson, T. Kawano, B. Kiedrowski, H. Kim, S. Kunieda, N. Larson, L. Leal, J. Lestone, R. Little, E. McCutchan, R. MacFarlane, M. MacInnes, C. Mattoon, R. McKnight, S. Mughabghab, G. Nobre, G. Palmiotti, A. Palumbo, M. Pigni, V. Pronyaev, R. Sayer, A. Sonzogni, N. Summers, P. Talou, I. Thompson, A. Trkov, R. Vogt, S. [van der Marck], A. Wallner, M. White, D. Wiarda, and P. Young, "Endf/b-vii.1 nuclear data for science and technology: Cross sections, covariances, fission product yields and decay data," Nuclear Data Sheets, vol. 112, no. 12, pp. 2887 – 2996, 2011. Special Issue on ENDF/B-VII.1 Library.

[22] E. L. MacConnachie and D. R. Novog, "Measurement, simulation and uncertainty quantification of the neutron flux at the mcmaster nuclear reactor," Annals of Nuclear Energy, vol. 151, p. 107879, 2021.

[23] B. (BAPI), "Thermistor vs RTD Temperature Accuracy." `http://www.bapihvac.com/wp-content/uploads/Therm_vs_RTD.pdf`.